Performance Studies for the KM3NeT Neutrino Telescope

Der Naturwissenschaftlichen Fakultät
der Friedrich-Alexander-Universität Erlangen-Nürnberg
zur Erlangung des Doktorgrades

vorgelegt von
Claudio Kopper
aus Erlangen

Als Dissertation genehmigt von der Naturwissenschaftlichen Fakultät
der Friedrich-Alexander-Universität Erlangen-Nürnberg

Tag der mündlichen Prüfung:	12. März 2010
Vorsitzender der Promotionskommission:	Prof. Dr. Eberhard Bänsch
Erstberichterstatter:	Prof. Dr. Ulrich Katz
Zweitberichterstatter:	Prof. Dr. Christian Stegmann

Meinen Eltern

Contents

Introduction

It is impressive how extensive our knowledge about the universe and its contents has become by just looking at the night sky. Astronomy has come a long way from its beginnings with observations using the naked eye to modern times, where sophisticated instruments are used to record the information reaching us from the stars, galaxies and from the host of other amazing things that exist out there. Until recent times, this information has almost exclusively been measured by detecting photons, either at optical wavelengths or at other bands including radio, x-rays and γ-rays.

There are, however, other particles that reach us, that, until recently, have not been used to look at the universe. One example is the flux of charged, high-energy protons and nuclei that are continuously hitting our atmosphere. As it is the case so often, the discovery of these particles[1] (being a major part of what has been called "cosmic rays"), posed more new questions than it answered: Where do these particles come from? How are they accelerated to the extremely high energies that we observe?

This thesis was written to be part of a tiny step towards answering these questions. Even though it is impossible to deduce the origin of most of these charged particles when they arrive at Earth because their trajectories have been altered by interstellar magnetic fields, it is nevertheless possible to "see" cosmic ray sources by using two other types of messengers that are produced in association with them: TeV-γ-rays and neutrinos. Both of them being uncharged, they can be used to deduce their source's origin and, thus, the origin of cosmic rays. TeV-γ-ray astronomy has come a long way in the recent years, especially thanks to the H.E.S.S. experiment which was able to produce whole sky maps of sources, some of them corresponding to an already known object, some of them being entirely new ones. There are, however, fundamental problems when only looking for sources emitting γ-rays with energies of a few TeV. One of these problems is that the sources may be too dense and thus may possibly absorb most of their emitted γ-rays. Another problem is that the observed TeV-γ-ray spectra could either be produced through leptonic effects (inverse compton scattering of photons from relativistic electrons and synchrotron radiation) or by the decay of neutral pions, produced by the interaction of high-energy protons. Proving that it is really hadronic interactions that produce the measured γ-ray spectra and thus showing that these sources are the accelerators of cosmic rays is extremely hard by only looking at photons.

---

[1] The discovery was made by Victor Hess in 1912 during a balloon flight.

The other kind of uncharged particles from cosmic ray sources that are able to reach us are neutrinos. As they are only weakly interacting, they are not absorbed on their way to us, making them a unique tool for gathering more insight into sources of cosmic rays, of both galactic and extragalactic origin. It is, however, exactly these properties that make them so hard to detect. Their extremely low cross sections require huge amounts of target material to be able to detect them in significant numbers. As detectors with their target material in containers or caverns have a certain limit in size, both due to monetary and technological constraints, high-energy neutrinos are usually detected using natural resources as a target. The charged particles produced by a neutrino interaction are detected using light emitted from them due to the Cherenkov effect, making a naturally occurring large volume of a transparent medium a requirement for building a neutrino detector. The only resource available in the required abundance is water, either in its liquid state, i.e. sea or lake water, or as ice in the glaciers of Antarctica. Deploying a light-detecting instrumentation into these media allows to detect neutrinos in the energy range from a few GeV up to the EeV region. Detecting neutrinos from a cosmic ray source would be a "smoking gun" evidence for disentangling between hadronic and leptonic acceleration.

Several experiments, starting with the DUMAND project in 1976 aimed to build such a detector with the goal of eventually using it as a neutrino telescope. Today, the BAIKAL experiment is the longest-running neutrino detector, operating since 1993. AMANDA and its km^3-sized successor IceCube have been taking data for years at the South Pole. In the meantime, AMANDA has already been shut down, with IceCube's construction being almost complete. The remaining projects are all situated in the Mediterranean Sea, two of them (NESTOR and NEMO) performing preliminary studies and in-sea testing.[2] The third project, ANTARES, has finished building a neutrino detector with a size comparable to AMANDA and has been successfully taking data for several years. Unfortunately, none of these detectors could yet find a source of cosmic neutrinos, but predictions from TeV-γ-ray sources show that there is a good chance of detecting high-energy neutrinos with km^3-scale detectors.

This work is concerned with the KM3NeT project, a joint effort of the NESTOR, NEMO and ANTARES collaborations, with the aim to build a neutrino telescope in the Mediterranean Sea which will surpass IceCube's sensitivity. The KM3NeT Consortium has just finished writing the Technical Design Report (TDR), which is currently in press, and thus has concluded its "Design-Study" phase associated with planning for the actual detector construction. This effort required extensive amounts of simulation in order to optimise the detector design, including detector geometries and sensor designs.

---

[2] NEMO is an R&D study for a km^3 neutrino telescope, whereas NESTOR does aim to build a full detector.

This thesis is part of the effort to study the performance of various detector designs and determine their physics performance. Its goal is to compare different design options that were being discussed for KM3NeT with a focus on one of the newer detector design options, which did not receive as much attention up to now because of the lack of a dedicated reconstruction algorithm. To achieve these means, a new simulation software chain, consisting of tools developed by the IceCube collaboration and of tools developed specifically for KM3NeT as part of this work was implemented.

The document is split into three parts: The first one introduces the physics of neutrino production and detection and presents the detection method common to all neutrino telescopes. It also introduces the currently working neutrino detectors and the KM3NeT project.

The second part gives a detailed description of the methods developed for studying different KM3NeT detector designs. It includes descriptions of all the already existing tools that were used for this study, among them the neutrino event generators from ANTARES and IceCube that both can be used for KM3NeT. It also presents the large number of algorithms that have been developed as part of this thesis and presents a software framework that was introduced for KM3NeT as part of this work.[3] The algorithms presented include a new muon propagation code and a Cherenkov light simulation for both muons and cascades induced by neutrinos. Additionally, a new reconstruction technique inspired by methods used for the IceCube neutrino telescope is introduced. Finally, the most common analysis techniques for neutrino point-sources are presented.

The third part of the document shows the results obtained for different KM3NeT designs using the new simulation chain introduced previously. Results obtained with this new chain are first compared to those produced with the old ANTARES tools. The new chain is then used to compare different detector design possibilities for KM3NeT. The remainder of the document then focusses on one of these possibilities and explores the effects of scaling the detector in various ways. At the very end of the thesis, the results and conclusions obtained earlier are summarised.

---

[3] When this work was started, KM3NeT and ANTARES did not use any kind of software frameworks, a point that often lead to confusion and hard-to-find software bugs.

Part I

Basics

1 High energy cosmic neutrinos

> Physics isn't a religion. If it were, we'd have a much easier time raising money.
>
> *(Leon Lederman)*

At first sight, neutrinos seem to be rather dull particles; they are virtually massless, do not have an electric charge and only interact weakly. It is exactly these properties, however, that make them so valuable for astroparticle physics. Unlike charged particles, they are not influenced by cosmic magnetic fields, so that any neutrino measured on Earth will point back to its source. And, unlike photons, neutrinos are not absorbed by interstellar matter due to their extremely low interaction cross-section.[1] They are also not influenced by photon fields and can escape very dense source environments.

This chapter will first provide a very brief history of the discovery of the neutrino and introduce its basic properties within the Standard Model. It will then describe possible cosmic sources of high energy neutrinos and a mechanism for particle acceleration within these sources.

1.1 Neutrinos in the Standard Model

The (electron) neutrino was first postulated by Pauli in 1930 in his famous letter to Lise Meitner *et al.* [1], to explain the continuous spectrum of electrons seen from radioactive beta decays. Unwilling to give up momentum conservation on the sub-atomic scale, he proposed to add a third, massless and uncharged particle to the final state of the decay

$$\mathrm{n} \rightarrow \mathrm{p} + \mathrm{e}^{-} + \bar{\nu}_{\mathrm{e}}. \tag{1.1}$$

This does not only explain the observed electron energy spectrum, but also ensures that the conservation of angular momentum is not violated. It took another 26 years until the actual discovery of the electron (anti-)neutrino by Reines and Cowan [2] in 1956 in their water and cadmium-chloride-based scintillation detector.

---

[1] This is only true up to a certain neutrino energy.

Since then, two more neutrino flavours have been discovered, namely the muon [3] and tau [4][2] neutrino. Together with their charged partners, these particles entered the Standard Model as three lepton families, corresponding to the three generations of quarks. In the Standard Model, neutrinos are assumed to be massless and only couple to other particles via the weak interaction, i.e. via the W and Z bosons.

In an extension to the Standard Model, neutrinos are allowed to have a small non-vanishing mass to explain the occurrence of *neutrino oscillations* [6]. This effect explains the *solar neutrino deficit* [7], where the number of electron neutrinos reaching the earth from the sun is too low to be explained by common solar models. However, when combining the neutrino flux of all three flavours, the measured flux becomes compatible with these models. This behaviour is explained by oscillations of neutrinos between different flavour eigenstates. This is possible because the flavour eigenstates are not identical to the mass eigenstates of the three neutrino generations and because these mass eigenstates are not identical.

This thesis will be primarily concerned with muon neutrinos, as their signature in neutrino detectors provides the best pointing to potential sources. More on the signatures of the different neutrino flavours in a neutrino telescope can be found in section 2.1.

1.2 Cosmic accelerators

Each high energy cosmic neutrino measured in an earth-based detector originates from a certain source. Though there are a number of different possible production mechanisms, the currently favoured one is the acceleration of protons within a source and their subsequent conversion into neutrinos through pion decay.

This section describes an acceleration mechanism that is capable of producing extremely high non-thermal energies that are already seen in cosmic rays [8, 9] and which are thus also expected for neutrinos. It outlines neutrino production at a source and gives a short overview of the most probable astrophysical objects capable of neutrino production.

1.2.1 The cosmic ray spectrum

Since Victor Hess opened a new window for astronomical observations by detecting the first cosmic rays in 1912 [10], a multitude of experiments have provided knowledge about their energy spectrum and composition. To our current knowledge, cosmic rays mainly consist of protons and heavier nuclei in addition to small amounts

---

[2] The referenced paper describes the actual direct measurement of the tau neutrino that was achieved in 2000. Indirect measurements from collider experiments have given strong evidence to its existence long before [5].

of electrons and positrons. Their energy spectrum spans several orders of magnitude and follows, to a very good approximation, a power law. Thus, the differential flux can be written as

$$\frac{\mathrm{d}N}{\mathrm{d}E} \propto E^{-\gamma}, \tag{1.2}$$

with γ being the so-called *spectral index*. Today, the highest recorded energies are of the order of about 10^{11} GeV. Figure 1.1 shows the measured cosmic ray spectrum including two points where the spectral index abruptly changes, known as the *knee* and the *ankle*. The *knee* at about $3 \cdot 10^{6}$ GeV corresponds to a change of spectral index from $\gamma \approx 2.7$ to approximately $\gamma \approx 3$. The spectrum stays at this steeper slope up to the *ankle* at about $3 \cdot 10^{9}$ GeV, where the spectral index changes again, back to $\gamma \approx 2.7$. The even higher energies, the interaction of cosmic ray protons with the 2.7 K black body radiation of the cosmic microwave background leads to a cutoff in the spectrum at about $6 \cdot 10^{10}$ GeV. This effect has been called the "GZK-cutoff" [11, 12].

1.2.2 Particle acceleration

A proposed mechanism that allows particles to be accelerated up to very high energies is the so-called *first-order Fermi acceleration* [18–21], which sometimes is referred to as *shock acceleration*. The basic idea is that particles are accelerated at a shock front between two colliding plasmas. For an overview of phenomena that could cause such a shock, see section 1.2.4.

The acceleration process itself can be sketched using a simple two-dimensional argument. Consider a shock front moving with the velocity v_S relative to the surrounding medium, which is considered to be at rest. If one assumes magnetic inhomogeneities on both sides of the shock front that randomise the directions of charged particles, these particles can be elastically scattered between these two sides multiple times. For each scattering iteration, a particle will gain energy until it finally leaves the shock front region.

In more detail, the argument can be the following: the shocked plasma behind the shock front travels with a lower speed v_P, which is related to v_S by shock hydrodynamics as

$$v_\mathrm{P} = \frac{3}{4} v_\mathrm{S}. \tag{1.3}$$

A particle with an initial energy E_1 crosses the shock front from downstream to upstream at an angle θ_1 (cf. figure 1.2 for an illustration). Transforming E_1 to the new reference frame yields

$$E_1' = \gamma E_1 \left(1 - \beta \cos\theta_1\right), \tag{1.4}$$

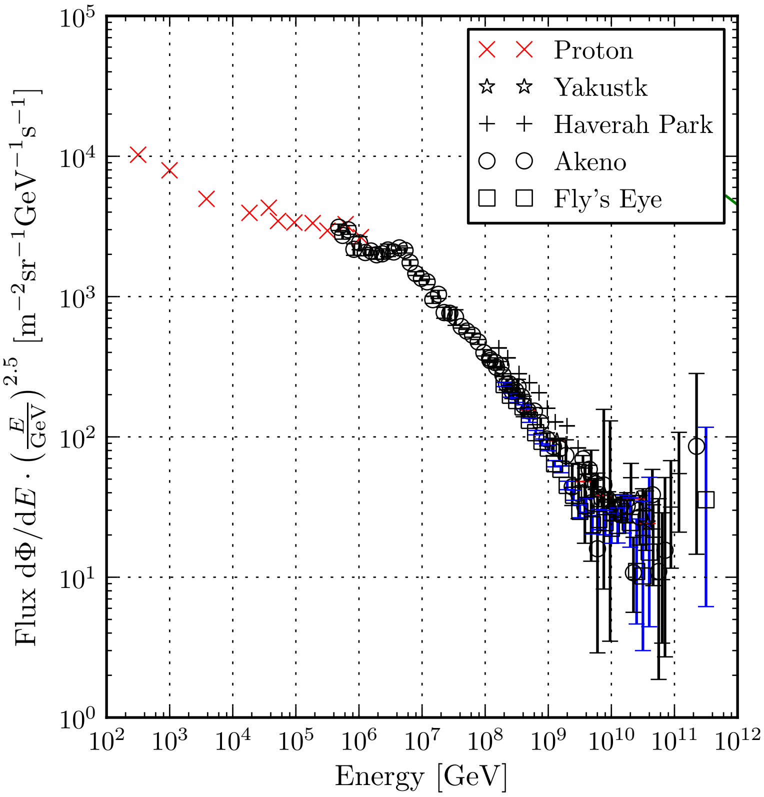

Figure 1.1 The energy spectrum of cosmic rays compiled from various experiments. Data provided by the author of [13], which was in turn compiled from [14–17].

with $\beta := v_\mathrm{P} c^{-1}$ and $\gamma := \left(1-\beta^2\right)^{-\frac{1}{2}}$. The particle is now scattered elastically at magnetic irregularities so that it crosses the shock front again, back to its downstream side. Thus, its energy in the shocked reference frame is unchanged $E_2' = E_1'$, whereas its direction is randomised so that it crosses the boundary at an angle of θ_2'.

The transformation back to the initial frame can be written as

$$E_2 = \gamma E_2' \left(1 + \beta \cos\theta_2'\right). \tag{1.5}$$

Therefore, the particle's new energy after crossing the shock front twice is

$$E_2 = \gamma^2 E_1 \left[1 - \beta\left(\cos\theta_1 - \cos\theta_2'\right) - \beta^2 \cos\theta_1 \cos\theta_2'\right] - 1. \tag{1.6}$$

Assuming isotropic scattering on both sides of the shock front, the average values of the crossing angle cosines can be calculated as $\langle\cos\theta_2'\rangle = -\langle\cos\theta_1\rangle = \frac{2}{3}$. Using

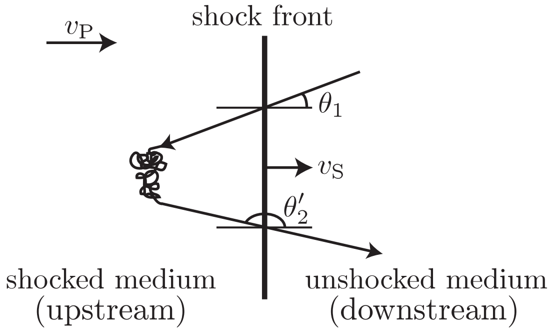

Figure 1.2 Illustration of a particle crossing a shock front from the unshocked medium into the shocked one. The particle's direction is randomised in magnetic irregularities until it crosses the front again. The shock front is travelling with a speed of v_S, whereas the plasma behind it has a lower speed of v_P.

(1.6), this immediately allows to derive the average energy change per cycle:

$$\langle \Delta E \rangle = \langle E_2 - E_1 \rangle \approx E_1 \left[1 - \beta \left(\langle \cos\theta_1 \rangle - \left\langle \cos\theta_2' \right\rangle \right) \right] - E_1 = \frac{4}{3} \beta E_1. \tag{1.7}$$

Terms proportional to β^2 have been neglected. After n cycles, the particle's average energy will then be $E_n = E_1 \left(1 + \epsilon\right)^n$, where $\epsilon := \frac{4}{3}\beta$. Solving this for the number of cycles needed to reach a given energy E yields

$$n = \frac{\ln\left({}^{E}\!/\!_{E_1}\right)}{\ln\left(1+\epsilon\right)}. \tag{1.8}$$

Assuming that the escape probability of a particle during one cycle is P_esc, the probability of crossing the shock at least n times is $P\left(N_\mathrm{cross} \geq n\right) = \left(1 - P_\mathrm{esc}\right)^n$. The integral energy spectrum of particles escaping the shock region is proportional to this number:

$$Q(\geq E) \propto \left(1 - P_\mathrm{esc}\right)^n . \tag{1.9}$$

Substituting (1.8) yields[3]

$$Q(\geq E) \propto E^{-\Gamma}, \tag{1.10}$$

where $\Gamma := -\frac{\ln(1-P_{\mathrm{esc}})}{\ln(1+\epsilon)}$. Assuming both ϵ and P_{esc} are small, Γ will be of the order of 1. The differential energy spectrum thus looks like

$$Q(E) = \frac{\mathrm{d}N}{\mathrm{d}E} \propto E^{-2}. \tag{1.15}$$

The derivation of this power-law spectrum does however rely on a number of simplifications and assumptions and are only valid up to a certain energy. More realistic calculations [22] yield indices in the range of $\gamma \in [2.1, 2.4]$. The actual measured spectral index of $\gamma \approx 2.7$ can be explained by taking into account the energy-dependent leakage of cosmic rays from the galaxy.

1.2.3 Neutrino production

The conventional models for neutrino production are based on interactions of accelerated protons and nuclei with photon or matter fields near or in the astrophysical source. The primary reaction produces neutral and charged pions

$$\mathrm{p} + \mathrm{p}/\gamma \rightarrow \pi^+ + \pi^- + \pi^0 + \mathrm{X}. \tag{1.16}$$

Whereas neutral pions mainly decay into photons, which can subsequently be detected by imaging air-shower cherenkov telescopes, charged pion decays yield neutrinos.

$$\begin{aligned}
\pi^+ &\rightarrow \mu^+ + \nu_\mu \rightarrow e^+ + \nu_e + \bar{\nu}_\mu + \nu_\mu & (1.17)\\
\pi^- &\rightarrow \mu^- + \bar{\nu}_\mu \rightarrow e^- + \bar{\nu}_e + \nu_\mu + \bar{\nu}_\mu & (1.18)\\
\pi^0 &\rightarrow 2\gamma & (1.19)
\end{aligned}$$

In these decays, the fraction of energy carried by the resulting neutrinos is approximately independent from the mesons' energies. The neutrino spectrum thus closely resembles the proton spectrum. Ignoring the distinction between neutrinos and anti-

---

[3] The equation can be transformed as follows:

$$\begin{aligned}
& Q(\geq E) = A\,(1-P_{\mathrm{esc}})^n & (1.11)\\
\Rightarrow\;& \ln Q(\geq E) = A + \frac{\ln\left({}^{E}/_{E_1}\right)}{\ln(1+\epsilon)} \ln(1-P_{\mathrm{esc}}) & (1.12)\\
\Rightarrow\;& \ln Q(\geq E) = B - \Gamma \ln E & (1.13)\\
\Rightarrow\;& Q(\geq E) \propto E^{-\Gamma}, & (1.14)
\end{aligned}$$

where A and B are constants and $\Gamma := -\frac{\ln(1-P_{\mathrm{esc}})}{\ln(1+\epsilon)}$.

neutrinos[4], the neutrino flux ratios are expected to be $\nu_e : \nu_\mu : \nu_\tau = 1 : 2 : 0$. Due to neutrino oscillations, this ratio is changed to $1 : 1 : 1$.[5]

1.2.4 Source candidates

This section summarises the most important source candidates that are thought be able to produce cosmic rays and therefore high-energy neutrinos. For details see the reviews in [22, 23].

Active Galactic Nuclei (AGN)

Galaxies with a supermassive black hole in their centre and an accretion disc surrounding it are classified as "Active Galactic Nuclei" (AGNs). As the matter from the accretion disc spirals inwards, it is finally ejected perpendicular to the disc in relativistic jets. It is along these jets that emission of high-energy neutrinos is expected. AGNs are already known to emit high-energy gamma rays, especially along their jets.

Depending on their jet's direction and thus their appearance from our point of view, different names are given to AGNs: Seyfert galaxies, radio galaxies, quasars, blazars and so on.

It is not entirely clear today which acceleration model leads to the observed AGN spectra. In one model, the *leptonic* acceleration model, low-energy synchrotron radiation from relativistic electrons is (inverse) Compton scattered on the electron population and can thus reach higher energies, a process called *Synchroton Self-Compton* (SSC). A competing model, the *hadronic* acceleration model, assumes that hadrons are accelerated to very high energies in the jet. They eventually interact with photons, producing π^0. The gamma rays from these pions would then lead to the observed gamma ray flux. Detection of neutrinos from an AGN could play an important role in resolving the question which of these models is actually valid.

Gamma Ray Bursts (GRB)

Gamma Ray Bursts are transient phenomena with a lifetime of up to several hundred seconds, emitting a gamma ray flux that outshines all other gamma ray sources. They are randomly distributed on the sky, so current models assume them to be extragalactic objects. Currently, GRBs are associated either with the core collapse of a very massive star leading to the formation of a black hole (so called *long-soft* GRBs) or with the merger of binary systems consisting of two neutron stars or a

---

[4] This assumption is possible because neutrino telescopes cannot distinguish between neutrinos and anti-neutrinos.

[5] This assumption is true for sources with an extent larger than the oscillation length.

neutron star and a black hole (*short-hard* GRBs). In both cases, matter is ejected from the object in ultra-relativistic jets.

The model that is currently best able to describe GRBs is the so-called fireball model, which is based on shock fronts at relativistically expanding spherical shells. Along with the gamma rays, emission of high-energy neutrinos is expected from these objects.[24]

Starburst Galaxies

Galaxies with a high rate of star formations, the so-called "starburst galaxies", have been suggested to emit neutrinos. Observations of synchrotron radiation at radio wavelengths and of TeV γ-rays from their dense core regions [25] imply the existence of relativistic electrons. Assuming that protons are accelerated along with these electrons, the dense core regions with high matter densities can act as proton beam-dumps. Neutrinos from the resulting p-p interactions could potentially be detected by km^3-sized neutrino telescopes like IceCube or KM3NeT [26].

Supernova Remnants (SNR)

One possible source of Galactic cosmic rays and therefore presumably of neutrinos are the remnants of supernovae, i.e. the material emitted from the initial explosion that encounters the interstellar medium and builds a shock front. The measured gamma ray spectra from SNRs can be used to calculate approximate neutrino rates from these objects, making detection of neutrinos from these sources possible with km^3-scale detectors [27]. As a concrete example, the analysis of RXJ1713.7-3946 measured by H.E.S.S. favours hadronic acceleration, which should lead to a measurable neutrino flux [28].

Pulsar Wind Nebulae

Whenever the axis of a neutron star's magnetic field points into our direction, we possibly observe the object as a pulsar. Particles are accelerated to relativistic energies, and they can subsequently react with the surrounding matter. Some of the brightest sources in TeV gamma rays are pulsar wind nebulae, among them the Crab and Vela pulsars [29, 30]. Though the gamma acceleration process is usually assumed to be leptonic, it has been suggested that there may be a hadronic part in the pulsar wind, which makes production of neutrinos possible [31].

Microquasars

Microquasars are another candidate for neutrino production. They are binary systems consisting of a neutron star or black hole of approximately a solar mass and a single star. The compact object accretes mass from the star and produces a relativistic jet perpendicular to the accretion disc. It has been shown that these objects may emit high energy neutrinos [32, 33]. It has been argued that γ-rays emitted from microquasars may be heavily absorbed inside the source. Neutrino fluxes for these sources could thus be much higher than predicted from their TeV-γ-ray spectra [34].

Other neutrino sources

There is a multitude of other suggested neutrino sources, among them various dark matter models and more exotic 'top-down' models suggesting that neutrinos may be produced by super-massive relic particles from the Big Bang. These other sources will not be considered in this work.

2 Neutrino telescopes

> One neutrino is a signal.
> Two neutrinos are a
> spectrum.
>
> *(Francis Halzen)*

Single-photo detection techniques and fast readout electronics have made it possible to build large-scale neutrino telescopes able to reconstruct the particles produced in neutrino interactions. This chapter shall describe the detection mechanisms currently used by neutrino telescopes and give an overview of different background sources that overlay the signal of cosmic neutrinos.[1] In addition, currently running neutrino telescope projects and the KM3NeT design study are presented.

2.1 Detection mechanism

Because of their very low interaction cross-section and their lack of charge, neutrinos can not be detected directly. However, the products of a neutrino interacting with a nucleon of the surrounding matter can be detected. Neutrino telescopes use the Cherenkov light emitted by muons (and other charged particles) to reconstruct these particle's tracks. At high energies, due to the kinematics of the interaction, a muon track will point in approximately the same direction as the original neutrino. This eventually allows to reconstruct the astronomical position of a potential neutrino source.

2.1.1 Neutrino interaction

Neutrinos are weakly interacting, so the only available interaction channels are via exchange of $W^{\pm}$ or Z vector bosons, i.e. via charged current (CC) or neutral current (NC) reactions, respectively. In neutrino telescopes, the interactions will always occur with nucleons of the surrounding matter, usually water or rock.

---

[1] When numbers are quoted in this section that depend on the detector material (ice or water) or on the detector site, they will be given for the ANTARES detector site in the Mediterranean sea as an example. This is done to give the reader a feeling for the approximate magnitude of these values. The overall principle, however, is the same for in-ice or in-water detection.

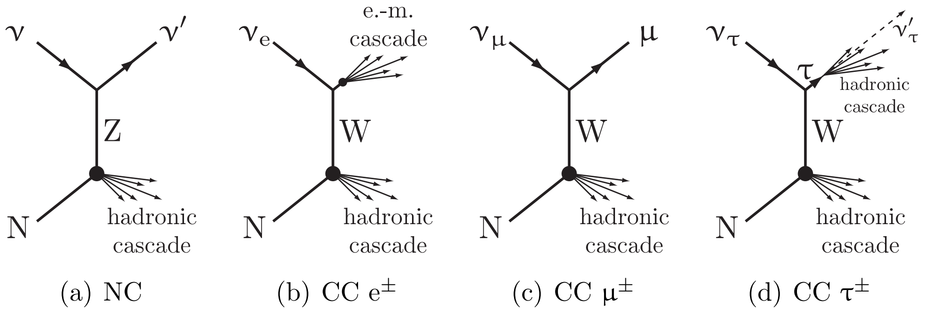

(a) NC (b) CC $e^{\pm}$ (c) CC $\mu^{\pm}$ (d) CC $\tau^{\pm}$

Figure 2.1 Illustration of the neutrino interaction channels visible to neutrino telescopes. A neutral current reaction resulting in a hadronic cascade and an invisible outgoing neutrino is shown in (a). Electron neutrinos reacting via the charged current yield an electron that immediately showers and forms an electromagnetic cascade overlaid to the hadronic one (b). Production of muons via CC is shown in (c), whereas (d) shows the reaction of tau neutrinos and the eventual decay of the τ into a hadronic cascade.

Due to flavour and charge conservation, the products of CC interactions depend on the flavour of the initial neutrino. The charged lepton's flavour in the final state will always be the same as the initial neutrino's flavour. So a ν_μ will yield a μ^-, an interacting ν_e will produce an electron and a ν_τ will produce a τ^-. This is of course also true for the respective anti-particles. In general, CC interactions can be written as

$$\overset{(-)}{\nu}_f + X \rightarrow f^{\pm} + X' \tag{2.1}$$

where f denotes the neutrino flavour and X stands for an arbitrary nucleon. The final state of this reaction includes the charged lepton and a hadronic part X' which will immediately lead to a particle cascade localised at the interaction vertex. Figure 2.1 shows (pseudo-)Feynman diagrams for these interactions.

The detector signatures of the three different neutrino flavours are therefore:

electron neutrino (ν_e) The resulting electron/positron only has a short free path length in matter and will produce high energy photons via bremsstrahlung. These photons can in turn interact with matter and again produce electrons and positrons via pair-production. This leads to an *electromagnetic cascade* which overlays the hadronic cascade. Such showers contain the whole energy of the neutrino and can be used for calorimetric measurements of the neutrino energy if they are located within the detector.

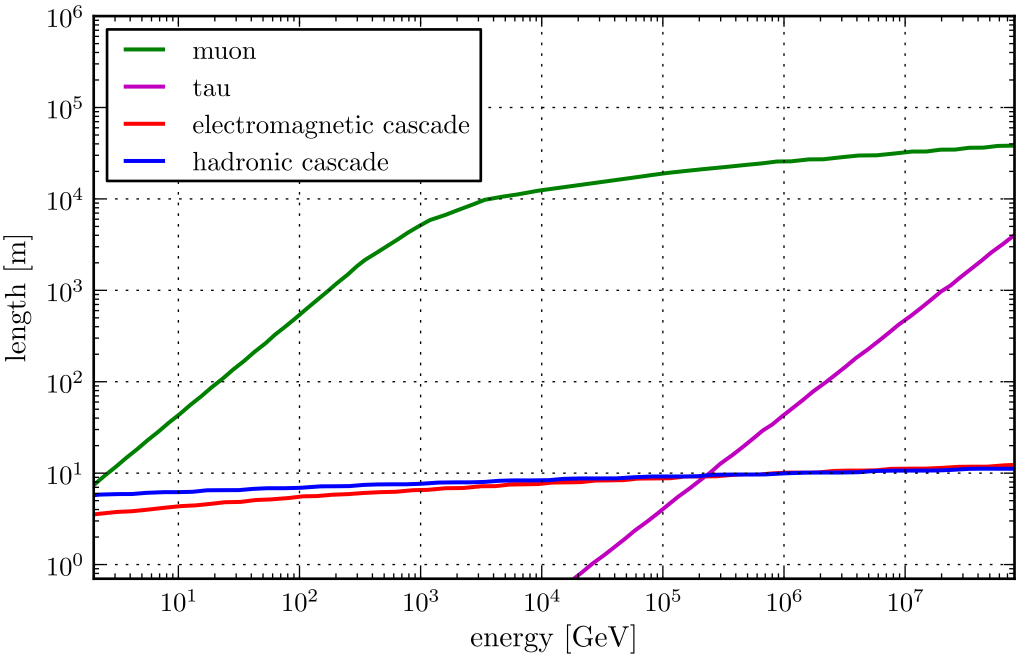

Figure 2.2 Mean Muon (μ) and tau (τ) path lengths and mean cascade lengths for electromagnetic and hadronic cascades in water. Data taken from [35].

muon neutrino (ν_μ) At energies of a few GeV, the path length of the resulting muon in water will be of the order of metres. It increases to over a few kilometres at about 1 TeV. The energy-dependence of muon path lengths is shown in figure 2.2. This means that most of the muon tracks visible in a neutrino telescope will have their vertex far outside the instrumented volume, which reduces energy resolution, but provides a much larger *effective detection volume* than the geometrical volume of the detector.

tau neutrino (ν_τ) The main signature of tau neutrinos is the so called *double-bang* structure, where a first particle shower is due to the hadronic cascade at the interaction vertex, followed by a second shower due to the decay of the tau. In case these two showers are by an appropriate distance separated, they can be detected individually.

As NC interactions are mediated by the neutral Z boson, the leptonic part of the final state has to be a neutrino with unchanged flavour.

$$\overset{(-)}{\nu}_f + X \rightarrow \overset{(-)}{\nu}_f + X' \tag{2.2}$$

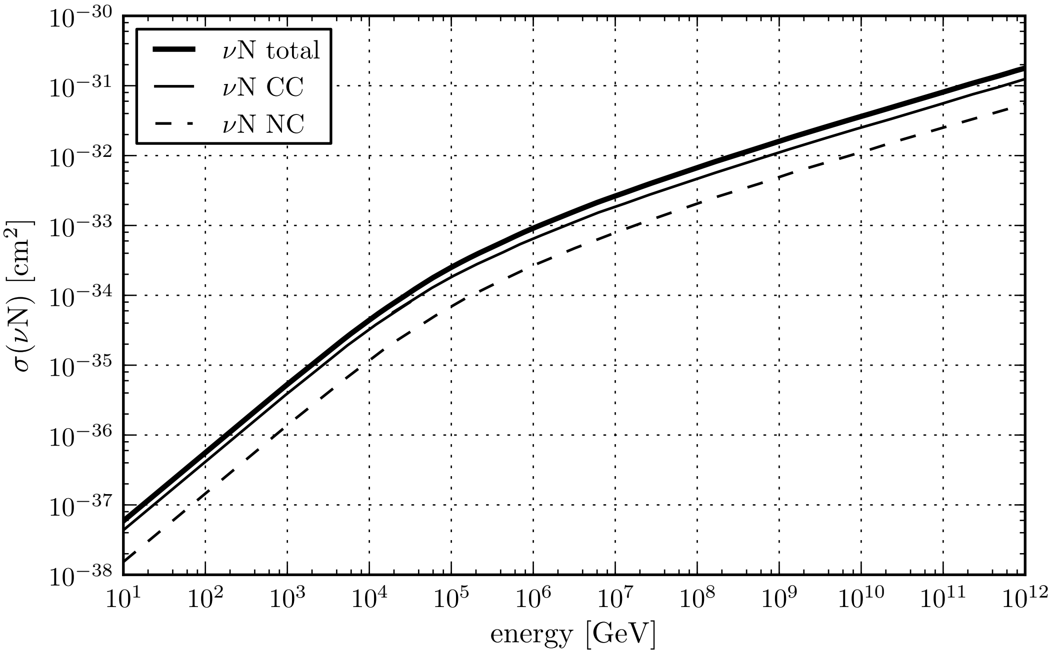

Figure 2.3 Cross sections for ν-nucleon-interactions according to the CTEQ5 parton distributions. Data taken from [36].

As the outgoing neutrino does not have a visible signature in the detector, only the hadronic cascade X' is seen, regardless of the neutrino flavour.

The following sections will only focus on CC reactions of muon neutrinos, as the design of neutrino telescopes is primarily focused on the detection of muons. Detection of all other interaction channels is possible, but because of their long lever arm, muon tracks provide the best angular resolution and therefore the best pointing accuracy.

Note that there is a small angle between the neutrino's direction and the resulting muon caused by the reactions kinematics. This angle does, however, decrease with energy, so that the angular resolution of the telescope above energies of a few 10 TeV is fully dependent on the reconstruction quality. Below this energy, the angular resolution is dominated by the neutrino interaction kinematics.

Figure 2.3 shows the neutrino cross-section in the energy range relevant for neutrino telescopes.[2]

---

[2] The Glashow resonance (i.e. W-production in anti-neutrino-electron scattering) at about 6.3 PeV is not included in the plot.

2.1.2 Cherenkov radiation from charged particles

Charged particles travelling through a transparent medium with a speed greater than the speed of light in that medium emit Cherenkov light [37]. It is this effect that allows neutrino telescopes to actually reconstruct muon track directions.

Cherenkov light is emitted on a cone with the emitting particle on its tip and with a characteristic opening angle θ_C depending on the particle's speed $\beta = \frac{v}{c}$ and the medium's refractive index n:

$$\cos\theta_\mathrm{C} = \frac{1}{\beta n} \tag{2.3}$$

For sea water with $n \approx 1.35$ and for highly relativistic particles (i.e. $\beta \approx 1$) the *Cherenkov angle* approaches $\theta_\mathrm{C} = 42^\circ$ and becomes independent of the particle's energy.

When neglecting changes in refractive index, the Cherenkov radiation's intensity is proportional to the emitted photon's frequency. As water is only transparent in a narrow band within the visible spectrum, most of the Cherenkov light is visible in the ultraviolet and visible range.

The number of photons emitted from a charged particle per path length can be written as

$$\frac{\mathrm{d}^2N}{\mathrm{d}x\mathrm{d}\lambda} = \frac{2\pi\alpha}{\lambda^2}\left(1 - \frac{1}{n^2\beta^2}\right), \tag{2.4}$$

where λ is the Cherenkov photon's wavelength and α is the fine-structure constant. In the wavelength range relevant for water-based neutrino telescopes of about 300 nm to 600 nm, the number of photons per track length is approximately

$$\frac{\mathrm{d}N}{\mathrm{d}x} = 3.4 \cdot 10^4\,\mathrm{m}^{-1}. \tag{2.5}$$

2.1.3 Muon propagation

A muon propagating through the detector volume can lose energy via ionisation, bremsstrahlung, pair-production and nuclear interactions. See figure 2.4 for an overview of the relative energy loss levels at different muon energies. Note the onset of the non-ionisation processes at an energy of about 1 TeV. Below this threshold, the muon energy loss is dominated by ionisation, which, at the resolution of current neutrino detectors, manifests as a quasi-continuous process along the muon track [39]. This energy loss mechanism does not have a strong dependence on the muon's energy and can be treated as a correction to the number of Cherenkov photons per track length (cf. (2.5)).

Starting at about 1 TeV, the muon starts to lose energy via bremsstrahlung and pair-production. At sufficiently high energies, these so-called *catastrophic* energy losses are visible as distinct electromagnetic showers along the muon track. It is

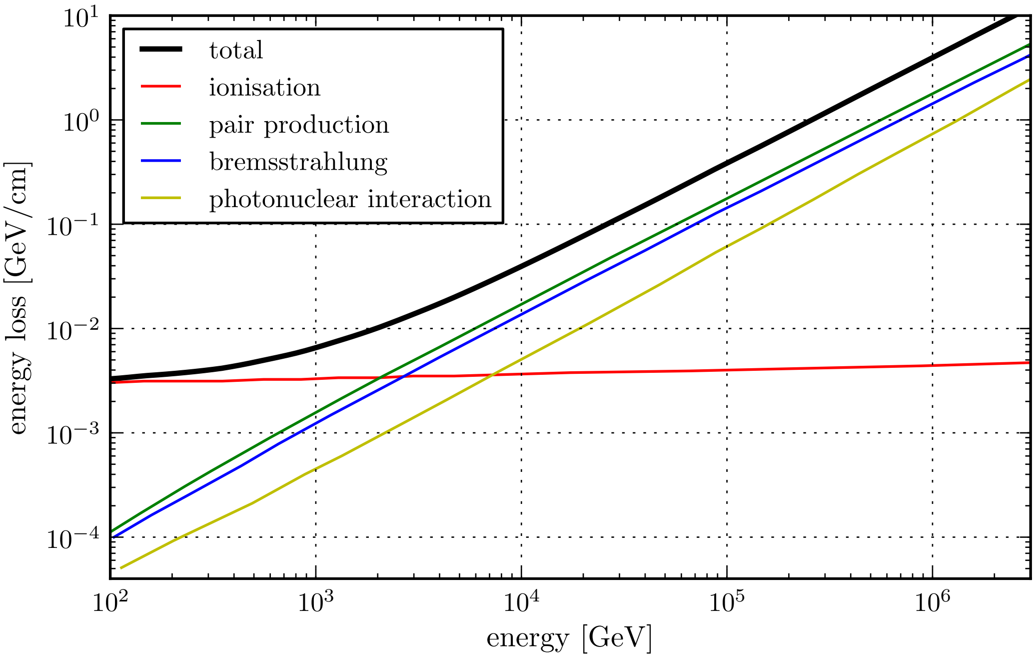

Figure 2.4 Energy losses of muons in water. The plot shows the losses by ionisation and by the stochastic processes (i.e. pair production, bremsstrahlung and photo-nuclear interaction). Data taken from [38].

specifically this type of energy loss that makes it possible to reconstruct a muon's energy as it passes through the detector.

2.1.4 Electromagnetic and hadronic cascades

As particle cascades consist of many particles with each of them having a rather short path length, their signature in Cherenkov light is different from that of muons: the Cherenkov cones of all charged particles within the shower overlap and lead to an effective angular light distribution that still peaks at 42° but is much broader than for muons. See figure 2.5 for an example. In addition, as the total length of showers is considerably shorter than that of muons, they will appear as point-like bursts of light in the detector, at least in first approximation.

Looking more closely, the total photon yield of a cascade and its mean length are proportional to its total energy E or to $\log E$, respectively. The energy dependence allows "calorimetric" energy measurements, which can help to determine a cascade's energy. Details on these parameterisations will be shown later in section 4.6.6.

The signature of hadronic cascades in the detector is very similar to that of electromagnetic ones. In first approximation, when applying simple corrections [39],

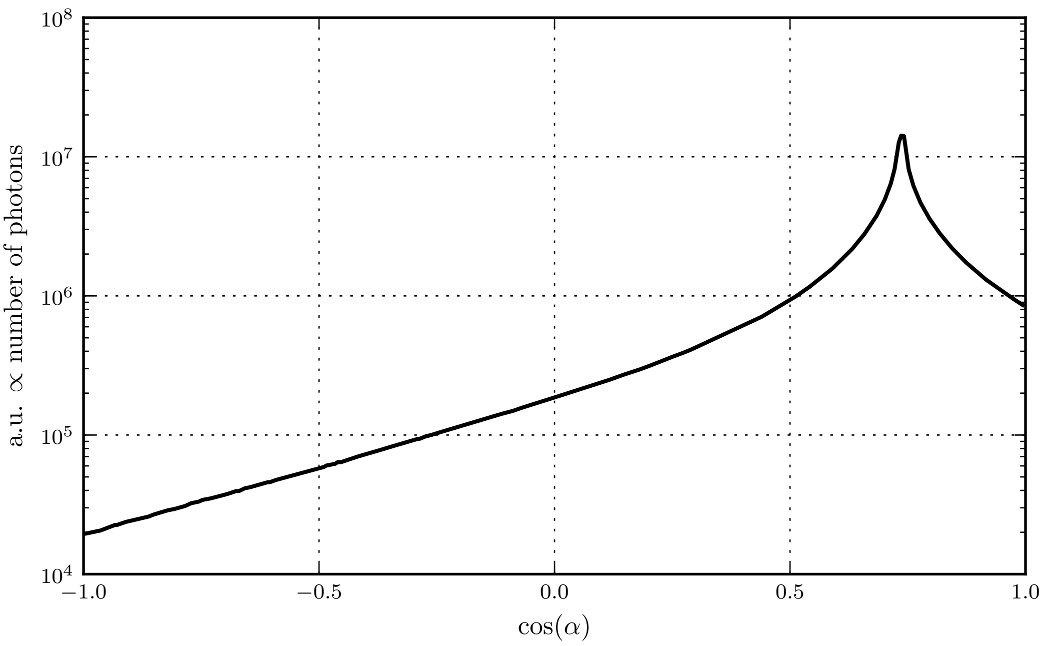

Figure 2.5 Angular profile of an electromagnetic cascade simulated with Geant4.

they can be treated like electromagnetic cascades, especially when parametric simulations are used that only simulate the shower according to its longitudinal and angular profiles.

2.1.5 Light propagation

As the position of measured photons and their arrival times are the only handles a neutrino telescope has on a muon track or shower, it becomes necessary to understand the influence of the surrounding medium on the Cherenkov light. Two effects need to be considered: absorption of light and scattering of light.

Absorption

Light absorption is characterised by the wavelength-dependent *absorption length* λ_a. It corresponds to the total track length at which the survival probability of photons has dropped to e^{-1}. Deep-sea water has its maximal transparency at about 470 nm. At this wavelength, measurements yield typical values of $\lambda_\mathrm{a} \approx 60\,\mathrm{m}$ [40].

Low absorption lengths necessitate a certain density of the detector instrumentation, as particles passing through sparsely instrumented detectors can simply be lost due to the fact that all their Cherenkov light is absorbed before it even reaches the detector.

Scattering

Scattered photons are one of the challenges in muon track reconstruction, as they will not be on the Cherenkov cone and thus do not point back to their emitting particle. The scattering properties of water are commonly described by a *scattering length* λ_s and a *scattering angle distribution* $\beta(\theta)$. For deep-sea water, these properties have been measured and parameterised. At a wavelength of about 470 nm, the scattering length is $\lambda_\mathrm{s} \approx 50\,\mathrm{m}$.[3] The scattering angle distribution (or *phase function*) can be described by a mixture of Rayleigh scattering and scattering on larger particles (Mie scattering). For details on the measured properties for the ANTARES site refer to section 2.2.3.

Speed of light in water/ice

As the arrival times of photons in the detector are crucial in reconstructing tracks, the speed of light in the respective medium needs to be known. The relevant speed is the light's group velocity, which is related to the medium's refractive index n by

$$v_\mathrm{g} = \frac{c}{n} + \lambda \frac{c}{n^2} \frac{\mathrm{d}n}{\mathrm{d}\lambda}. \tag{2.6}$$

Sometimes, a *group refractive index* n_g is defined, so that $v_\mathrm{g} = \frac{c}{n_\mathrm{g}}$. Substituting in (2.6) yields

$$n_\mathrm{g} = \frac{n}{1 + \frac{\lambda}{n}\frac{\mathrm{d}n}{\mathrm{d}\lambda}}. \tag{2.7}$$

Refractive indices in sea water have to be measured and depend on temperature, salinity and water pressure at a certain point. At 470 nm, typical values are $n \approx 1.35$ and $n_\mathrm{g} \approx 1.42$ (see [41]).

2.1.6 Light detection

Light detection in neutrino telescopes is typically done using a number of *optical modules* (OMs) consisting of photomultiplier tubes (PMTs) (and possibly readout electronics) in a spherical glass housing. The glass sphere protects the PMT from pressure and other environmental influences like salt water, while allowing Cherenkov light to get to the PMT's photocathode, where photons are subsequently converted into electrons. After an amplification stage, detected photons lead to an electrical

---

[3] This scattering length should not be confused with "effective" scattering lengths where averaging over scattering angles is included.

charge pulse which is read out using dedicated electronics. Detected photons are thus converted into a time and charge signature which is called a *hit*.

OMs are located on horizontal structures commonly called *strings*. They typically consist of a cable for mechanical support and data transport which has a number of OMs fixed to it. Depending on the level of expected optical background hits for a certain medium (see section 2.1.9), OMs are grouped in pairs, triples or other multiples on so-called *floors* or *storeys*. By looking for coincident hits within these nearby OMs, high background rates can be very well suppressed. This is especially true for all detectors located in sea water, as Cherenkov light from electrons produced by decays of ^{40}K lead to significant background rates.[4] For detectors in ice, a single OM per floor is sufficient, as there is no considerable background from radioactive decays.

More detailed information on the OM designs and readout schemes used by existing and planned telescopes can be found in sections 2.2 and 2.3.2.

2.1.7 Triggering

The readout of thousands of optical modules creates a huge amount of data that has to be filtered before it can be written to permanent storage for analysis. For this reason, *trigger* algorithms are applied. Such algorithms either operate on the continuous data stream arriving from the detector on shore or are implemented in the off-shore hardware. A trigger algorithm has to fulfil two requirements: it has to be able to split the data stream into discrete *events* and it has to filter all data between events that are not likely to contain any useful information.

There are a multitude of algorithms for triggering data. A simple, yet powerful algorithm, which looks for coincident clusters of hits in nearby floors will be described in section 4.10.4.

2.1.8 Muon track reconstruction

The information available for reconstruction of a muon track is a triggered event containing a set of hits. Each hit consists of a position in space (i.e. the position of the OM that recorded the hit), a timestamp and a pulse amplitude, commonly measured in multiples of the single photoelectron level.

Using information like the fixed Cherenkov angle and the speed of muons and light in water, the task of any reconstruction algorithm is to find a track that fits the given hit distribution.

There are several classes of track reconstruction algorithms:

---

[4] Another detector design possibility is to use more than a single PMT per OM be able to reduce background hits by using coincidences. Such a design will be presented in section 2.3.2.

Maximum likelihood fits Algorithms of the class use a probability density function (PDF) that, according to a given track assumption, assigns a likelihood value to each recorded hit. Calculating the product of all likelihood values yields an overall likelihood for a certain track assumption.[5] The algorithm then varies the track parameters in order to find the highest possible likelihood value. It finally returns the track with the best parameters as the reconstructed track.

The most important part in a PDF is the difference between the theoretical hit time calculated from the track assumption and the recorded hit time. But other data like hit amplitudes and OM directions can also be used to further improve the quality of the reconstructed tracks.

χ^2 fits These algorithms work similar to maximum likelihood methods in that they minimise a function that depends on a certain track assumption. In this case the function is a quadratic sum over time differences between recorded and hypothetical hit times, with each time difference divided by its uncertainty.

$$\chi^2 = \sum_i \frac{(t_{\text{rec.}} - t_{\text{hypoth.}})^2}{\sigma_i^2} \tag{2.8}$$

A minimisation algorithm then finds a minimal value of χ^2 by varying the track parameters. The track with these parameters is returned and used as the fit result.

geometrical fits/pre-fits These algorithms are usually used for pre-fits, with their results being used as a starting point for the likelihood or χ^2 minimisation routines. Most geometrical fits simplify the procedure by, for example, assuming that a track responsible for a hit goes exactly through the OM in question. This allows for a fast first-guess track estimate, which is usually not very good but better than a purely arbitrary starting point.

2.1.9 Background

No measurement can be free of background, which is especially true for neutrino telescopes. The rate of hits that are not due to cosmic neutrinos is much larger than the number of hits produced from the signal events.

Background light can be due to various sources. The most important of these sources will be described in this section, together with possible measures to reduce their contribution.

---

[5] For numerical reasons, most algorithms do not calculate the product of all likelihood values P_i but rather the sum of $\log P_i$. Hence, these algorithms are sometimes called *log-likelihood* methods.

Optical noise

An overall optical noise rate is the main background source for unfiltered data in sea-water-based detectors. This noise is due to two sources:

^{40}K decays The salt contained in sea-water includes a small amount of the radioactive isotope Potassium-40 (^{40}K), which decays through β-decay with a branching ratio of 89.3% ($^{40}\mathrm{K} \rightarrow {}^{40}\mathrm{Ca} + \bar{\nu}_e + e^-$). The resulting electrons have an energy of about 1 MeV, which is sufficient to produce Cherenkov light. A second decay channel with a branching ratio of 10.5% is the decay to ^{40}Ar, either by electron-capture or by positron emission. The resulting ^{40}Ar nucleus is in an excited state and can thus emit a photon with an energy of about 1.5 MeV, which in turn can produce electrons via compton-scattering. These electrons can also possibly create Cherenkov light if their energy is high enough. These decays add up to a total rate of about 100 Hz per cm^2 of photocathode area.

Bioluminescence As the deep sea is by no means a dead environment, it contains a large number of life forms, ranging from microscopic life-forms to larger animals including fish. Several of these organisms emit light in a broad range of wavelengths. This light is seen in the detector's PMTs as two different contributions. One is a slowly-changing *baseline* rate that causes noise hits that just overlay the ^{40}K noise. On top of this, *bursts* of noise with durations of up to a few seconds can be seen. The ANTARES collaboration measures a baseline noise rate in the range of about 60 to 120 kHz with rates of over a MHz during bursts.

Bioluminescence is subject to a noticeable seasonal variation, depending on sea currents and the vertical movement of nutrient-rich water from warmer layers down to the depths of a detector [42]. During spring, baseline rates of up to several MHz have been measured by ANTARES. However, as these rates have not been measured each year during the operation of ANTARES, seasonal variations do not seem to be the only factor influencing the bioluminescence rate.

Optical noise can affect the reconstruction performance of neutrino telescopes, as the chance of a series of noise hits accidentally looking like a muon event rises with the noise rate per PMT. This is especially true for muons with energies below 1 TeV, where only a few photons are seen. In addition to such fake events, an excessive amount of noise hits can mask hits from a real event.

One way to suppress noise hits is to look for coincidences in neighbouring PMTs, as already described in section 2.1.6. The probability for random coincidences by ^{40}K or bioluminescence hits is low. Another possibility is to only use hits above a certain amplitude threshold: photons from ^{40}K decays generally have amplitudes corresponding to a single photoelectron, whereas signal hit amplitudes can have higher amplitudes, at least at higher muon energies. This basically corresponds to a coincidence within a single PMT. The actual probability for a noise coincidence leading to a hit with higher amplitude depends on the length of the integration time window defined by the readout electronics.

Atmospheric muons

Cosmic rays reaching earth's atmosphere with enough energy will produce extensive air showers. Due to their hadronic nature, these cascades will contain a significant number of muons, many of them reaching the detector from above. The flux of these muons is significantly higher than the expected flux of muons due to neutrino interactions.

As a an air shower usually produces more than one muon, most of these muons arrive at the detectors in bundles. This background type is the main reason to build neutrino detectors at deep sea sites, as the sea water above the detector acts as a shield against these muons. But, even at large depths, atmospheric muons are the most common events seen in the detector.

Therefore, neutrino telescopes predominantly look at up-going muons, thus using the whole planet as a muon shield. This requires a robust track reconstruction algorithm which minimises the fraction of mis-reconstructed tracks. Bundles of muons or even two coincident muons from separate air showers can lead to signatures in the detector that closely resemble these of up-going muon tracks.

Looking downwards will only work up to an energy of about 1 PeV, as above this energy, the earth starts to become opaque for neutrinos. See figure 2.6 for an overview of the neutrino interaction lengths vs. energy compared to the earth diameter. Simulations for the ANTARES detector [45] show, however, that the atmospheric background rate is low enough at these energies to allow reconstruction of such high-energetic tracks even if they are only seen from above the horizon.

Atmospheric neutrinos

Hadronic air showers do not only produce muons. Decays of charged pions and kaons also yield a large flux of high-energetic neutrinos, which will be visible to a neutrino detector on top of the flux of cosmic neutrinos signal. These *atmospheric neutrinos* present an irreducible background for the measurement of any cosmic neutrino. However, as can be seen from figure 2.7, the energy spectrum of atmospheric neutrinos is much softer than the signal spectrum expected from cosmic sources. In that way, signal events will manifest as an excess of events measured at higher energies. For point-source searches, the expected neutrino direction is already known, so a

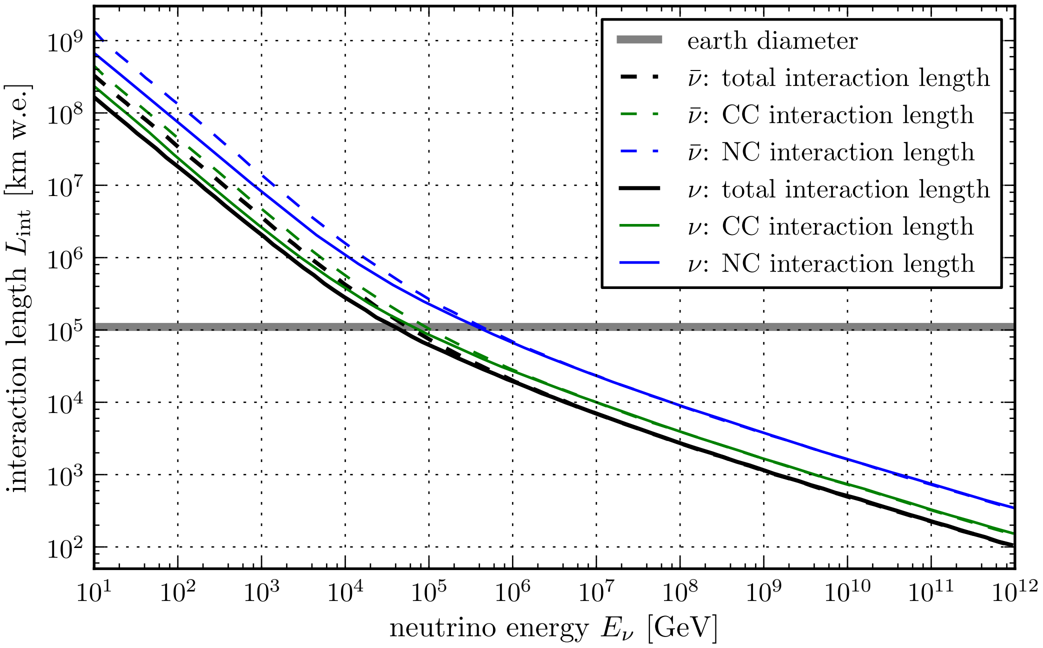

Figure 2.6 Interaction lengths for (anti-)neutrino-nucleon interactions in km water equivalent. Data taken from [43]. The earth diameter has been calculated using the earth density profile cited in [44].

large amount of background events can be eliminated by simply requiring events to be contained in a pre-defined space angle around the source direction.

In addition to the *conventional* neutrino flux due to pions and kaons, there is a secondary flux component due to decay of charm particles called the *prompt* flux. Whereas the different models for the conventional flux are more or less in agreement with each other, this is not true for the prompt flux models. Note that, beginning from approximately 100 TeV, the prompt flux component starts to dominate. As this is the energy region where diffuse neutrino flux searches are focused, a calculated detector sensitivity will depend on the choice of flux model. This work uses the *bartol* model [46] for the conventional flux and the *Naumov RQPM* model [47] for the prompt flux. This particular prompt flux model yields rather high fluxes and is thus conservative.

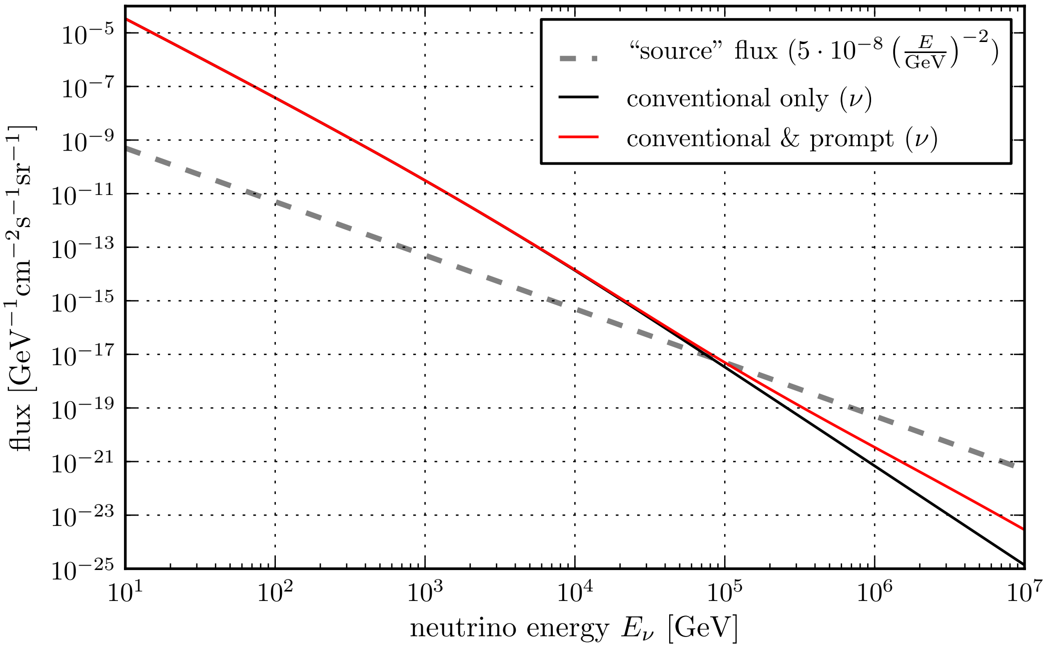

Figure 2.7 Atmospheric neutrino spectrum calculated using the "bartol" model with and without a prompt contribution according to the "Naumov RQPM" model. The anti-neutrino spectrum looks similar and is thus not shown for clarity. An E^{-2} "source" spectrum is included for comparison.

2.2 Existing neutrino telescopes

This section will give an overview of the currently existing and operational neutrino telescopes. However, before introducing the currently running neutrino telescopes, the DUMAND project [48] has to be mentioned. It was the first deep-sea neutrino telescope project, starting its planning phase around 1976. The detector location was in the Pacific Ocean near Hawaii's Big Island. Although the project's funding was eventually cancelled in 1995 due to technical difficulties with their deployed hardware and the detector was never fully built, DUMAND did a lot of fundamental work for the neutrino astronomy community.

2.2.1 Baikal

The neutrino telescope in Lake Baikal [49] started with 36 OMs on three detector strings which were deployed in 1993. Deployment and detector maintenance is generally done in winter, when the lake freezes over. This allows cost-effective access to the detector with winterproof vehicles. The second advantage of using Lake Baikal

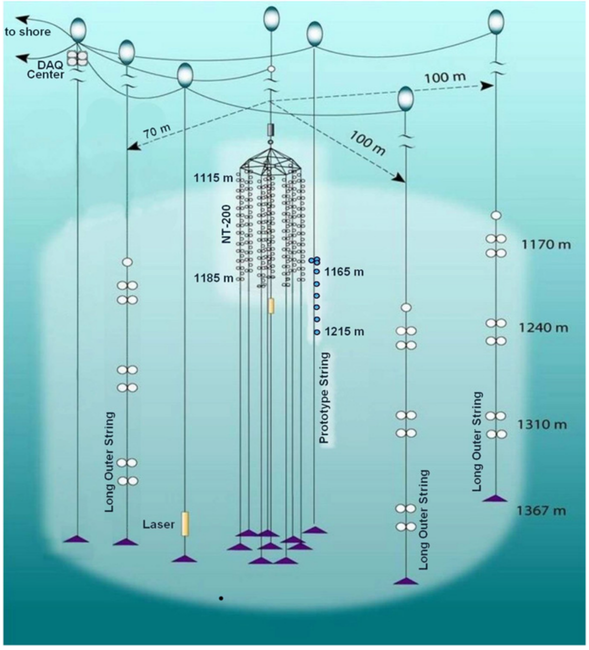

Figure 2.8 The Baikal neutrino telescope “NT200+” as of 2008 with its compact centre array (“NT200”) several extra peripheral strings. Taken from [49].

as detector site is the low concentration of ^{40}K in its water. It is a fresh water lake as there are several rivers draining into it and one river coming out of the lake. The lower optical noise is however outweighed by the rather short light absorption length ($< 20\,\mathrm{m}$) when compared to deep-sea sites. Additionally, the relatively low depth of the detector site of only about one km leads to a high flux of atmospheric muons.

Nevertheless, the Baikal experiment was the first deep-water neutrino telescope to detect several neutrinos. It has been continuously extended with additional strings. Its current iteration *NT-200+* is shown in figure 2.8.

2.2.2 IceCube

The IceCube detector [50], currently under construction at the south pole, is the first neutrino detector with a volume approaching $1\,\mathrm{km}^3$. At the time of this writing, more than half of the detector is completed and data-taking is well underway. Sharing its South Pole site, IceCube’s predecessor AMANDA pioneered in-ice neutrino detection and is integrated with the IceCube data acquisition system. However, AMANDA has recently been turned off, leaving IceCube as the only neutrino telescope in the Southern hemisphere.

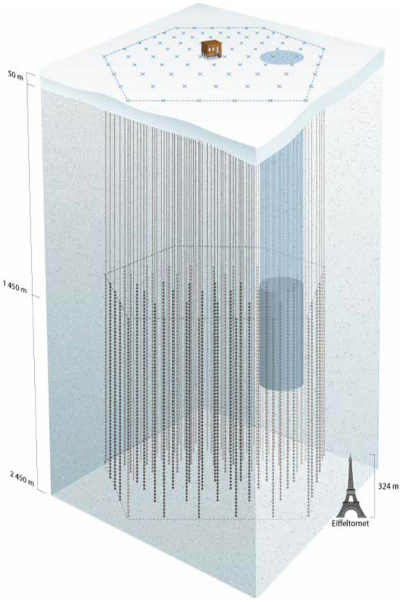

Figure 2.9 Schematic of the IceCube detector. Taken from [50].

IceCube consists of 80 strings with 60 downward-looking optical modules per string and one module per floor. The floor spacing is 17 m, between 1450 m and 2450 m below the surface. The strings are arranged on a hexagonal grid with a spacing of 125 m. The layout can be seen in figure 2.9.

Due to its location in the antarctic glacial ice, there is almost no optical background noise from either ^{40}K or bioluminescense. It is for this reason that a single OM per floor is sufficient, as no hit-coincidence filtering is necessary as it would be for a water-based detector. The antarctic ice has a much higher absorption length than water, but its scattering length is relatively short. The ice properties are highly depth-dependent, the ice being mixed with impurities that were contained in the atmosphere at the time a certain ice layer first formed.

2.2.3 ANTARES

The ANTARES detector is the first completed deep-sea neutrino telescope. It is located in the Mediterranean Sea, 40 km off the French Coast at a depth from 2500 m to 2052 m. It consists of 12 strings, each with 75 optical modules distributed in triplets on 25 floors per string. All optical modules are pointing downwards at an angle of 45° with respect to the horizon. The vertical floor spacing is 14 m with floors starting to be instrumented 100 m above the sea floor. It has a total number of 885 OMs, with 5 floors equipped with acoustic neutrino detection R&D setup instead

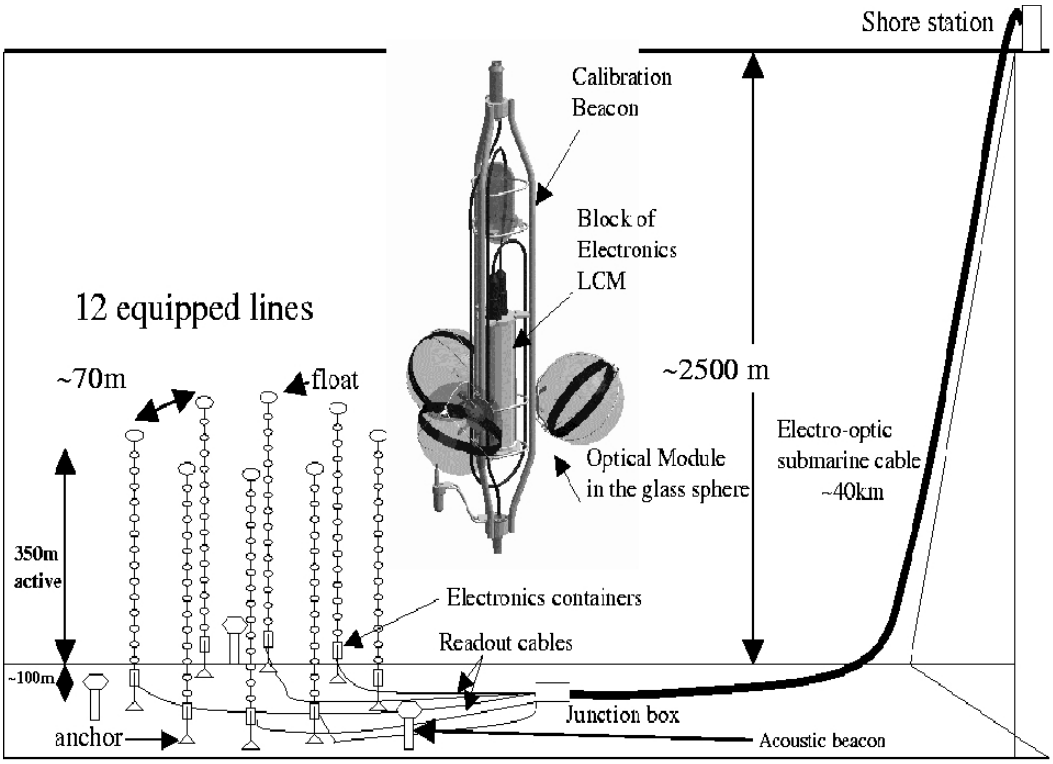

Figure 2.10 Schematic overview of the ANTARES detector. Official ANTARES plot.

of optical modules. See figure 2.10 for a schematic of the detector. The detector is connected with a shore station using an electro-optical telecommunications cable, capable of transmitting multiple optical GBit feeds.

The ANTARES collaboration performed detailed site studies, leading to a fair understanding of the detector medium. It is these water properties that have been used in all simulation studies for this work. Refer to section 4.5.1 for the actual medium property values.

The ANTARES readout is performed by a application-specific readout chip, the “analogue ring sampler” (ARS) [51]. This chip reads out the integrated photomultiplier signal once it rises above a certain configurable threshold. The default integration time is 33 ns with a consecutive dead time of 250 ns. To compensate for this, the chip contains a second, similar channel with the same integration and dead times, which is used if the first channel is processing data. There is a short switching time from one ARS channel to the other of 7 ns. The default pulse integration threshold is at a level of about 0.3 photoelectrons. The ANTARES readout is equipped with an optional waveform pulse readout, which is currently only used for calibration purposes.

The detector's trigger scheme uses an all-data-to-shore strategy, i.e. all hits above the integration threshold are sent to shore without any further filtering. The actual event building and triggering is done in an on-shore computer cluster. This allows for a rather flexible trigger design, as no hardware changes are necessary in case an improved triggering algorithm becomes available.

2.3 The KM3NeT project

2.3.1 Overview

The KM3NeT project is a joint effort of the ANTARES collaboration and the other collaborations currently designing Mediterranean neutrino telescopes, namely NEMO [52] and NESTOR [53, 54]. The project's aim is to construct a detector with a volume larger than $1\,\mathrm{km}^3$ in the Mediterranean Sea to complement the IceCube project in the Southern hemisphere. At the time of this writing, the project is completing its initial Design Study Phase, a "Conceptual Design Report" (CDR) has been written [55] and a final "Technical Design Report" (TDR), describing options for the final detector design, is in press.

This work is concerned with the development of a new simulation toolchain, independent of the original ANTARES tools, which have been used for a large fraction of the studies on KM3NeT. It is currently not clear which final design choices will be made for KM3NeT, so the simulations are performed for several example detectors which were design possibilities at the time of this writing.

As the TDR was not in existence when the simulations for this work were started, the following design choices may not coincide with the choices finally made for KM3NeT. Thus, none of the results in this work were either endorsed by the KM3NeT Consortium nor do they represent any official result.

2.3.2 Design possibilities

From a technical point of view, there are three competing overall detector design choices that are possible for KM3NeT, re-using part of the knowledge gained from the respective predecessor projects.

The "string" design

The "string" design used in this work shares most of the detector properties with the original ANTARES detector. To achieve a larger detector size at manageable cost, the string and floor distances have to be increased with respect to ANTARES.

Common floor distances are of the order of 30 m to 40 m, whereas string distances are increased to be larger than 100 m. As the hit coincidence condition is based on the OM distances on a floor, it does not need to be changed from its ANTARES values. In fact, the whole ANTARES readout simulation scheme can be used as-is, including the two-channel ARS chip.

The "tower" design

An alternative design is to fix the optical modules on large metal bars, a design choice pioneered by the NEMO collaboration. In the design that will be used for this work, three pairs of optical modules will be fixed on both ends and in the middle of each bar with a length of 8 m. As in this design each vertical detection unit looks more like a tower of bars instead of a string of OMs, the name "tower" design will be adopted for it from now on. Like the "string" design, the ANTARES concept with a single photomultiplier per OM is used.

Building tower-like detectors with only OM pairs instead of triplets decreases the number of detected hit coincidences for each pair. However, it has a non-negligible advantage at high tower distances, as the three pairs of optical modules on each bar are indistinguishable from three separate closely-spaced strings if shadowing effects are not taken into account. Thus, at low muon energies, where the track lengths are short and a single line may not be sufficient to fully reconstruct a track, the tower design provides a gain in detection efficiency while at the same time keeping technical deployment problems with closely spaced strings at a minimum. In this work, the OMs used for the tower design are the same as for the string design. This includes the PMT type and readout choices.

The "multiPMT" design

The third design tries to change the "single-PMT-per-OM" paradigm by using a number of smaller PMTs per OM instead. The specific "multiPMT" design [56] used in this work has 31 PMTs with an effective diameter of 76 mm fitted into an OM sphere with a diameter of 432 mm, the same size currently used for ANTARES. In this design, the use of multiple OMs per floor becomes unnecessary, so it only consists of single OMs per floor, similar to IceCube.

Due to its simplicity with only one OM per floor, strings for the multiPMT design are cheaper to build, which allows to deploy more of them. This compensates for the lower total photocathode area per string in these designs. Additionally, the number of under-water connectors is minimised in this design, eliminating a potential source of failure during the detector's lifetime. Having such a large number of small PMTs in a single OM also allows the detector to have a finer-grained single photon resolution. Finally, it may even be possible to reconstruct a Cherenkov light front's direction from the data of just a single OM. The readout scheme used for such multiPMT OMs is a time-over-threshold approach, which will be described in more detail in section 4.10.3.

2.3.3 Detector sites

As each of the predecessor projects of KM3NeT performed site studies in different places around the Mediterranean Sea, three different site possibilities emerged: off the French coast near Toulon (depth 2475 m), at the *Capo Passero* site near Catania (depth 3500 m) and near Pylos in the East Ionian Sea (depth between 3750 m and 5200 m). These sites have very different maximum depths, influencing the atmospheric muon background rate. The studies for this work have all been done for a depth of 3500 m.

Part II

Methodology

3 Software simulation and reconstruction tools

> Computer Science is no more about computers than astronomy is about telescopes.
>
> *(Edsger W. Dijkstra)*

Neutrino detectors would not be possible without computer-based simulation and reconstruction tools. As the sheer amount of data collected by any telescope cannot possibly be handled by hand, sophisticated filtering, triggering and reconstruction algorithms have to be implemented in software to reduce and convert the recorded raw data to datasets suitable for a physics analysis. In addition, Monte Carlo simulation tools are necessary for understanding the effect of detector systematics and to be finally able to interpret the data recorded by a detector. Especially during the design phase of KM3NeT, where no real working detector does exist, Monte Carlo simulations are the only way to properly compare different possible design options and to evaluate their physics potential.

This chapter describes the Monte Carlo simulation tools used to produce all data presented in this work. First, the legacy software toolchain from the ANTARES project, which is currently in use for most KM3NeT studies, is presented. The remainder of this chapter introduces the concept of a *software framework* and presents *IceTray*, a framework developed by IceCube. During the course of this work, IceTray was adapted for KM3NeT and ANTARES. This chapter covers all direct ports of ANTARES algorithms to IceTray and the most important modules that could be reused from IceCube without major changes. Note that some of the simulation-centric IceCube modules are covered in more detail in chapter 4.

3.1 Legacy software tools from ANTARES

The software that has been in use by ANTARES for the last decade consists of a suite of independent software tools [57] loosely linked by an ASCII-based text file format [58, 59]. Data processed by one tool is written to disk in a common file format that can then be read by the next tool in the processing chain. The relevant tools for simulation and reconstruction of muon neutrinos are:

gendet, a tool for detector layout generation [60, 61]. It takes a set of sea floor coordinates and a string template description. The template contains the floor positions on the string and a floor description specifying the OM positions on the floor and their orientations. From these data, it generates a *detector file* containing the position and orientation of each OM in the detector. Optionally, a sea current which distorts the strings from their vertical orientations can be simulated. The *gendet* tool does not directly support non-string detector layouts (i.e. “tower”-type detectors). Such layouts can, however, be generated by configuring bar-like floors on each string. In this way, the final OM positions will be compatible with the “tower”-layout as long as no sea current is simulated. Because all further simulation and reconstruction steps only work on the OM level and do not use the string cable positions, this approximation is sufficient for KM3NeT studies.

genhen, a neutrino event generator [62–67]. Neutrinos are generated with a user-defined energy spectrum and propagated to a cylindrical volume around the detector called the *generation volume.* Inside this volume, each neutrino is forced to interact and the actual interaction probability is recorded. All muons resulting from these interactions are then propagated, taking into account their energy losses in rock and water. The generation volume is chosen as a cylinder encompassing all strings (the *instrumented volume*) and extended by the maximum muon length at the maximum neutrino energy used for the simulation, limited by the sea surface.

In case one of these muons reaches a second, smaller cylindrical volume around the detector, the whole reaction including neutrino and muon is recorded as an event. The size of this *sensitive volume* has to be chosen so that muons that do not intersect it will only have an extremely small probability of being seen by the detector. The standard ANTARES approach is to extend the instrumented volume by three Cherenkov light absorption lengths. The *sensitive volume* is sometimes called the *can* in ANTARES jargon.

The *genhen* generator simulates neutrino interactions with LEPTO [68]/CTEQ6 and RSQ [69], for deep inelastic scattering and for resonant/quasi-elastic events, respectively. Muons are transported to the *can* using either the MUSIC [70], MUM [71, 72] or PropMu [73] algorithm.

The implementation of *genhen* is generic and can be used for KM3NeT detectors with only minor technical changes.

km3, a muon and Cherenkov light propagation implementation [74, 75]. The *km3* package performs muon tracking within the sensitive volume, takes care of generating Cherenkov photons and of propagating them to the optical modules. Muon tracking is performed by the MUSIC library [70], which provides *km3* with information about the energy loss profile along the particle’s track. Electromagnetic showers are then placed along the track according to this profile. In a second step, light from the "bare" muon and from each of the showers is propagated to the detector's OMs, taking into account scattering and absorption of light in sea water.

As simulating each single photon would take far too much CPU time to be feasible for Monte Carlo mass productions, an alternative approach using pre-simulated photon tables is used: Photons are only simulated once using the Geant3 [76] based helper tool *gen*, which records the light output of a short muon segment (with a length of about 1 to 2 m) or of an electromagnetic shower on concentric spheres. Several of these spheres are placed around the emitters at different distances. All photons intersecting the spheres are recorded. A second helper tool, *hit*, subsequently divides these spheres into angular bins and converts the photon fields into tables containing hit probabilities. These probabilities include the OMs' characteristics such as their angular acceptance and their wavelength-dependent quantum efficiency. Thus, the photon tables produced by *hit* contain the full set of OM properties and have to be re-calculated for each type of OM that is to be simulated.

The actual *km3* program then takes care of calling the MUSIC library to propagate muons and of creating hits according to the pre-generated tables from *hit*. The muon segments are combined into a whole muon track. Each time the energy loss is above a configurable limit (which is set to the ionisation loss), a secondary shower is placed at this position on the track. Hits on each OM are sampled from the tabulated probability distributions for each segment and shower. Optionally a white noise background per OM can be added, approximating the ^{40}K and bioluminescence rate. All OM hits can additionally be converted into readout pulses using a simplified PMT and electronics simulation targeted at ANTARES OMs. See [74] for more details on the actual implementation of the *km3* suite of simulation tools.

geasim, a full tracking Monte Carlo code based on Geant3 [76]. This tool provides the same functionality as *km3*, with the exception of light scattering. It does not use a table-based approach, but rather simulates each particle using the full Geant3 engine. To be reasonably fast, light is only propagated in straight lines, which enables the code to speed up processing by a fair amount, as most photons can simply be rejected by simple geometric considerations: a photon with a straight path that can never hit an OM can be rejected early in the code. This is of course only true if light scattering is neglected. As *geasim* is still quite slow when simulating very long muon tracks, it is mainly used for the hadronic part of neutrino interactions near the vertex. It can be combined with *km3* by using a special mode where only the hadronic component is simulated by *geasim*, whereas the muon is simulated by *km3*.

reco, a track reconstruction tool containing a number of reconstruction algorithms, including the current standard ANTARES reconstruction strategy [77]. This strategy has been ported to the software framework described in the following sections. It consists of a chain of likelihood-based fitting routines. A detailed description can be found in section 4.11.1.

As they were initially designed for use with ANTARES, several of these tools required minor technical modifications to be usable for simulations of KM3NeT detectors. This included changing of some hard-coded numbers and array sizes and the implementation of dynamic OM types [78].

3.2 Software frameworks

A major physics experiment like the KM3NeT neutrino telescope requires an immense amount of hardware development effort. However, to make use of the telescope, software that allows running the experiment and, most importantly, to transform the raw data to high-level physics information is also needed. Such software cannot be written by a single person, but has to be created in a collaborative effort.

A software developer should not need to know every single line of code of a particular program to be able to extend it. Most of the time, the task is to implement or change a single algorithm only, without modifying the rest of the reconstruction software. It is thus necessary to write modular code with a predefined data flow from the very beginning. Such program modularisation and the definition of a corresponding data flow are the essential elements provided by a *software framework* [79].

3.2.1 The concept of a software framework

A possible definition of a software framework can be: a software framework is a set of rules, interfaces and services provided to a software developer, who can use it to perform a set of tasks.

In a modular framework, the user should only have to change a few lines in a steering file to modify an analysis chain. This is illustrated in figure 3.1: An existing analysis is changed by adding a further module.

Frameworks should not be confused with class libraries. A class library, like a framework, provides a set of interfaces and services. It does not, however, enforce a particular program structure and leaves it to the individual programmer's code to specify the structure. A framework defines an overall program pattern, which makes it easy to extend: a developer implements algorithms, whereas the framework specifies how their implementations interact.

Typically, frameworks enforce this overall design. At the same time, they must avoid being too restrictive, to allow for the necessary freedom to developers and

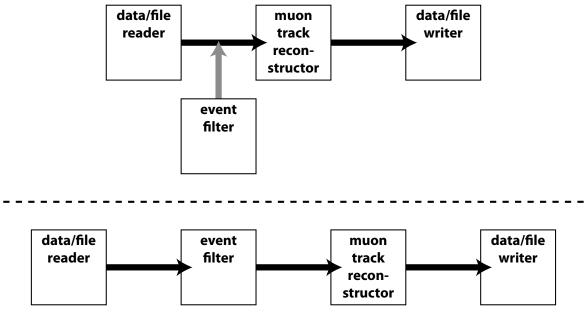

Figure 3.1 Simplified reconstruction chains consisting of *modules*, with data flowing from one module to the next one. The first chain consists of three modules. In a framework, tasks like adding modules can easily be performed. In this example, an event filter is inserted at a particular point in the first chain. The resulting reconstruction chain is shown below the dashed line.

end-users.[1] This is achieved by using a modular approach, where each subsystem can be modified, added or replaced without altering the others.

Using a framework saves the physicist a lot of time in learning how to use a particular software package every time s/he wants to perform a new task on a set of data. All algorithms are implemented in modules having the exact same structure. This makes the code easier to read and understand. The software user can thus start to work on physics problems with a significantly shorter learning period.

A modular structure also leads to more flexibility. Systematic analyses can be performed more easily, as the high-level program flow and all fine-grained module parameters are always visible to and changeable by the framework user.

Finally, frameworks facilitate the collaboration between different groups doing software development. As all modules have the same format, they can be easily exchanged. This is especially advantageous when doing cross-checks and also helps implementing an overall quality control scheme: Code that is broken down into small independent units can be more easily reviewed by others than a single monolithic program.

---

[1] In an object-oriented language like C++, a particular design can be enforced by using the concept of *encapsulation*: the inner workings of a class should always be hidden from other classes. Another important concept, called *polymorphism*, allows the framework to be extended in a well-defined way: only a small set of abstract classes is exposed from the framework. These classes are then overwritten when implementing an algorithm.

3.2.2 The IceTray framework

IceTray [80], the software framework developed and used by the IceCube collaboration [50], provides all the features mentioned in the previous section. Developers create *modules*, which can be dynamically linked into the framework. They contain the actual algorithms responsible for event reconstruction or simulation. Data is passed from module to module in data containers called *frames*. Each frame typically describes a single event. A frame consists of a list of name-object tuples. Except for an I/O method, there are no requirements imposed on the objects stored in a frame. This design decision makes the framework easily extendable.

The framework already provides modules for reading and writing of data. These modules can be used at any time in the reconstruction chain, so that data can be written out at any stage. Though IceTray uses its own data format based on routines from the *boost.org* libraries [81], it is possible to write reader modules for any other data format. This has been demonstrated by providing a reader module for standard ANTARES ROOT-files as produced by the current ANTARES online data acquisition (DAQ) system [82]. It should be noted that, in principle, the framework does not require to write out any intermediate data, as data input and output is done in dedicated modules. A full Monte Carlo simulation of events and their reconstruction can thus be done in IceTray without ever writing temporary files to disk. Of course it is still possible to produce intermediate data files.

The order of modules can be defined when initialising the framework. This is typically done using the *Python* scripting language [83]. In addition to Python, compiled C++ code can be used to control IceTray module chains.

IceTray comes with *dataclasses*, containing class definitions usable for storing positions, directions, particle tracks, optical module (OM) properties and all other data necessary during event reconstruction and simulation. These classes are usable for KM3NeT with only minor modifications. These modifications are mostly necessary because the developers of IceTray assumed that all OMs would look either vertically downwards or upwards. This is true for IceCube, but assumedly not for KM3NeT.

A few simple non-physics modules, such as a generic event selector template and a ROOT tree writer can also be re-used for KM3NeT. None of these helper modules contain any physics-relevant code.

3.2.3 Simulation and analysis tools for KM3NeT within the IceTray framework - "SeaTray"

To enable IceTray to work with the data that is currently available, a considerable fraction of the code from the ANTARES experiment, was modularised during the course of this work. Most of these modules can also be used for KM3NeT without major changes, although some modules are targeted specifically to ANTARES and were only implemented to show the feasibility of using IceTray for water-based detectors. They are, however currently in active use for other projects [84–86]. The work done on the framework and the implementation of all modules has ultimately led to the adoption of IceTray as the official software framework for both ANTARES and KM3NeT.

In addition to straight ports from ANTARES, new modules have been implemented which are targeted specifically to the simulation of different proposed KM3-NeT detector designs. The whole distribution of the framework core together with all KM3NeT/ANTARES modules is referred to as "SeaTray", whereas the framework itself is still called IceTray.[2]

This section will give an overview of all modules that could be re-used from IceCube and of all modules that were ported or re-written from existing ANTARES code. It will not cover modules that were developed specifically for this work, as these are presented in full detail in chapter 4.

Ports and rewrites from the ANTARES toolchain

As part of this work, several modules have been ported to IceTray from their original implementation in the ANTARES toolchain. This includes a DAQ file reader module together with database access services necessary for reading real detector data files. These modules were implemented to demonstrate the applicability of IceTray to neutrino detectors beside IceCube and can be disregarded for this work.

In addition to that, a module that permits reading the standard ANTARES Monte Carlo file format was developed. It enables the user to read data produced by the standard ANTARES Monte Carlo packages described in section 3.1. Thus, all of the currently existing Monte Carlo tools can be used with IceTray.

Environmental background hits (from ^{40}K decays and bioluminescence) at the detector site are generated with a fixed user-configurable rate per OM. Alternatively, the noise rate per OM can be taken from real data. A module providing this functionality was re-written to be compatible with the previous ANTARES implementation.

To be able to compare Monte Carlo events to real data, full simulations of the OM's digitisation electronics are needed. The ANTARES code for these simulations has been encapsulated into modules: The OM simulator uses a parameterised approach to simulate the transit time spread and the amplitude smearing of the PMTs. The simulation of the PMT signal digitisation is fully compatible with the one currently in use by ANTARES. A second simulation for a time-over-threshold readout scheme was developed from scratch. Both simulations will be described in sections 4.10.2 and 4.10.3 respectively.

---

[2] For reasons of pronounciability, it was decided to use the name "SeaTray", despite the fact that "KM3Tray" would be a more correct name, as the "Ice" in IceTray does not refer to the detector's medium but rather to its name.

When using Monte Carlo data, it is necessary to simulate different detector trigger conditions. For this purpose, the complete ANTARES core trigger code was encapsulated into an IceTray module. This module receives the current event data and converts it into the format used internally by the ANTARES trigger. The original trigger code can thus be used unchanged, which allows for easy maintenance and updates in case new trigger algorithms are added to the ANTARES DAQ. After calling the trigger routines, the module converts all results back to a data format compatible with IceTray and passes all information to the next module.

The ANTARES standard reconstruction strategy has also been ported to IceTray from its *reco* implementation mentioned in section 3.1. A full description can be found in section 4.11.1. In addition, two more reconstruction algorithms were ported to IceTray, namely the χ^2-based *BBFit* algorithm [87] and the *scanfit* algorithm [88]. Porting of the latter was not done as part of this work but rather during another PhD thesis [85]. As these algorithms are not suited for KM3NeT in their current state, they have not been used for the studies presented later on.

Modules provided by the IceCube collaboration

Events can not only be produced by the ANTARES Monte Carlo packages, but also by using other event generators like *ANIS* [36] (neutrino events) and *CORSIKA* [89] (atmospheric muons). Both of them are also in use for IceCube and already exist as IceTray modules. Once events have been generated, the resulting particles need to be tracked through the detector volume and their Cherenkov light needs to be simulated. Muons, being the main detection channel of neutrino telescopes, can either be tracked by the *MMC* [90] package which was modularised by IceCube or by a custom tracking code based on Geant4 [91] developed specifically for KM3NeT in the context of this work (see section 4.5).

4 A new KM3NeT simulation and reconstruction chain

```
++++++++++[>+++++++>++
++++++++>+++>+<<<<-]>+
+.>+.+++++++..+++.>++.
<<+++++++++++++++.>.++
+.------.--------.>+.>.
```

(example code)

This chapter presents a new simulation chain that was developed within the frame of this work. It consists of a combination of tools that have already been in use by the IceCube collaboration and new tools developed specifically for KM3NeT.

4.1 Overview and Incentive

The tools that have been used for most of the simulation work for KM3NeT are taken over from the ANTARES pilot project and have been successfully in use there for over a decade.

This fact, however, also leads to problems: until now, no independent toolchain was in existence, which would have been necessary to perform cross-checks of the current tools. Additionally, all ANTARES simulation code is written in FORTRAN in a highly non-modular style and is thus hard to maintain. This is especially true for modern operating systems where FORTRAN compilers do not have as high an importance as they did a few years ago.

It is thus desirable to develop an alternative simulation chain based on more modern programming languages. For this work, such a chain has been implemented on top of the IceTray framework.

4.2 Simulation of neutrino interactions using ANIS

The first step in a simulation chain for a neutrino telescope has to be the generation of neutrino events according to a spectrum defined by the user. Here, an *event* is defined as the combination of the neutrino's energy, its direction, the reaction vertex, the reaction's final state and an event weight. The weight is necessary as typically, all neutrinos are forced to interact within a certain volume around the detector. Their interaction probability and the initial energy spectrum are combined into a weight that has to be applied to each reconstructed event to obtain a physical neutrino event rate.

An existing tool providing exactly these features is *ANIS* [36], originally developed for AMANDA/IceCube. Therefore, a modularised version for IceTray is already available. ANIS can be used to simulate neutrinos of all flavours, though only muon neutrinos will be covered in this document. It includes tabulated cross-sections for neutrinos and anti-neutrinos and is able to simulate both CC and NC events. The νN structure functions are chosen according to CTEQ5 [92] (cf. figure 2.3). Generation of neutrino events starts at the surface of the Earth. From there, they are propagated to the detector along straight lines, neglecting small angle neutrino scattering. The density profile of the earth is chosen according to the Preliminary Earth Model [93]. In case of an interaction on the way to the detector, an appropriate interaction channel is chosen and the neutrino is either absorbed or regenerated. Once a neutrino reaches the pre-defined volume around the detector, it is forced to interact within the volume and its interaction probability is stored. Additionally, the final state of the reaction is generated as a particle vector. As neutrino telescopes cannot distinguish between different types of hadrons, no hadronisation is performed. All hadronic energy is written out as a single particle type reserved especially for this purpose, whereas the leptonic part is fully stored as independent particles. In the case of muon neutrinos this is either a muon for CC reactions or a muon neutrino for NC reactions. For the purposes of event simulation the NC neutrinos can be discarded, as they will not be seen as part of the event.

The most important input parameters to the ANIS simulation are the neutrino spectrum (specified as the spectral index γ of a power law spectrum $E^{-\gamma}$), the neutrino energy range $[E_{\mathrm{min}}, E_{\mathrm{max}}]$, the zenith range and the neutrino flavour. ANIS always simulates neutrinos and anti-neutrinos as well as NC and CC events in a single run. Additionally, the interaction volume size around the detector and the detector depth needs to be specified. The interaction volume is defined as a cylinder, anchored at the detector centre with its axis parallel to the neutrino direction. Its radius and height can be chosen by the user. See figure 4.1 for an illustration.

Almost no modifications were necessary to use ANIS in its modularised form fro KM3NeT. The hard-coded detector medium density and the fixed rock depth of 3000 m which are used for IceCube simulations were made user-configurable. The detector medium density can now be changed from its default value for polar ice to that of sea water. Apart from that, no changes were necessary to be able to use the code for KM3NeT simulations.

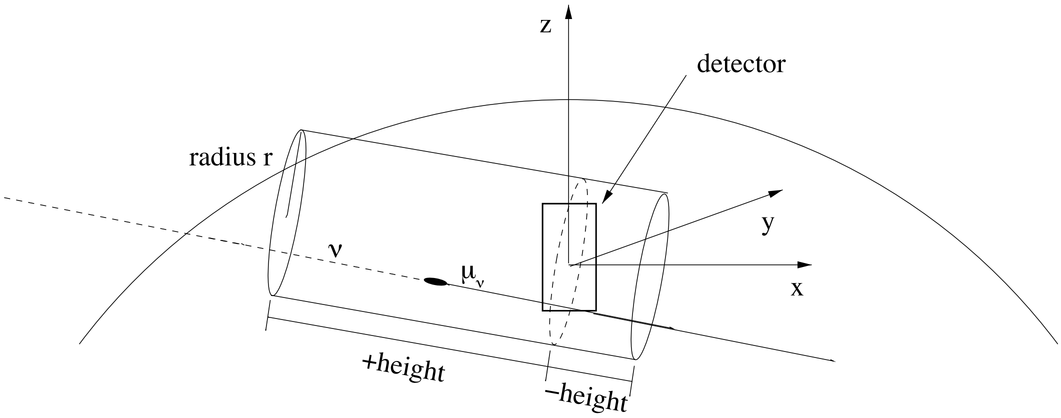

Figure 4.1 The ANIS geometry. The cylinder shown is the final/detection volume defined by two heights (before and after the detector centre) and a radius. This radius defines the generation area. The cylinder is rotated to have its axis in parallel with the neutrino direction. The actual detector volume is shown as a box around the coordinate origin. Taken from [36].

4.2.1 Event weights

ANIS stores event weights with its final events [93]. The most important weight is the interaction probability in the final volume P_{int}, which is being calculated from the cross-section for every event. Together with the knowledge of the input spectrum's spectral index γ and the simulation parameters described previously, an event rate for an arbitrary spectrum

$$\frac{\mathrm{d}\Phi'(E)}{\mathrm{d}E} \tag{4.1}$$

can be calculated. The generation spectrum is defined to be

$$\Phi(E) = (E/\mathrm{GeV})^{-\gamma}\left[\mathrm{GeV}^{-1}\mathrm{cm}^{-2}\mathrm{sr}^{-1}\mathrm{s}^{-1}\right]. \tag{4.2}$$

Neutrinos are sampled uniformly across the generation area A and isotropically in Ω, so that the total rate of incoming neutrinos can be written as

$$R_{\text{incoming}} = \int_{E_{\min}}^{E_{\max}} \Phi(E)\mathrm{d}E \cdot A \cdot \Omega, \tag{4.3}$$

where A is the generation area and Ω is the integrated generation solid angle.

For a sample of N_{gen} generated events, the rate of interacting neutrinos due to the flux $\Phi(E)$ is

$$R_{\text{int}} = \frac{1}{N_{\text{gen}}} \sum_{i=1}^{N_{\text{gen}}} \int_{E_{\min}}^{E_{\max}} \Phi(E) \mathrm{d}E \cdot A \cdot \Omega \cdot P_{\text{int},i} \ . \tag{4.4}$$

Re-weighting event-wise to $\Phi'(E)$ yields

$$\begin{aligned} R'_{\text{int}} &= \frac{1}{N_{\text{gen}}} \sum_{i=1}^{N_{\text{gen}}} \frac{\Phi'(E_i)}{\Phi(E_i)} \int_{E_{\min}}^{E_{\max}} \Phi(E) \mathrm{d}E \cdot A \cdot \Omega \cdot P_{\text{int},i} && (4.5) \\ &= \frac{1}{N_{\text{gen}}} \sum_{i=1}^{N_{\text{gen}}} \frac{\Phi'(E_i)}{E_i^{-\gamma}} \int_{E_{\min}}^{E_{\max}} E^{-\gamma} \mathrm{d}E \cdot A \cdot \Omega \cdot P_{\text{int},i} && (4.6) \\ &= \frac{1}{N_{\text{gen}}} \sum_{i=1}^{N_{\text{gen}}} \Phi'(E_i) \cdot w_i \ , && (4.7) \end{aligned}$$

with w_i being defined as

$$w_i := \frac{1}{E_i^{-\gamma}} \int_{E_{\min}}^{E_{\max}} E^{-\gamma} \mathrm{d}E \cdot A \cdot \Omega \cdot P_{\text{int},i} \ . \tag{4.8}$$

For convenience, this derived weight w_i is stored with every event during the generation step. This weight is practical, as it can be used to weight events without knowing about simulation parameters such as the generated energy range, the energy spectrum, the zenith angle range and the generation volume radius.[1]

4.3 Simulation of atmospheric muons with CORSIKA

In addition to a neutrino flux, the atmospheric muon background has to be simulated. The muons' lateral and energy distributions are generated using the CORSIKA extensive air shower Monte Carlo tool [89] in a version originally modified for AMANDA [94][2].

CORSIKA simulates air showers induced by a cosmic ray flux of protons and nuclei. Muons produced in these showers are stored at the sea surface level. They can then be propagated to the detector as described in section 4.4.

---

[1] The weight w_i was given the name “OneWeight” by the IceCube collaboration.

[2] dCORSIKA is available from `http://icecube.wisc.edu/~jkelley/simulation/dcorsika.html`.

4.4 Propagation of muons to the detection volume

Muons produced near the detector (either by ANIS on the surface of the generation volume or by CORSIKA at the sea level) need to be propagated to the actual detector volume. This is done using the *MMC* simulation code [90][3]. The JAVA-based code has already been wrapped as an IceTray module by IceCube, which makes it easy to use. MMC propagates muons (and optionally tauons) through matter while simulating their energy losses. For the simulation chain presented here, MMC is only used to find the position of the muon on the surface of the sensitive volume of the detector and to calculate the muon's energy at this point. The sensitive volume is defined as an upright cylinder containing the instrumented detector, extended by three light absorption lengths.[4] As muons can propagate over long distances, it is important to calculate their energy losses with good accuracy. As this was one of the design goals of MMC, it was chosen as the primary muon propagator.

4.4.1 Modifications for KM3NeT

MMC allows to define a lower cut-off energy, which is set to the energy at which Cherenkov light ceases to be emitted. The refractive index used to calculate this energy was hard-coded and has been changed from its original value of $n_{\text{ice}} = 1.31$ to $n_{\text{water}} = 1.35$. Additionally, an already existing definition of the element composition of water at the ANTARES site was bug-fixed (see table 4.1 for the actual composition). Together with a new medium definition containing the KM3NeT detector site depths, these were the only changes necessary for adaptation to KM3NeT. Note that the bug concerning the element composition only affects a pre-defined "ANTARES water" medium type and thus has no effects on simulations using other medium types.

4.5 Muon propagation and Cherenkov light generation

Once a muon has reached the detector, it has to be propagated through its sensitive volume. At the same time, secondary particles from the muon need to be tracked and all Cherenkov light needs to be propagated through the detector medium. A simulation code based on *Geant4* [91] was developed for this purpose. The code performs a full tracking simulation of every particle inside the sensitive volume. This includes the simulation of every single Cherenkov photon. This approach takes an immense amount of computing time, but it provides accurate event simulations usable for cross-checks of parameterised simulations.

---

[3] MMC is available from `http://dima.lbl.gov/~dima/work/MUONPR/`.

[4] This is the same definition as used in the ANTARES simulation tools, see section 3.1.

4.5.1 Detailed simulation

Geant4 provides algorithms for simulation of almost all of the “standard” physics processes needed for tracking of muons, electrons and other particles through a medium, among them all muon energy loss processes described in section 2.1.3. Hadronic processes, which can result from either nuclear interactions of the muon or from the primary hadronic cascade, are simulated according to the *QGSC* model. In Geant4, a large set of hadronic models is made available to the users, each one tuned to different energy ranges and applications. The QGSC model is one of the hadronic models recommended by the Geant4 authors for high-energy applications and is valid up to 100 TeV. Electromagnetic processes can be simulated with much higher energies, although care should be taken, as for example the LPM effect is not yet properly implemented in Geant4 for all processes. Geant4 can not only track high-energy cascades and muons, it can also directly simulate Cherenkov photons and propagate them through a medium.

Medium definition

To be able to track particles, all media surrounding the detector have to be defined in terms of their element composition and density. For the current application, the two important media are *sea water* and *rock*. Medium properties have been chosen to be compatible to the ones used in the ANTARES simulation tools: sea water is mainly composed of H_2O with a salinity of 3.84% and a density of $1.039\,\mathrm{g\,cm^{-3}}$. The bedrock layer composition is chosen to be compatible with *standard rock* as defined in [95]. This definition assumes a material with a density of $2.65\,\mathrm{g\,cm^{-3}}$. As the definition uses an average atomic weight ($\langle Z/A\rangle = 0.5$) which is not properly supported by Geant4, the known chemical composition of Gran Sasso rock as defined for example in [96] was used instead.[5] As this step of the simulation is not meant to be used to propagate muons over long distances, this choice should not influence simulation results.[6] Note that only the chemical composition was changed from the original standard rock definition, the density is chosen as defined originally. See table 4.1 for the exact chemical composition used for the simulation.

Simulation of optical photons needs a few more medium specifications like the wavelength dependent refractive indices, absorption lengths and scattering lengths. These specifications were chosen to be compatible with measurements from the ANTARES site. To be able to compare results, all medium descriptions are taken from the *geasim/km3* tools from the ANTARES software chain. Figure 4.2 shows all these water properties.

---

[5] The Geant4 authors specifically warn about using average atomic weights with their code.

[6] Propagation of muons over long distances is done using MMC in the previous simulation step. MMC includes a proper parametrisation of standard rock.

medium	element	fraction of mass
ANTARES sea water	Hydrogen	10.74%
	Oxygen	85.41%
	Chlorine	2.37%
	Sodium	1.32%
	Magnesium	0.15%
bedrock	Oxygen	52%
	Calcium	27%
	Carbon	12%
	Magnesium	9%

Table 4.1 Composition of sea water at the ANTARES site and of *standard rock* as used in the Geant4-based muon propagation and Cherenkov light generation code.

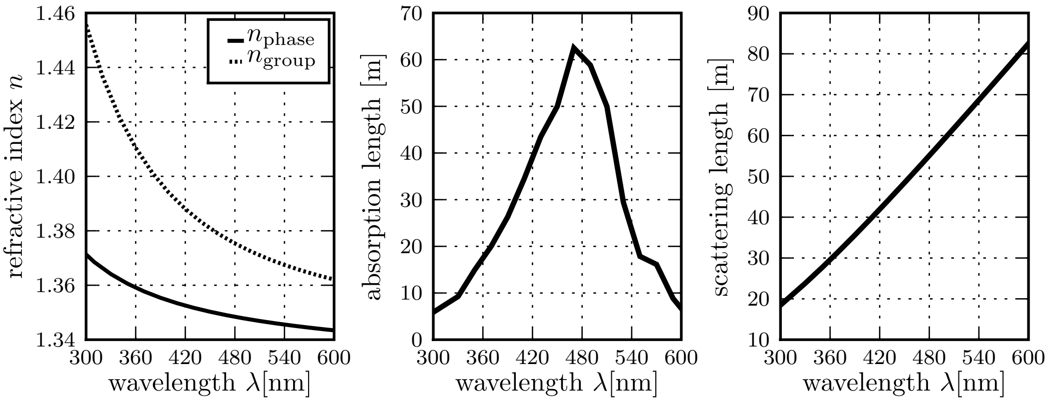

Figure 4.2 Water properties of the ANTARES site used in the simulation. The plots show, from left to right, the refractive index, the absorption length and the scattering length as a function of wavelength. Taken from the *km3* code [74]. The *group refractive index* is calculated as defined in section 2.1.5.

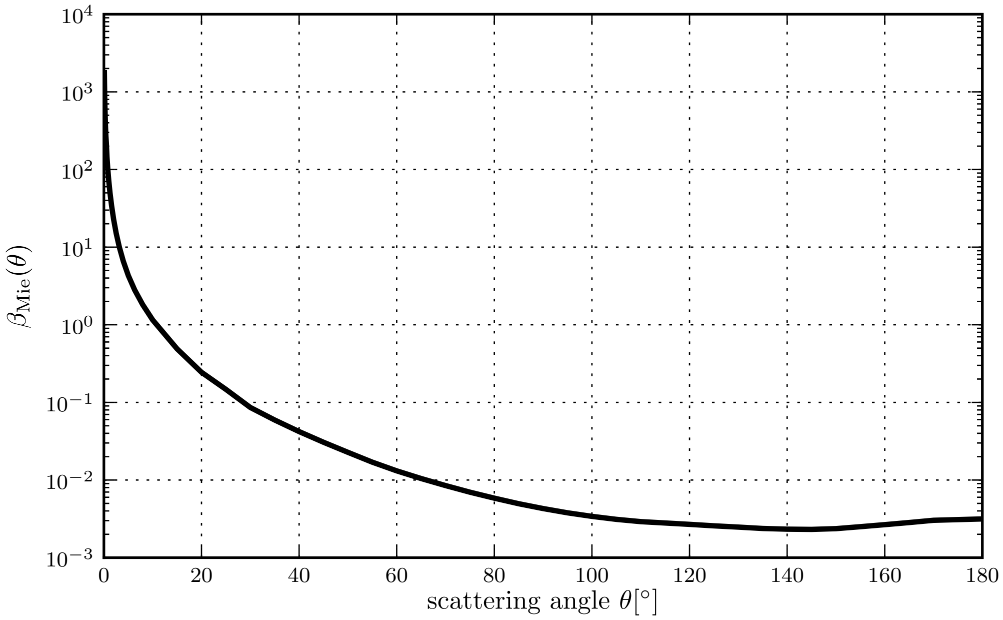

Figure 4.3 Scattering angular distribution $\beta_{\mathrm{Mie}}(\theta)$ for the "partic-0.0075" water model used for water at the ANTARES site.

For light scattering, a scattering angle distribution is needed in addition to the scattering length. The algorithm for calculation of scattering angles was ported from the original FORTRAN implementation in *km3* and implemented as a Geant4 process. This was possible due to the modular design of Geant4 which allows adding new particles and processes as derived classes. There are multiple scattering models implemented in the original ANTARES software. The model currently in use is called "partic-0.0075" and is implemented as a mixture of Rayleigh scattering and scattering on particles (Mie Scattering). For each scattering event, the type of scattering is decided randomly so that the fraction of Rayleigh scattering events is η. All other scattering events will be Mie scatters, described by a scattering angle distribution (or *phase function*) $\beta_{\mathrm{Mie}}(\theta)$. Figure 4.3 shows the angular distributions. The value used for η in the "partic-0.0075" model is 0.17. The Rayleigh scattering angle distribution is described by the parameterisation given by [97] for sea water:

$$\beta_{\mathrm{Rayleigh}}(\theta) = 0.06225\left(1 + 0.853\cos^2(\theta)\right) \tag{4.9}$$

4.5.2 Speedup of the Cherenkov light tracking algorithm for unscattered light

Simulating each single particle generated by an incident muon is a rather time-consuming process. Depending on their energy, single events can take days to simulate on modern CPUs. Even muons with low energies need processing times of at least a few minutes. This is due to the huge number of photons being generated by a single track. In the wavelength range relevant to water Cherenkov telescopes (between 300 nm and 600 nm), approximately $5 \cdot 10^4\,\mathrm{m}^{-1}$ are generated by low muons and their secondary particles. At higher energies, starting at about 1 TeV, this number starts to grow, as the probability of producing larger electromagnetic showers along the muon track increases. Considering muon track lengths of the order of 100 meters or more, a simulation algorithm tracking each photon will always be rather slow.

Most of these simulated photons, however, will never reach an optical module, as a neutrino detector is only sparsely instrumented. In a way, most of the processing time is wasted on the simulation of photons that will never be seen. An easy solution to this problem can be found if optical scattering of photons is neglected. In this case, the simulation code can decide if a photon will never reach an optical module by purely geometric calculations before even starting the tracking code. Whole segments of a muon track can be skipped in the simulation, as unscattered light from these segments would never reach any optical module. Note that, in a Monte Carlo tracking simulation, this is only possible when light scattering is neglected, because the code cannot know if a photon that would not reach an OM on its direct path could eventually reach it after one or more scatters.

The speedup provided by this solution is substantial, but neglecting scattering can distort results, especially for detector designs where the string distance is larger than the scattering length.

4.6 Fast cascade light generation and propagation

As the source of most of the Cherenkov light are cascades (either induced by the muon or by the neutrino itself), a starting point for improvement of simulation times can be to parameterise the light output of electromagnetic or hadronic cascades and optionally include light scattering in this parameterisation.

4.6.1 Angular light distribution

Parameterisations of the angular light output of showers (which are assumed to be point-like for this argument) have been used in previous simulation codes [98, 99]. These parameterisations make use of the fact that the basic shape of the angular

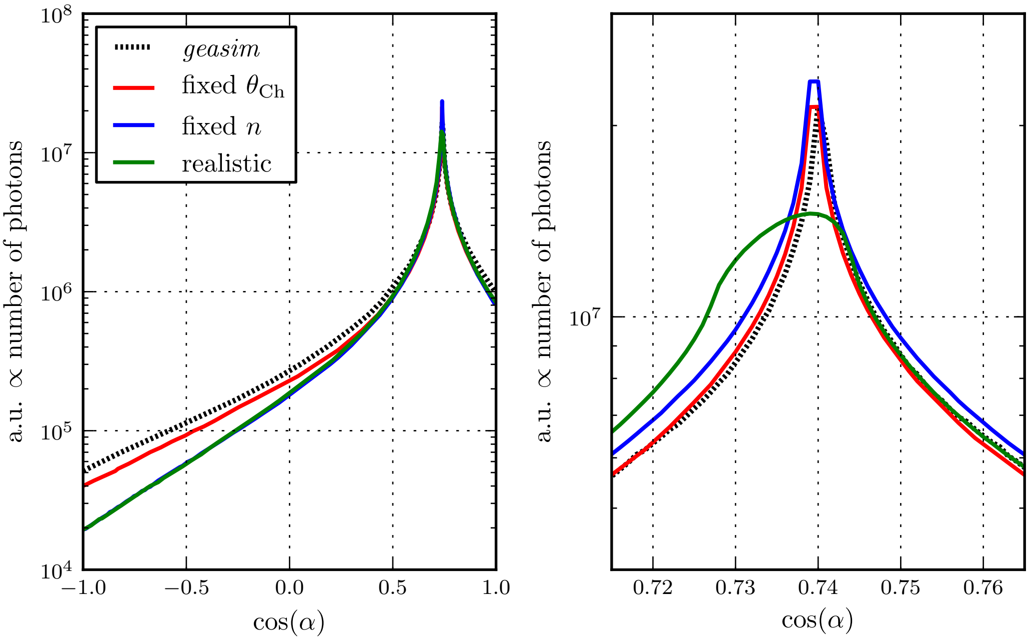

Figure 4.4 The angular light distribution of an electromagnetic cascade with an energy of 100 GeV. The plots show the distribution for a full Geant4 simulation ("realistic"), for a Geant4 simulation with fixed refractive index n but variable $\beta = {}^{v}\!/_{c}$ and for a Geant4 simulation with fixed Cherenkov angle θ_{Ch}, i.e. fixed n and fixed $\beta = {}^{v}\!/_{c}$. The corresponding distribution used for simulations with the Geant3-based *geasim* tool is shown for comparison. The left plot shows the full angular range, whereas the right plot shows a zoomed in portion of the plot around the Cherenkov peak.

light distribution is the same over a large range of primary shower particle energies. Figure 4.4 shows the angular distribution used in the *geasim* package compared to the distribution for showers simulated with Geant4 in the ANTARES sea-water defined previously in section 4.5. During the simulation process, each generated optical photon was killed (i.e. its simulation process was aborted and the particle was removed from the simulation stack). Before removing a photon, the angle between the shower axis and its direction vector was recorded in a histogram. The results can be seen in figure 4.4.

As expected from previous work, the distribution peaks at the Cherenkov angle of about 42°. At angles far away from the peak, these new distributions differ from the distributions used by the original ANTARES software. This is due to the fact that previous implementations used a fixed Cherenkov angle for all particle energies, i.e. they assumed that ${}^{\beta}\!/_{c} \approx 1$ and $n = \mathrm{const}$. When changing this behaviour in

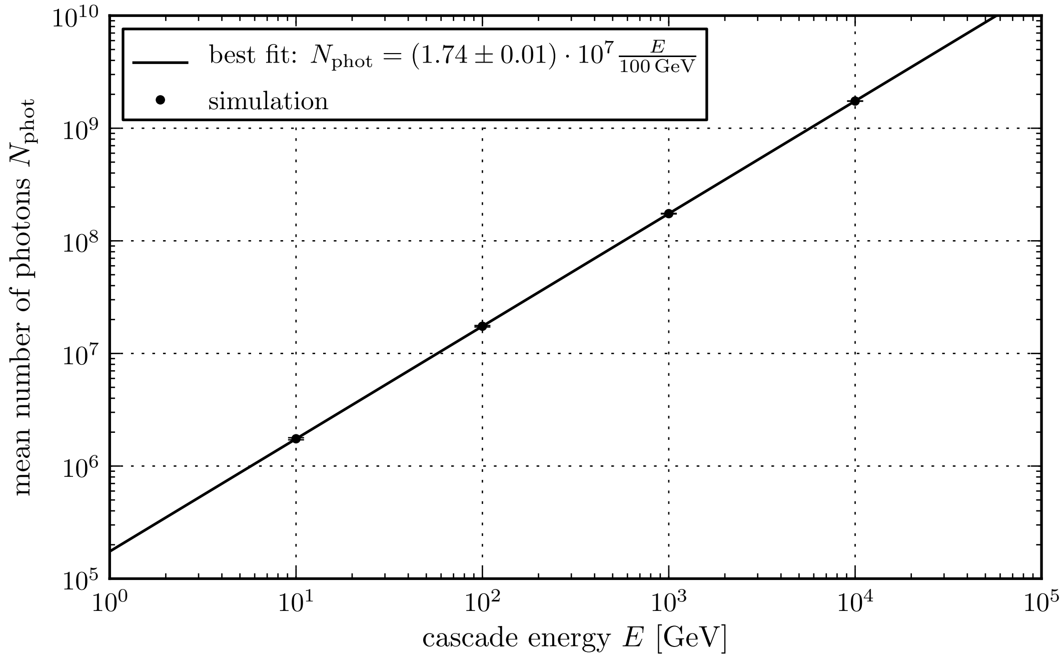

Figure 4.5 The total number of photons produced by cascades of a specific energy in the wavelength range [290 nm, 610 nm] as simulated with Geant4.

the Geant4 simulation code, the original distributions are reproduced more closely. The peak itself has a certain width in the new simulation. This is caused by the use of a realistic refractive index distribution instead of the approximation of using a constant refractive index.

4.6.2 Total photon yield

Figure 4.5 shows the total number of photons generated by a cascade with respect to its primary particle's energy. The dependence on energy is linear over the considered range. A best fit over a range of energies from 1 GeV to 100 TeV yields

$$N_{\mathrm{photons}} \approx 1.74 \cdot 10^7 \cdot \frac{E_{\mathrm{shower}}}{100\,\mathrm{GeV}}. \tag{4.10}$$

4.6.3 Scattering table generation

The most time-consuming process of the simulation chain is the propagation of photons through the detector medium including the simulation of scattering and absorption of photons. This process can be sped up by sampling a multi-dimensional probability distribution that describes the probability to see a photon at a certain position with a certain direction and wavelength together with the photon's travel time. As there is no good analytical model for this distribution, it is usually calculated using Monte-Carlo methods and stored in large lookup tables. The *km3* and *photonics* simulation packages [99] use this method.

For this work, however, a different method is used: the space around a shower is divided into spherical segments. A number of photons is propagated from the shower and tracked through the medium using a full Monte Carlo simulation. If a photon enters a segment it is recorded at the position where it crosses the surface with its full properties, including position, direction and energy. All photon records are stored in a database (the "scattering table") where they can be accessed later on during the actual simulation of a shower. In this way, given that the segment sizes are chosen small enough, photons do not need to be propagated all the way from the shower to the optical module. They can rather be randomly chosen from tables of pre-propagated photons at the nearest segment surfaces.

Figure 4.6 shows the segmentation of the medium around a shower as it is used in the actual implementation: the medium is divided into concentrical sphere shells around a shower. Each shell has two photons tables associated with it that are stored in the photon database: one for the inner boundary and one for the outer one. As the whole space around a shower needs to be covered, each shell (except the innermost and outermost one) shares its boundaries with exactly two other spheres. However, the two tables associated with a shared boundary are still distinct: one contains photons entering a shell from the space outside its maximum radius, the other contains photons entering a shell from inside its minimal radius.

To exploit as many symmetries as possible, the shower is assumed to be point-like, i.e. photons are only emitted from a single point in space which is chosen to be at the origin during the simulation process. Additionally, showers are assumed to have a rotational symmetry around their axis. In the following description, this shower axis is arbitrarily defined to be the z-axis. During the table generation process, it is sufficient to emit photons only with directions in the x-z-plane, provided that an arbitrary rotation around the z-axis is performed whenever such a photon is used later on.

However, even when only photons emitted in the x-z-plane are used, the number of photons that need to be pre-propagated to be able to fully describe only a single cascade is still too large to be effectively handled by a current computer. To further minimise the number of photons that need to be stored, photons are only pre-propagated in the range $\theta_i = 0°..\alpha$, where θ_i is the angle between a photon's direction and the z-axis and α is a sufficiently small constant angle (see figure 4.6(b)). For the implementation used in this work, α was chosen to be $1°$. When using this optimisation, the cascade's angular emission probability is not used during table

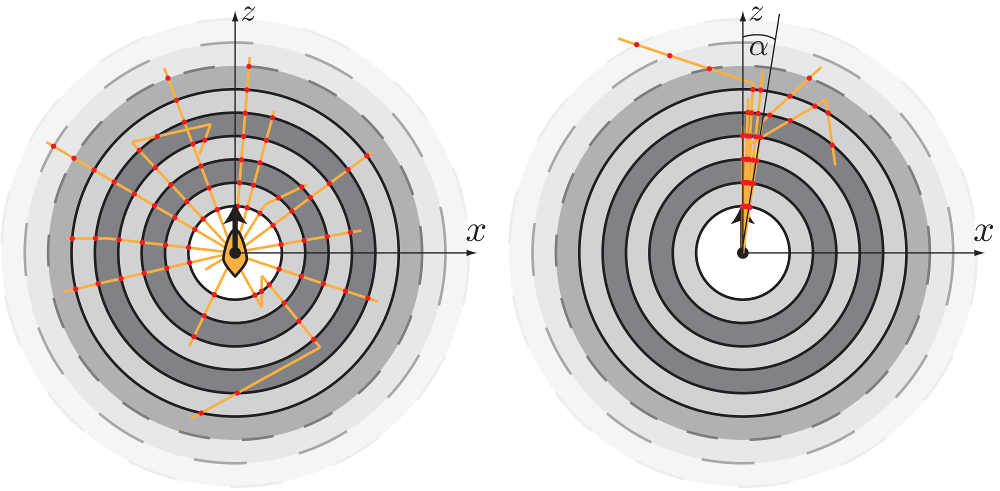

(a) basic principle (b) optimised photon direction range

Figure 4.6 Segmentation of the medium around a shower when building a photon table. The space around a shower is divided into spherical shells. The shower shown in the centre is assumed to be point-like; the extended shower profile is only shown for illustration purposes. Photons (yellow lines) are emitted from the shower. Each time a photon crosses a sphere boundary (red dots), its full properties are recorded in a database. The basic principle is illustrated in (a), whereas (b) shows the optimised photon direction range actually used during the table generation process. Note that photons are only generated in the x-z-plane. They can, however, leave this plane after they are scattered.

generation but rather during the actual simulation process described in the next section. For each photon, θ_i is chosen from a flat distribution.

For each simulated photon, the following data are saved in the scattering table:

1. θ_{sphere}, the zenith angle with respect to the shower axis of the point where the photon track intersects the sphere boundary
2. θ_{dir}, the zenith angle of the photon's direction vector at the sphere
3. φ_{dir}, the azimuth angle of the photon's direction vector at the sphere
4. λ, the photon's wavelength
5. t, the time it takes the photon to travel from its emission to the sphere

6. N_{scat}, the number of scatters the photon has undergone on its way to the sphere (This value is not needed for the actual simulation process and is stored for informational reasons only.)

Note that the azimuth angle of the photon's intersection point with the sphere boundary is not stored in the table. This is because scattering is assumed to have a rotational symmetry around the photon's direction. The azimuthal position can therefore be generated during the simulation phase by adding a random rotation around the photon's initial direction. As photons are only generated with directions near the z-axis, the rotation can be performed around that axis instead. This yields an approximate result without having to store the actual initial direction of each photon.

4.6.4 Light generation at optical modules

With a table of pre-propagated photons as described in the previous section, the algorithm to generate light at a optical module can be split into two parts. First, a list of photons corresponding to a shower is generated at the segment boundaries surrounding the optical module. Then each of these photons is propagated within the segment until it reaches the optical module or it leaves the segment.

Generation of photons at the segment boundaries

Generation of photons at segment boundaries is done by randomly choosing photons from the pre-generated table. If an optical module is fully contained within a segment, photons only have to be chosen from the tables describing the inner and outer shell of this segment. In case an optical module overlaps more than one segment, the photon tables from different segments have to be combined.

As the tabulated photons are only generated with zenith angles in the range $\theta_i \in [0°; \alpha[$ (see section 4.6.3), this process needs to be repeated $R_\alpha = \frac{180°}{\alpha}$ times for each shower. For each iteration $j \in [0; R_\alpha[$, the selected photons are rotated by an angle $j \cdot \alpha$ around the y-axis.[7] For each iteration j, the simulated zenith angle range is therefore $[j\alpha; (j+1)\,\alpha[$. The number of photons to be simulated $N_{\mathrm{sim};j}$ is determined by integrating the angular photon distribution in the current range.

$$N_{\mathrm{sim};j} = \frac{N_{\mathrm{arriving}}}{N_{\mathrm{generated}}} \int_{j\alpha}^{(j+1)\alpha} d_{\mathrm{phot}}(\theta)\mathrm{d}\theta \tag{4.11}$$

Here, $N_{\mathrm{generated}}$ is the total number of photons used for the table generation and N_{arriving} is the number of generated photons actually arriving at the segment bound-

---

[7] To be able to cover the whole zenith range up to 180°, α needs to be chosen so that $R_\alpha \in \mathbb{N}$.

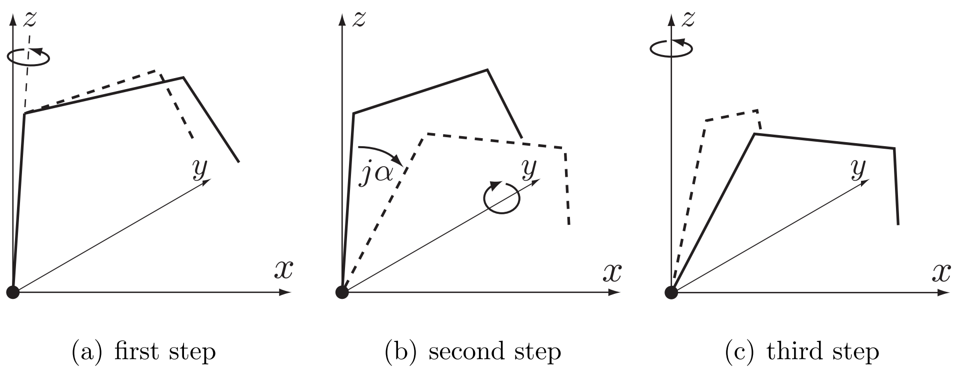

(a) first step (b) second step (c) third step

Figure 4.7 Rotations applied to each photon read from the photon database during the simulation phase. Solid lines represent the geometry before the rotation, dashed lines indicate the position after the rotation. In the actual implementation, the first rotation is not applied around the initial photon direction but around the z-axis. This optimisation can be used because the initial photon directions are always near the z-axis.

ary. The angular photon distribution d_{phot} is normalised to the total photon yield of the shower as described in section 4.6.2.

Now, $N_{\text{sim};j}$ photons are chosen randomly from the pre-generated table. For each photon i, three rotations are performed: (see figure 4.7 for an illustration)

1. A random rotation around the z-axis (the shower axis) to account for the missing scattering azimuth angle. As photons are only produced with directions near the z-axis, this is approximately correct. The rotation angle is chosen randomly from the range $[0°; 180°[$.

2. A rotation around the y-axis to account for the currently simulated zenith angle. The rotation angle is $j\alpha$.

3. Another random rotation around the z-axis to account for the fact that photons were only emitted in the x-z-plane. Again, the rotation angle is chosen randomly from the range $[0°; 180°[$.

At this point, a photon is fully propagated to the boundary of a segment and is ready to be propagated to an OM. Similar to the *km3* simulation code, the maximum segment distance was set to 250 m for the results presented in this work. However, this value is a configurable option and thus can easily be changed.

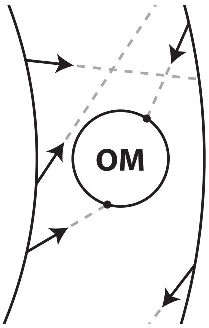

Figure 4.8 Propagation of photons from a segment boundary to an OM. Photons stored at segment boundaries are indicated as black arrows, their propagation tracks are shown as dashed lines. Once a photon hits the OM sphere, it is stored for further processing, indicated as a small black dot on the OM surface.

Propagation of photons inside a segment

To save computation time, scattering is neglected at this point. Scattered photons are treated as if they were absorbed, so in fact the scattering and absorption lengths are combined into an attenuation length λ_{att} with

$$\lambda_{\text{att}} := \left(\lambda_{\text{abs}}^{-1} + \lambda_{\text{scat}}^{-1}\right)^{-1} \tag{4.12}$$

This length is used to describe the mean length after which a photon cannot be observed by an optical module. This is of course an approximation, but if segment sizes are kept small enough, absorption and scattering should be sufficiently rare.

As photons can only travel in straight paths at this point, they can be described by line segments with a starting point $\vec{a}_i$ and a length l_i. The starting point is already known from the previous step. The length l_i is sampled from an exponential distribution with the attenuation length as its mean. In case the line described by these quantities leaves the segment, it is clipped to stay inside by shortening l_i. This simply means that all photons that leave the segment without hitting an OM are immediately removed from the simulation.

In this way, finding the list of photons that hit a spherical OM becomes equivalent to the problem of finding intersections of line segments $\{(\vec{a}_i, l_i)\}$ with a sphere, which is computationally cheaper than a full scattering simulation. See figure 4.8 for an illustration of the tracking process from the segment boundary to an OM.

The output of this simulation step is a list of photons that hit the OM sphere, which can then be converted into actual hits.

4.6.5 Optimisation for unscattered photons

This section describes a further optimisation technique that can be used to store more photons in a single table while keeping its size manageable. This increases the statistics available for simulation.

In the algorithm described until now, direct (i.e. unscattered) photons are treated in the same way as photons that have undergone one or more scattering events. Direct photons, however, do not necessarily need to be stored in the table one by one as their position and direction on each sphere are known a priori. The only information missing is the wavelength-dependent survival probability on each segment boundary. Using this fact, the table generation algorithm can be changed to prevent all direct photons from being stored. Instead, an entry to a wavelength histogram is added for each photon intersecting the sphere boundary that has not yet been absorbed or scattered. This histogram is then stored along with the database of scattered photons.

During the simulation step, direct photons on the segment boundaries now have to be generated separately. This is done by sampling the histogram, which leads to a correct distribution of photon wavelengths for the corresponding distance from the shower. The photon directions and positions are chosen according to the shower's angular profile. Because the segments were chosen to be spherical, the photon position vectors are always parallel to their direction vectors. Once all direct photons have been generated at the sphere boundaries, the algorithm can continue to track them to an OM in the same way as described in the previous section.

4.6.6 Longitudinal light distribution

In the simulation process described up to now, showers were treated as point-like light sources. Using the assumption that the angular light distribution is approximately independent from the shower energy, a shower's longitudinal light distribution can be approximated by distributing its total light output to a number of sub-showers. These sub-showers are then placed along the shower axis according to the longitudinal shower profile.

Figure 4.9 shows such a longitudinal shower profile for a cascade induced by an electron with an energy of 100 GeV. It also shows a best fit using a gamma distribution

$$p(x,a,b) := x^{a-1}\frac{e^{-x/b}}{b^{a}\Gamma(a)}. \tag{4.13}$$

Because the profile changes with energy, this fit has been performed for different energies. The fit parameters are shown in figure 4.10. It can be seen that the *scale* parameter b is approximately constant, whereas the *shape* parameter a varies linearly

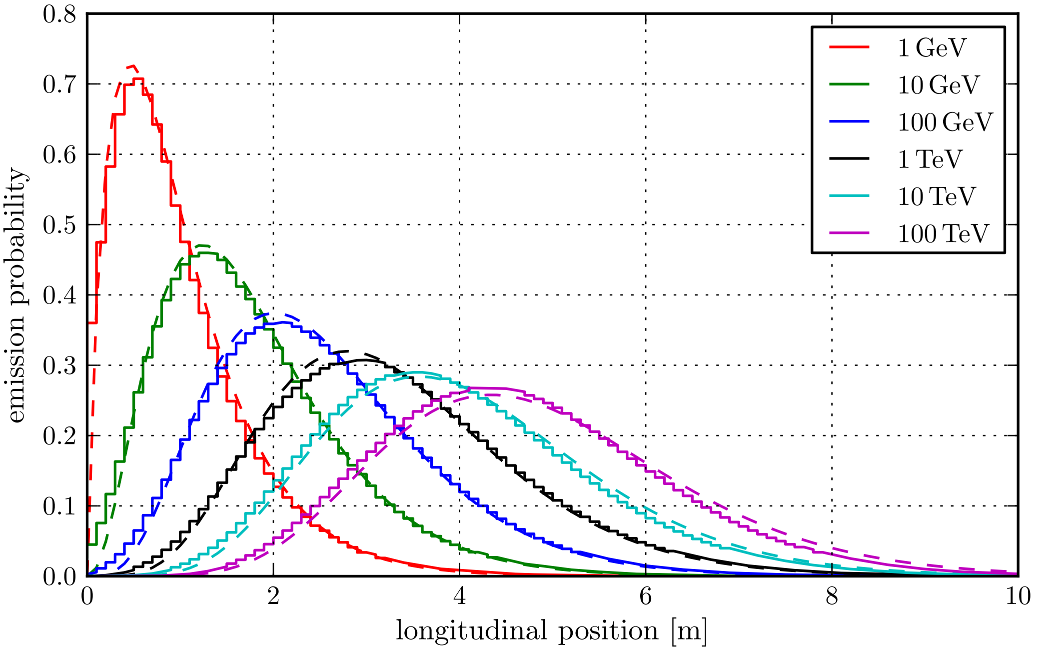

Figure 4.9 Longitudinal light distribution for cascades with different energies. The parameterisation given in (4.13) is overlaid using the parameters from (4.14).

with $\log E$. Thus, the following parameterisation has been found:

$$a = 1.85 + 0.62 \cdot \ln \frac{E}{1\,\mathrm{GeV}} \tag{4.14}$$

$$b = 0.54 \tag{4.15}$$

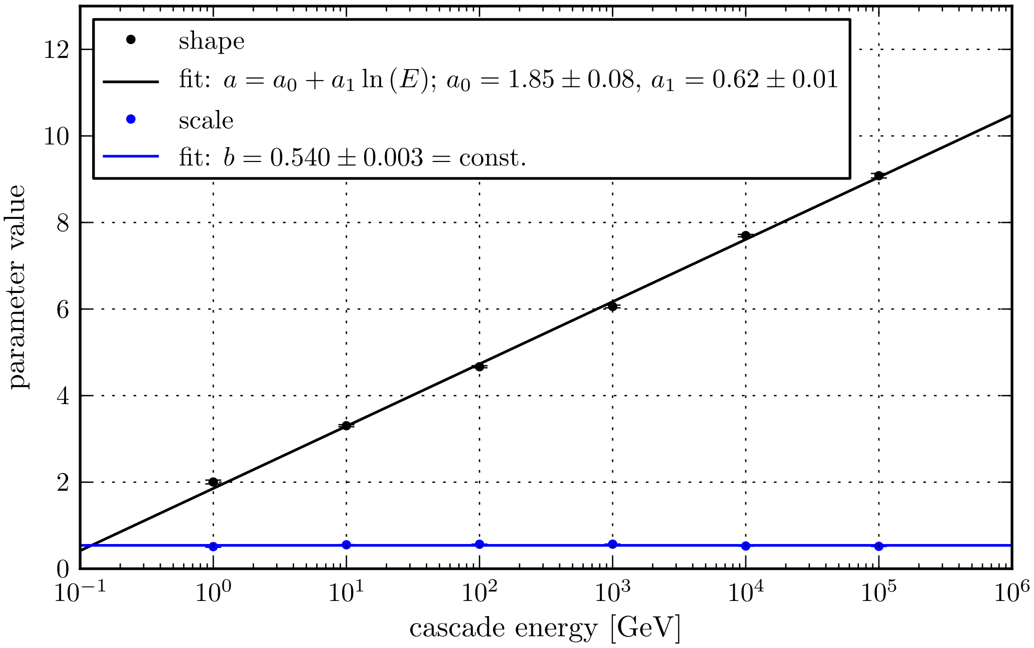

Figure 4.10 Fits of the shape and scale parameters a and b from the longitudinal cascade shape parameterisation (4.13).

4.7 Adaptation of the cascade simulation approach to muons

The method for shower photon simulation described in the previous section can only be used for point-like light sources as it relies on the spherical symmetry of the source.

However, the basic idea of using a database of pre-propagated photons for fast lookup can be extended to muons (or any other track-like light source), too. This section describes a spatial segmentation that can be used for this problem.

To be able to exploit as many symmetries as possible, the following assumptions are made:

- During database generation, muon tracks are assumed to have infinite length. An extension to the algorithm that allows simulation of muons with finite length will be presented in section 4.7.3.
- Muons travel with a constant speed of c.
- Muons are simulated as “bare” muons, i.e. any secondary particle created by the muon that has an energy above a certain threshold E_{thresh} is not regarded

as part of the muon. During the database creation phase, these particles are removed from the simulation immediately, whereas during the simulation phase, they are treated as separate showers distinct from the muon. Such showers are then simulated independently from the muon in a second step, using the algorithm described in section 4.6.

- The mean light output of a muon during its traversal through the detector is assumed to be constant. Energy losses are not taken into account for purposes of light generation.
- Rotational symmetry is assumed around the muon track.

The coordinate system for this algorithm is chosen so that the z-axis is parallel to the direction of the muon. Because of the rotational symmetry of the problem, the x- and y-axes can be chosen arbitrarily as long as they are orthogonal to the z-axis and to each other.

4.7.1 Spatial segmentation

Using these assumptions, a muon track does not only have a rotational symmetry around its axis, it also has a translational symmetry along the axis, as long as the photon arrival times are adjusted accordingly. A photon seen in the x-y-plane at time t is equivalent to a photon recorded in any other plane parallel to the x-y-plane as long as the photon time is corrected to be $t' := t + \Delta t$ with

$$\Delta t := \frac{\Delta z}{c}, \tag{4.16}$$

where Δz is the distance of the shifted plane from the original x-y-plane. See figure 4.11(a) for an illustration. It is therefore sufficient to record photons only in (or near) the x-y-plane. Due to the rotational symmetry, segments only have to be stored around an arbitrary axis in this plane.

For these reasons, segments are chosen to be “tube segments”, each with a certain inner radius R_{inner}, an outer radius R_{outer}, a height h and an angular (azimuth) range $\Delta\varphi$ (see figure 4.11(c)).

4.7.2 Table generation

Photon tables are generated by propagating a muon from a position on the z-axis that is sufficiently far away from the origin to look like an infinite muon. The current implementation uses a distance of $d = 600\,\text{m}$. The muon is propagated along the z-axis until it has traveled a distance of $l = 2d$. In case a secondary particle produced by it has an energy higher than a certain threshold E_{thresh}, it is immediately removed

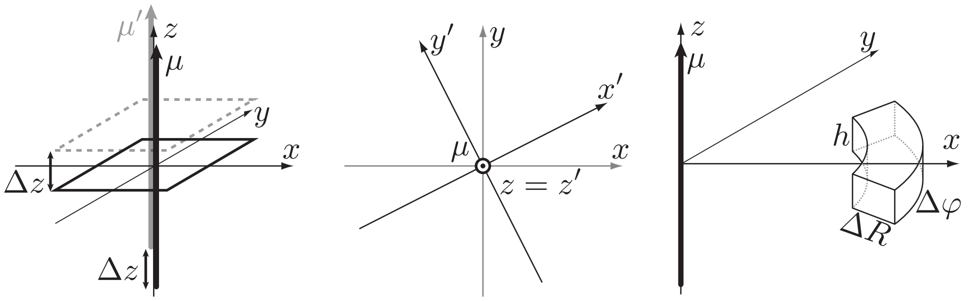

(a) translational symmetry (b) rotational symmetry (c) a tube segment

Figure 4.11 Rotational and translation symmetry of a muon track and a possible spatial segmentation using "tube segments", i.e. cylindrical segments with a certain radial width ΔR, a height h and an angular range $\Delta\varphi$.

from the simulation and does thus not produce any light. The threshold energy is set to $E_{\text{thresh}} = 500\,\text{MeV}$ in the current implementation.

The tube segments are placed along the x-axis with a radial length of $R_{\text{outer}} - R_{\text{inner}} = 1\,\text{m}$; the segment height is $h = 1\,\text{m}$. For each radial segment, its azimuthal range is chosen so that an OM sphere with a diameter of $2r_{\text{OM}} := 1\,\text{m}$ fully fits inside the segment, i.e. $\Delta\varphi := \text{atan}(\frac{2r_{\text{OM}}}{R_{\text{inner}}})$.

All photons produced by the muon or its secondaries below E_{thresh} are propagated through the medium using Geant4. In case a photon crosses a segment boundary, it is recorded and stored in the photon table for this segment. Each photon record stores the particle's position, direction, wavelength and its emission time from the muon. As the muon is assumed to travel with constant speed c, a photon's emission time can easily be converted into the position along the muon track where it was emitted.

The data from all tables is saved to an on-disk database after the muon has travelled for the pre-defined length $l = 2d$. To increase photon statistics, this procedure is performed with a number of muons. The tables for these muons are then merged into a single table which is eventually used for simulation. Table merging is done by concatenating all photon records from multiple muons belonging to the same radial segment bin. In case a table exceeds a certain amount of entries, photon records are randomly deleted from the table. The mean number of photons N_{phot} recorded per muon is stored along with each table, which allows to select the right number of photons during the actual simulation process.

4.7.3 Light generation at optical modules

Before generating photons at an OM for a certain muon, the reference frame is rotated and translated so that the muon's direction is parallel to the z-axis and its initial position is on this axis. A time offset for the muon is calculated so that the OM's centre lies on the x-y-plane. This offset is later added to the arrival times of all photons hitting the OM. The simulation then starts within this new reference frame which is compatible to the frame in which the photon database was generated.

Generation of hits at optical modules is then performed in the same way as for showers: photons are randomly selected on the boundaries of the segments surrounding an OM. All these photons are then propagated inside their segments until they either leave the segment or hit a sphere around the OM. All photons intersecting the sphere are then returned from the simulation and can be used to generate hit signatures for this OM. This approach is analogous to that used for showers described in section 4.6.4. It differs from it in that no random rotations of photon positions and directions are needed during the simulation stage. This is because the segments are much smaller than the ones used for the shower tables. In this way, most of the photons that are generated on a segment boundary actually hit the OM sphere. This helps keeping the photon database much smaller.

The photons generated up to now are compatible with the assumption of a muon track with infinite length. As each photon also has information about the time at which it was emitted from the muon, all photons hitting the OM sphere that were emitted before or after the muon really existed can easily be omitted during the generation process. In this way muon tracks with finite lengths can be simulated easily.

4.8 A unified cascade/muon simulation

The method of using photon databases with the "tube segments" spatial segmentation as presented in the previous section (4.7) can also be adapted to be used for simulation of cascades. This section describes this adapted method which can be used as an alternative to the algorithm presented in section 4.6.4.

The basic idea is to use the exact same spatial segmentation as for muons.[8] Showers are again regarded as point-like objects during the table generation and initial simulation process. The algorithm presented in section 4.6.6 is then used to construct cascades with a longitudinal extent.

In contrast to a muon track where photons are emitted during the whole lifetime of the particle, shower photons are all emitted at approximately the same point in

---

[8] For cascades with their spherical symmetry, sphere segments instead of tube segments would have been the more logical choice. By using tube segments, however, the most of the algorithms developed for muons could be re-used.

time. It is therefore not necessary to store the emission time for shower photons. As a good approximation, their emission time can be set to the interaction time of the shower's primary particle. Cascades also do not have a translational symmetry along their axis, however, they can be assumed to be point-like objects. The latter property can be used to generate photon tables in almost the same way as for muons by placing the shower in the reference frame's origin. In order not to be dependent on the shower's direction, light is generated isotropically from this point. For each photon, the initial direction vector is stored along with all of its other properties. This allows to weight photons later during the simulation phase according to the shower's angular profile and its direction. All other aspects of the database creation process are kept exactly the same as already described for muons.

During the simulation phase, the reference frame is rotated so that the shower to be simulated is in the frame's origin and the detecting OM is on the x-axis and thus enclosed in one or more segments.

4.9 Simulation of light near and in optical modules

Once light has been propagated to each optical module, the module's response must be simulated. This includes all effects of the glass housing and of the actual PMT. In this step, photons are propagated through the OM until they are either absorbed or hit the PMT's photocathode. For technical reasons, this step also includes the conversion of photons into photoelectrons (p.e.'s) at the photocathode and propagation to the first dynode, which is described by the so-called "collection efficiency". Everything else, including the propagation of photoelectrons through the PMT is done in a separate step described in the next section (section 4.10).

This section first describes the simulation of the ANTARES-style optical module with a single PMT per module. This is the design already used by all existing neutrino telescopes like ANTARES, IceCube and Baikal. The second part covers an alternative design where each OM houses multiple small PMTs, called the "multiPMT" design.

4.9.1 ANTARES-style modules

The essential part of this simulation step is to determine if a photon arriving on an OM is converted into a photoelectron at the PMT's photocathode. There are several factors determining the probability of measuring a photon:

- The photon must not be absorbed in the OM's glass sphere. This is described by a wavelength-dependent transmission probability $p_{\text{glass}}(\lambda)$, where λ is the photon's wavelength.

- The photon must not be absorbed in the optical gel connecting the OM glass to the PMT. This can again be described by a transmission probability $p_{\mathrm{gel}}(\lambda)$.
- The photon must arrive at the photocathode to be detected. This is described by a geometrical factor p_{geom} corresponding to the ratio of OM area and the PMT area, both projected on a plane which is perpendicular to the PMT direction d_{PMT} (i.e. the axis of rotational symmetry of the PMT).

  $$p_{\mathrm{geom}} = \frac{A_{\mathrm{OM,proj.}}}{A_{\mathrm{PMT,proj.}}} = \frac{\pi R_{\mathrm{OM}}^2}{\pi R_{\mathrm{PMT}}^2} = \frac{R_{\mathrm{OM}}^2}{R_{\mathrm{PMT}}^2} \tag{4.17}$$

  The factor p_{geom} describes the ratio of the area projections for photons incident anti-parallel to the PMT direction, i.e. for photons with $\alpha = 0$, where $\alpha = -\mathrm{acos}(\vec{d}_{\mathrm{phot}} \cdot \vec{d}_{\mathrm{PMT}})$. For photons from all other directions, the lowered acceptance can be described by including an angular acceptance factor $p_{\mathrm{ang}}(\alpha)$ with $p_{\mathrm{ang}}(0) = 1$.[9]
- The photon must be converted into a photoelectron at the photocathode. This is described by the PMT's quantum efficiency $p_{\mathrm{qe}}(\lambda)$.
- The photoelectron must arrive at the PMT's first dynode. This probability is described by the "collection efficiency" p_{coll}. In the current implementation this factor does neither depend on α nor on λ.

Combining all these probabilities yields an overall detection probability for the conversion of an incident photon into a hit that is measured by a PMT:

$$p_{\mathrm{detect}}(\lambda, \alpha) := p_{\mathrm{glass}}(\lambda) \cdot p_{\mathrm{gel}}(\lambda) \cdot p_{\mathrm{geom}} \cdot p_{\mathrm{ang}}(\alpha) \cdot p_{\mathrm{qe}}(\lambda) \cdot p_{\mathrm{coll}} \tag{4.18}$$

Note that for each OM, the glass and gel transmission probabilities are not stored directly, but are rather split into an absorption length $l_{\mathrm{glass/gel}}(\lambda)$ and a glass/gel thickness $d_{\mathrm{glass/gel}}$. The respective transmission probabilities can then be calculated as

$$p_{\mathrm{glass/gel}}(\lambda) = e^{-d_{\mathrm{glass/gel}} \cdot l_{\mathrm{glass/gel}}(\lambda)}. \tag{4.19}$$

Splitting this value into a material property and a geometrical factor allows for greater flexibility when different OM designs are studied. Figure 4.12 shows the individual transmission probabilities and the quantum efficiency for the standard ANTARES OMs used for all single-PMT simulations in this work. Note that the

---

[9] The reason for defining the angular acceptance like this is to stay compatible with previous ANTARES code which uses the same definition. Note that for a flat photocathode the angular acceptance becomes $p_{\mathrm{ang}}(\alpha) = \cos(\alpha)$ if scattering and reflection processes in the OM are neglected.

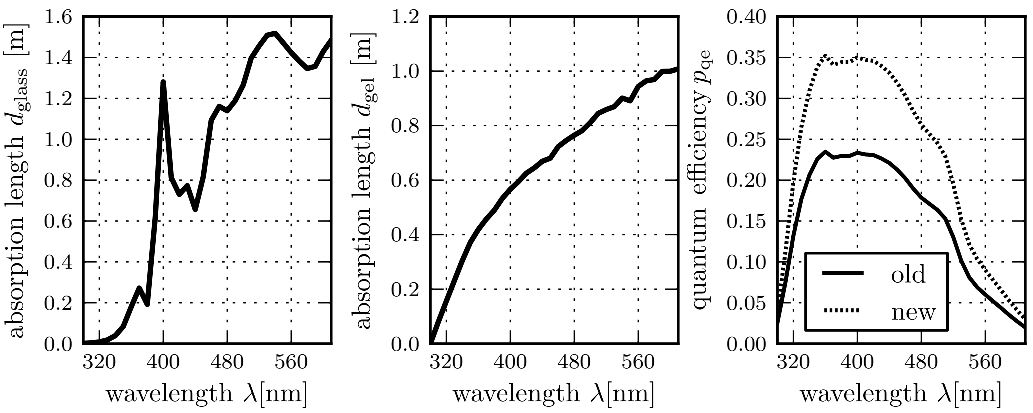

Figure 4.12 Various properties of an ANTARES-style optical module with a single PMT. The PMTs used in all simulations in this work (labelled "new") have a higher quantum efficiency than the ones used in the existing ANTARES design (labelled "old"). The new quantum efficiency is scaled up from the ANTARES values to have a peak value of 35%. The original values have been extracted from the ANTARES simulation tools *km3* and *geasim*.

quantum efficiency has been scaled from the original ANTARES values to have a peak value of 35%. This was done to be comparable with newer PMT photocathode coatings the have become available since ANTARES was designed. The PMT's angular acceptance is shown in figure 4.13. All other properties are summarised in table 4.2.

Having defined the overall detection probability $p_{\mathrm{detect}}(\lambda, \alpha)$, the photon-to-hit conversion process is reduced to sampling a random value u_1 from an uniform distribution in the interval $[1, 0[$ for each photon. A photon is rejected if $p_{\mathrm{detect}}(\lambda, \alpha) \leq u_1$, otherwise it is converted into a hit and passed to the PMT and readout simulation algorithm.

4.9.2 MultiPMT modules

Simulation of multiPMT OMs is done in much the same way as for ANTARES-style OMs. However, as the angular acceptance cannot be parameterised for the whole OM, photons first need to be tracked to determine if they hit a PMT and if yes, which one of the set. This is accomplished with a simple ray-tracing approach. Photons are first tracked through the glass and gel layers neglecting the respective transmission probabilities. PMTs are assumed to be discs with pre-defined radii in a user-definable spatial configuration. In case the photon track does not intersect any PMT disc, it is discarded. In case a PMT is hit, the algorithm described for single-

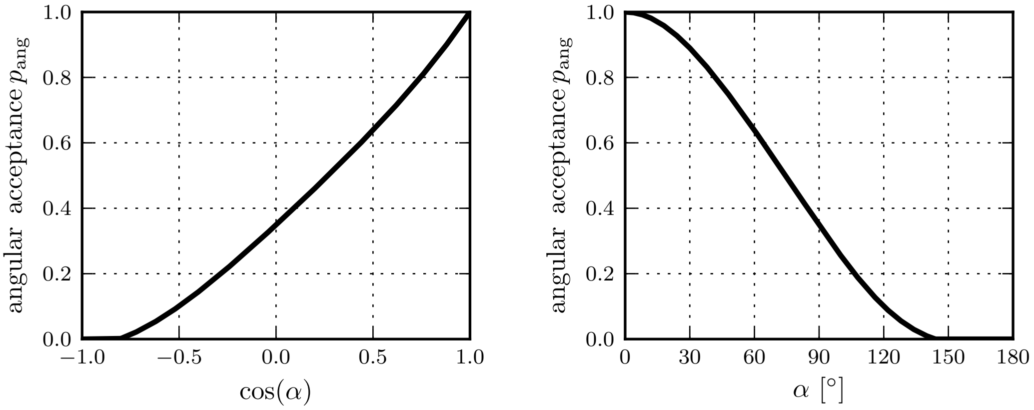

Figure 4.13 Angular acceptance of the ANTARES-style optical modules as used in the simulations done for this work. The angle α is defined as $\alpha = -\mathrm{acos}(\vec{d}_{\mathrm{phot}} \cdot \vec{d}_{\mathrm{PMT}})$, where $\vec{d}_{\mathrm{phot}}$ is the direction of the incident light and $\vec{d}_{\mathrm{PMT}}$ is the direction vector of the PMT. The ANTARES collaboration defined various angular acceptance parameterisations. When simulations for this work were done, the one accepted as best fitting real optical modules was the so-called "Genova" parameterisation [100] shown in this plot.

number of PMTs	1
OM sphere diameter	432 mm
PMT diameter when projected in OM direction	$9.3'' = 236.22$ mm
glass thickness d_{glass}	14 mm
gel thickness d_{gel}	2 mm
glass absorption length l_{glass}	see figure 4.12
gel absorption length l_{gel}	see figure 4.12
glass refractive index n_{glass}	1.472
gel refractive index n_{gel}	1.44
quantum efficiency p_{qe}	peak at 35%, see figure 4.12
collection efficiency p_{coll}	90%
angular acceptance p_{ang}	see figure 4.13

Table 4.2 Constant properties of the ANTARES-style OM containing a single PMT as used for all simulations in this work. Compiled from [101].

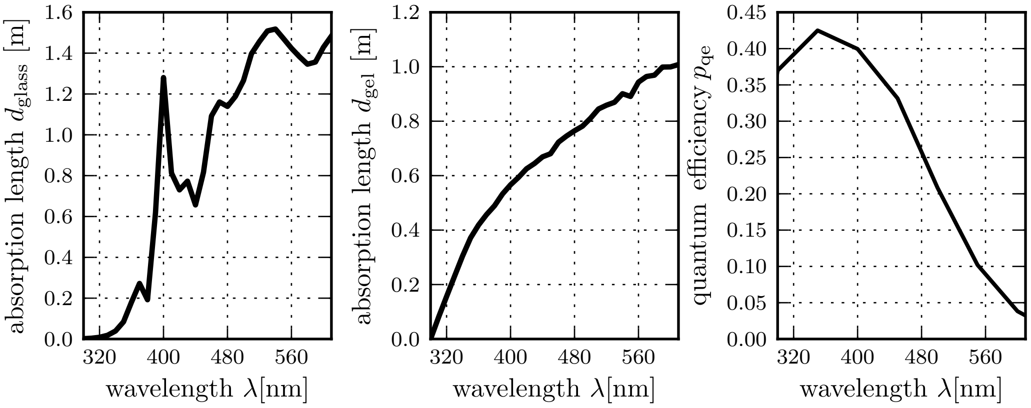

Figure 4.14 Various properties of an multiPMT-style optical module with 31 small PMTs. The OM glass sphere and optical gel properties are exactly the same as for the single PMT optical module (cf. figure 4.12), the PMT's quantum efficency p_{qe} is different. Values taken from [56].

PMT OMs in the previous section is applied, now taking into account absorption in the glass and gel layers.

Note that the detection probability defined in (4.18) needs to be slightly changed due to the fact that the ray-tracing process already accounts for the angular acceptance for a flat PMT photocathode ($\propto \cos(\alpha)$). It therefore becomes

$$p_{\mathrm{detect}}(\lambda,\alpha) := p_{\mathrm{glass}}(\lambda)\cdot p_{\mathrm{gel}}(\lambda)\cdot p_{\mathrm{geom}}\cdot \frac{p_{\mathrm{ang}}(\alpha)}{\cos(\alpha)}\cdot p_{\mathrm{qe}}(\lambda)\cdot p_{\mathrm{coll}}. \tag{4.20}$$

For all subsequent results, the following OM design has been used: each PMT's angular acceptance in a multiPMT design is assumed to be $p_{\mathrm{ang}}(\alpha) = \cos(\alpha)$ (cf. figure 4.13). This corresponds to the purely geometrical angular acceptance. The PMT's effective diameter is 76 mm and its collection efficiency is 90%. The quantum efficiency is shown in figure 4.14. An OM contains 31 PMTs, distributed evenly within the glass sphere (with the exception of the sphere's top, which cannot contain a PMT as it is used for the cable breakout, OM electronics and cooling). The PMT positions and direction are summarised in table 4.3. The OM's glass sphere properties (including the optical gel) are exactly the same as for the ANTARES modules (cf. figure 4.13).

p_x [m]	p_y [m]	p_z [m]	d_x	d_y	d_z
0.000	0.000	-0.200	0.000	0.000	-1.000
0.092	0.053	-0.169	0.460	0.266	-0.847
0.000	0.106	-0.169	0.000	0.531	-0.847
-0.092	0.053	-0.169	-0.460	0.266	-0.847
-0.092	-0.053	-0.169	-0.460	-0.266	-0.847
-0.000	-0.106	-0.169	0.000	-0.531	-0.847
0.092	-0.053	-0.169	0.460	-0.266	-0.847
0.166	0.000	-0.111	0.831	0.000	-0.557
0.083	0.144	-0.111	0.415	0.719	-0.557
-0.083	0.144	-0.111	-0.415	0.719	-0.557
-0.166	0.000	-0.111	-0.831	0.000	-0.557
-0.083	-0.144	-0.111	-0.415	-0.719	-0.557
0.083	-0.144	-0.111	0.415	-0.719	-0.557
0.165	0.096	-0.059	0.827	0.478	-0.296
0.000	0.191	-0.059	0.000	0.955	-0.296
-0.165	0.096	-0.059	-0.827	0.478	-0.296
-0.165	-0.095	-0.059	-0.827	-0.477	-0.296
-0.000	-0.191	-0.059	0.000	-0.955	-0.296
0.165	-0.096	-0.059	0.827	-0.478	-0.296
0.191	0.000	0.059	0.955	0.000	0.297
0.096	0.165	0.059	0.478	0.827	0.297
-0.095	0.165	0.059	-0.477	0.827	0.297
-0.191	0.000	0.059	-0.955	0.000	0.297
-0.096	-0.165	0.059	-0.478	-0.827	0.297
0.095	-0.165	0.059	0.477	-0.827	0.297
0.144	0.083	0.111	0.719	0.415	0.557
0.000	0.166	0.111	0.000	0.830	0.557
-0.144	0.083	0.111	-0.719	0.415	0.557
-0.144	-0.083	0.111	-0.719	-0.415	0.557
0.000	-0.166	0.111	0.000	-0.830	0.557
0.144	-0.083	0.111	0.719	-0.415	0.557

Table 4.3 Positions and directions of the 31 photomultiplier tubes in the multiPMT OM design used in this work. The position is specified relative to the OM centre as the three components of the position vector $\vec{p} = (p_x, p_y, p_z)$. The direction is given in a similar manner as (d_x, d_y, d_z). All PMTs are facing radially away from the OM centre.

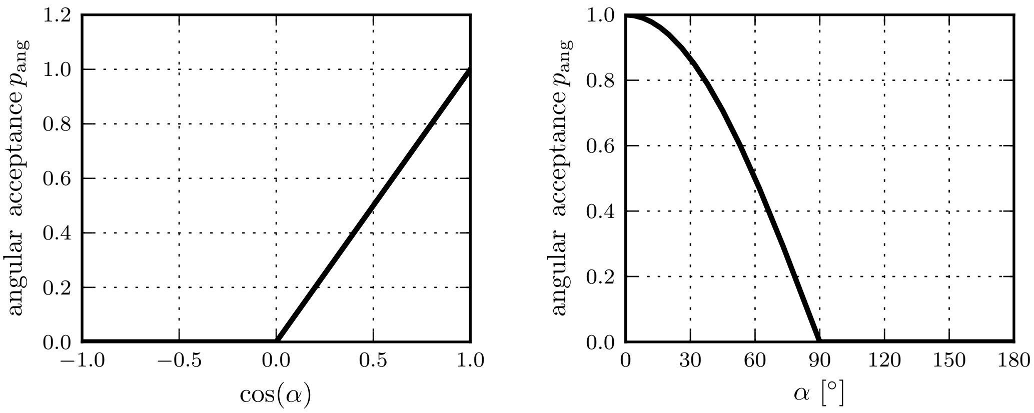

Figure 4.15 Angular acceptance of the multiPMT-style PMTs as used in the simulations done for this work. The acceptance profile shown here ($\propto \cos\theta$) corresponds to a flat photocathode with uniform acceptance regardless of the photon's angle of impact. The factor $\cos\theta$ is purely geometrical.

4.10 Light detection

During the previous step, photons were propagated through the optical module to its PMT's first dynode. For technical reasons, the conversion into photoelectrons was already performed during the OM simulation step. The input of this step are thus "hits" that need to be converted into measured electrical pulses, read out by the OM's electronics. Finally, the event consisting of all detected pulses in the whole detector needs to be evaluated by a trigger algorithm, which decides whether it should be recorded or not.

4.10.1 PMT simulation

The current PMT pulse height and transit time spread (TTS) simulation algorithms assume a very simple model for the simulation of pulse heights and start times from input photoelectrons. All PMT pulses are generated from single photoelectrons taken from the previous OM simulation step. The pulse amplitude is generated from a gaussian centred at 1 p.e., i.e. charge calibration is assumed to already be performed. The gaussian's width is set according to the PMT type to be simulated. For the large ANTARES PMTs, this value is 0.3, for the smaller PMTs used in the multiPMT OMs it is 0.25.

The pulse start time is simulated in a similar manner. The photon arrival time is smeared with a gaussian distribution with a configurable width, the TTS. For a single photoelectron, this value is assumed to be 1.5 ns for the large PMTs and 1 ns for the small ones. The TTS is practically proportional to $1/\sqrt{n_\mathrm{phot}}$, where n_phot is the number of photoelectrons per pulse [102].

4.10.2 Readout electronics simulation using the "ARS" chip

The readout for singlePMT PMTs used in this work is compatible to the original implementation in ANTARES:[10] The signal is read out using a chip design called *analogue ring sampler* (ARS). The chip reads out two channels and is used in an integrating configuration. Once a configurable threshold (0.3 p.e. in this case) is reached, the signal is integrated for 40 ns.[11] The resulting value is then sent to shore together with a timestamp value. After each readout event, the corresponding channel is dead for 250 ns. During this time, the second channel can record hits. In the event that both channels are dead, incoming hits are lost.

4.10.3 A time-over-threshold approach

At the time of this writing, the readout scheme for multiPMT OMs is planned to be a time-over-threshold (TOT) approach. PMT pulses are sampled at a regular interval of the order of 1 ns. In each of the resulting time bins, the electronics check if the PMT signal is above a certain threshold. The threshold value is currently assumed to be 0.3 p.e. The data that is sent to shore is a continuous bitstream from which the pulse start times can be extracted. Additionally, as the pulse widths are correlated to their heights, amplitudes can be extracted. Figure 4.16(a) shows a typical pulse shape, which in this case is modelled as a falling exponential convoluted with a gaussian to include the rising pulse edge. A pulse can thus be characterised by its width (e.g., the time over threshold for 1 p.e.) and by its rise time from amplitude zero to its peak. The single photon pulses (amplitude 1.0) as used in the following simulation have a rise time of 2 ns and a time-over-threshold of 20 ns. The sampling time is 1 ns.

Once a pulse has been identified in the bitstream as a number of consecutive bins, the number of bins is converted back to an amplitude using a fast, lookup-table based calibration code, which includes a time-walk correction. In its current implementation, the calibration tables have to be re-calculated in case the pulse shape or the binning time is changed. Figure 4.16(b) shows the calibration table as a function of the number of bins. The resulting value is the most probable amplitude for this number.

---

[10] This may not be the readout solution used in a final KM3NeT detector design, but at the time this work was started, it was the only solution in existence.

[11] This does not correspond exactly to the behaviour of the ARS chip in ANTARES, where the integration window is only 33 ns, followed by a short dead time of 7 ns needed to switch to the other channel.

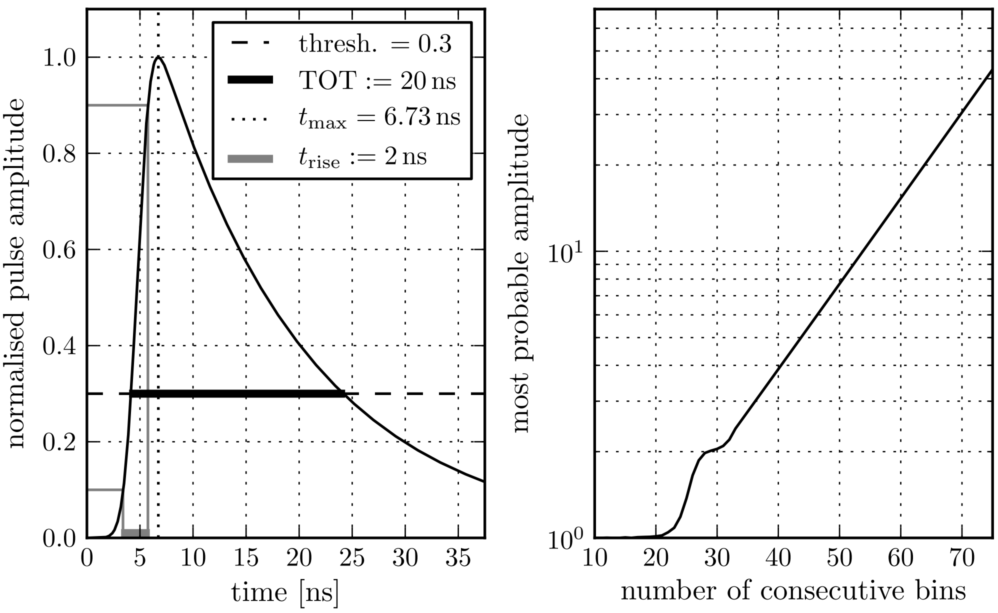

(a) pulse shape

(b) calibration

Figure 4.16 Pulse shape and calibration used for the time-over-threshold simulation. The pulse's falling edge is an exponential, which is convoluted with a gaussian for the rising edge. The rise time is defined as the time from the 10% to the 90% level. The calibration plot (b) shows the most probable amplitude for a given number of consecutive 1 ns bins that are over the threshold level. Up to a level of 32 bins, the calibration includes charge smearing and binning effects and was done for a realistic photon number distribution.

4.10.4 Hit coincidence triggering

Real in-water detectors have a high optical noise rate and thus need to use some kind of trigger algorithm to reduce the data rate. This algorithm needs to determine if a number of hits could correspond to an actual event. For the studies in this work, no particular trigger algorithm is necessary as computation time and data rate are not an issue. Every possible event is sent to the reconstruction and the decision whether to keep it or not is made using a set of quality criteria available after the reconstruction. In this way, the reconstruction algorithm becomes the actual trigger. This is a solution that may be not practical in a real detector, but one that is possible assuming that adequate computational power is available.

Nevertheless, for comparison with other works, a simple trigger algorithm is used. It is based on coincident “L1 hits” on neighbouring floors on the same string. An L1 hit is defined as a coincidence of hits in neighbouring PMTs. In the *string* and *tower* designs, these PMTs will be in neighbouring OMs on the same floor, whereas in the *multiPMT* design, both PMTs will be contained in the same OM. The coincidence time window is 20 ns for the single-PMT designs, the same value that is currently in use for the ANTARES detector. For the multiPMT design, where all PMTs are spaced much more closely, a smaller time of 10 ns was chosen.[12]

In the list of all L1 hits, coincidences are found on either neighbouring floors or next-to-neighbour floors, the event is triggered. The trigger can be made more strict by requesting two non-overlapping coincidences instead of one within a single event and/or by not taking into account next-to-neighbour coincidences. The ANTARES naming convention for this trigger is $n\mathrm{T}m$, where n is the number of non-overlapping coincidences and m is 2 for only neighbouring floors and 3 for neighbouring and next-to-neighbour floors. The coincidence time window for neighbouring floors is set to 180 ns for a floor distance of 30 m, which is the value used in all of the simulations in this work. For next-to-neighbour coincidences, the time window is doubled.

4.11 Muon track reconstruction strategies

Once light has been detected, converted into hits and possibly passed the trigger, the hit distribution has to be converted back into a particle track. This task can be performed by different reconstruction algorithms, two of which shall be presented in this section. The first one is the algorithm currently used by ANTARES with some minor modifications for KM3NeT-sized detectors. The other one is a reconstruction strategy aimed specifically at multiPMT detectors, based on ideas taken from the IceCube reconstruction algorithm [103]. This second algorithm has been developed as part of this work.

4.11.1 The standard ANTARES reconstruction strategy

The standard reconstruction algorithm used for the ANTARES experiment uses a large number of hit selections, a linear pre-fit and several log-likelihood fit stages [77]. It has previously been modified for use with KM3NeT detectors [104, 105]. This section gives a very brief outline of the algorithm that has been re-implemented to be usable with the *IceTray* framework for this work. For the details of the algorithm, refer to [77, 104, 105].

The algorithm starts with a hit filter that is used to clean the hit sample from as much optical noise as possible, while at the same time retaining most of the signal hits. This selection has been modified for KM3NeT to be a bit more relaxed compared to its ANTARES version. Overall, this leads to a slightly worse angular

---

[12] This value was not optimised and was only used as a first guess.

resolution, but provides better efficiency, i.e. more tracks are visible to the algorithm than with its ANTARES counterpart.

These hits are then used in a linear prefit which has been optimised to include the mean distance of tracks from optical modules as a function of the hit amplitude. Tracks are thus not forced to go through the optical module, but rather through a point that is a certain distance away from the OM. This distance is determined by Monte Carlo simulations and hard-coded as part of the algorithm.[13]

The resulting track is transformed (shifted and translated from the original track) eight times. Each of these tracks (including the original track) are then used as input for an “M-Estimator” fit[14] which is used to bring the track estimate nearer to its true value. The result is put through another fit stage using a simple probability density function (PDF).

The best fit result out of the nine tracks considered is then used for a final fit step, using a highly optimised PDF. This function was fitted to Monte Carlo data for ANTARES and has not been changed for KM3NeT.

The final result is a track estimate together with some quality parameters. The ones used here are the number of compatible tracks N_{comp}, defined as the number of tracks out of the nine translated ones that ended up within an angular range of 1°. A second parameter is the quality parameter Λ defined as

$$\Lambda := \frac{\mathcal{L}_{\text{final}}}{N_{\text{DOF}}} - N_{\text{comp}} \cdot 0.1, \tag{4.21}$$

where N_{DOF} is the number of degrees of freedom used for the final fit and $\mathcal{L}_{\text{final}}$ is the value of the log-likelihood function of the final fit.

4.11.2 A new reconstruction algorithm for multiPMT detectors

When reconstructing events from multiPMT detectors, it became clear that the ANTARES reconstruction strategy was not usable for that design. This is primarily due to the fact that the optical module design is fundamentally different. Neither treating each PMT as its own OM in the reconstruction nor combining all hits on a OM into a single hit list proved successful. Especially the final fit PDF, which is heavily tuned to the ANTARES optical module design does only yield successful results if the previous fit step result is already extremely near the actual result. Quite possibly, this is due to the tuning of the PDF to the average hit amplitude distributions and the angular acceptance of large PMTs which is of course different for the smaller ones. Figure 4.17 shows the reconstruction results using the ANTARES

---

[13] The actual values have been determined for ANTARES and were not changed for KM3NeT.

[14] M-Estimators are solutions to a generalised form of maximum likelihood estimation, where the probability density function is replaced with a more general function.

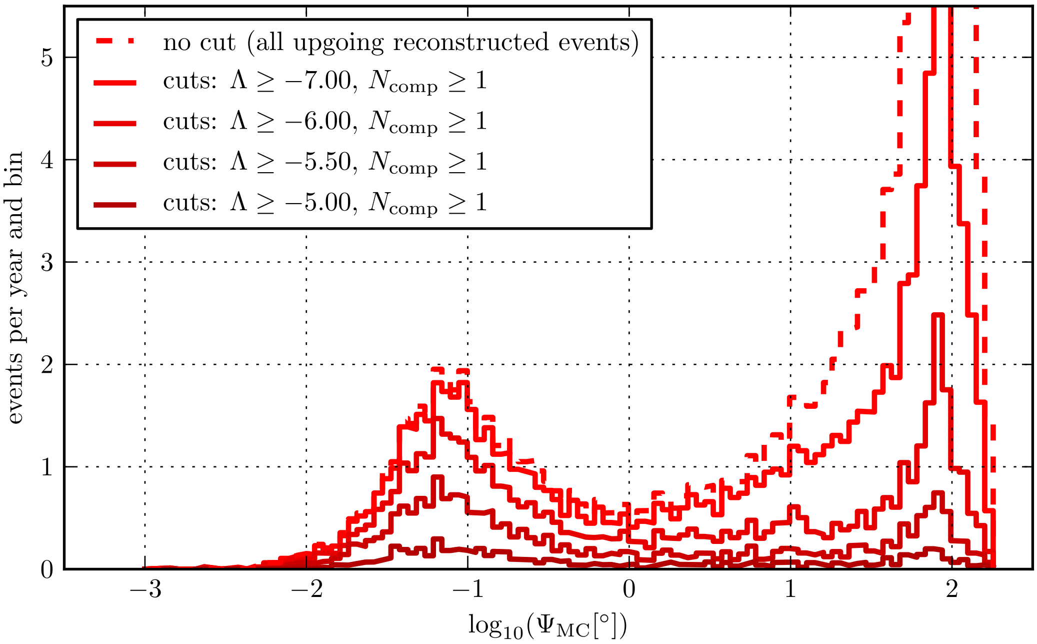

Figure 4.17 Reconstruction results using the standard ANTARES reconstruction algorithm for a multiPMT detector. The plot show the angular error Ψ, i.e. the space angle between the Monte Carlo track and the reconstructed track. To be able to better see the whole angular range, $\log_{10} \Psi$ is shown, with Ψ in units of degrees. Varying the cut level Λ should cut away tracks with large errors while retaining well-reconstructed tracks. It is evident that the cut does not work correctly, as it removes bad tracks as well as good ones. Additionally, a large amount of tracks is reconstructed with a large angular error while only a small amount of tracks ends up with small errors.

algorithm before and after the standard quality cut for a generic multiPMT detector design. It is evident that rejecting events due to this parameter cuts away many well-reconstructed events while at the same time it does not reject enough of the events with large angular reconstruction errors.

To achieve good reconstruction results for multiPMT detectors, a new reconstruction algorithm was developed as part of this work. The aim was not to achieve the best possible angular resolution using a heavily tuned PDF, but rather to implement a robust algorithm with a good reconstruction efficiency and a usable quality parameter.

This new reconstruction algorithm is inspired by work published by IceCube. It uses the "*Pandel*" PDF parameterisation for photon arrival time residuals that is also currently used by IceCube [106], re-fitted to water MC data. Additionally, a track reconstruction error estimator used by IceCube as described in [107] was adapted for KM3NeT.

The “Pandel” parameterisation

The *Pandel* parameterisation [103, 106] is a semi-physical function with 3 free parameters that need to be fitted to Monte Carlo data to represent the time residual distribution at various distances from point light sources. Despite the fact that it only has a small number of free parameters, it can be fitted to results from a large range of different water and OM properties. It is for this reason that it can also be used for muon tracks, which in principle have a different light emission profile than point sources (i.e. cascades). It should be noted that using the Pandel parameterisation for muons should be a better approximation in scattering-dominated media like ice, compared to water with its much larger scattering lengths. It is assumed that this is one reason for the slightly worse angular resolution obtained from the track reconstructions algorithm presented in this section.

The function itself is a gamma distribution and can be written as

$$p(d, t_{\mathrm{res}}) := \frac{1}{N(d)} \frac{\tau^{-d/\lambda_{\mathrm{scat}}} t_{\mathrm{res}}^{d/\lambda_{\mathrm{scat}}-1}}{\Gamma(d/\lambda_{\mathrm{scat}})} \cdot e^{-\left(t_{\mathrm{res}}\left(1/\tau + c_{\mathrm{medium}}/\lambda_{\mathrm{abs}}\right) + d/\lambda_{\mathrm{abs}}\right)} \tag{4.22}$$

$$N(d) := e^{-d/\lambda_{\mathrm{abs}}} \left(1 + \frac{\tau c_{\mathrm{medium}}}{\lambda_{\mathrm{abs}}}\right)^{-d/\lambda_{\mathrm{scat}}}, \tag{4.23}$$

where $N(d)$ is a normalisation factor so that $\int_{-\infty}^{\infty} p(d, t_{\mathrm{res}}) \mathrm{d}t_{\mathrm{res}} = 1$. The function's parameters are the absorption length λ_{abs}, the scattering length λ_{scat} and the time parameter τ. Note that these parameters are effective values obtained as fit results to Monte Carlo data and do not necessarily represent the real scattering and absorption lengths of the medium. The function depends on the distance from the light source d and on the time residuals t_{res}, i.e. the differences between the expected and measured photon arrival times. For muons, d is not the perpendicular distance from the track, but rather the path length of an unscattered photon. It is, however, linearly dependent on the perpendicular distance $d_{\perp}$ and can be calculated assuming a constant Cherenkov angle θ_{C}:

$$d = \frac{d_{\perp}}{\sin \theta_{\mathrm{C}}}. \tag{4.24}$$

For this work, the fit to Monte Carlo data was only intended to show this function's general applicability to the KM3NeT track fit problem and not to be at its absolute optimum. Therefore, in order to reduce the degrees of freedom in the fit procedure, the value for λ_{abs} was chosen to be at the real peak absorption length at 470 nm, i.e. $\lambda_{\mathrm{abs}} = 62.5\,\mathrm{m}$.

For small distances, the Pandel function has a pole at $t_{\mathrm{res}} = 0$. It is also undefined for negative time delays. In order to account for PMT transit-time-spread and readout uncertainties, it can be convoluted with a gaussian with width σ. This width should correspond to the timing accuracy of each PMT. It is non-trivial to calculate this convolution with the high accuracy that is needed for log-likelihood algorithms. However, by splitting the function into different distance and time delay ranges and using different approximations, these problems can be averted [108]. The optimal value of σ for the multiPMT OMs with the readout presented earlier was found to be $\sigma \approx 1.4\,\mathrm{ns}$.

The time-residual distributions for Cherenkov light are different for different PMT orientations with respect to the muon track. These differences can be accounted for by replacing the distance from the muon track d with an effective distance d_{eff}, which includes the angle at which the PMT sees the Cherenkov light [103]:

$$d_{\mathrm{eff}} := ad + b\,, \tag{4.25}$$

where $b := b(\cos\eta)$, with η being the angle between the expected direction of unscattered Cherenkov light from the track and the reverse PMT orientation vector, i.e. $\eta = 0$ for direct light from the track hitting the PMT head-on. The function $b(\cos\eta)$ includes scattering effects and the effects from the PMTs angular acceptance and has to be fitted to Monte Carlo data. The constant a was chosen to be 1 and the function $b(\cos\eta)$ was chosen with the boundary condition $b(\cos(0°)) \approx 0$. Slight deviations from $b(\cos(0°)) = 0$ were allowed during the fit process in order to account for systematic uncertainties. In this way, the time residual distributions could first be fitted for head-on photons (i.e. $\eta \approx 0$). The angular dependencies were then fitted in a second step.

Photon survival probability

The parameterisation is constructed so that the normalisation factor $N(d)$ (cf. (4.23)) represents the total photon survival probability as a function of the photon path length d independent of photon arrival time. The exponential term describes the absorption component whereas the second term can be seen as a correction to include scattering processes. Fitting this function to Monte Carlo data can help to resolve the large correlation between the λ_{scat} and τ parameters that is present at short distances.

Fit to Monte Carlo data for head-on photons

A full fit of λ_{scat} and τ over a large range of distances and time differences for photons with $\cos\eta > 0.9$ yielded $\lambda_{\mathrm{scat}} = 66.89\,\mathrm{m}$ and $\tau = 163.55\,\mathrm{ns}$. The resulting

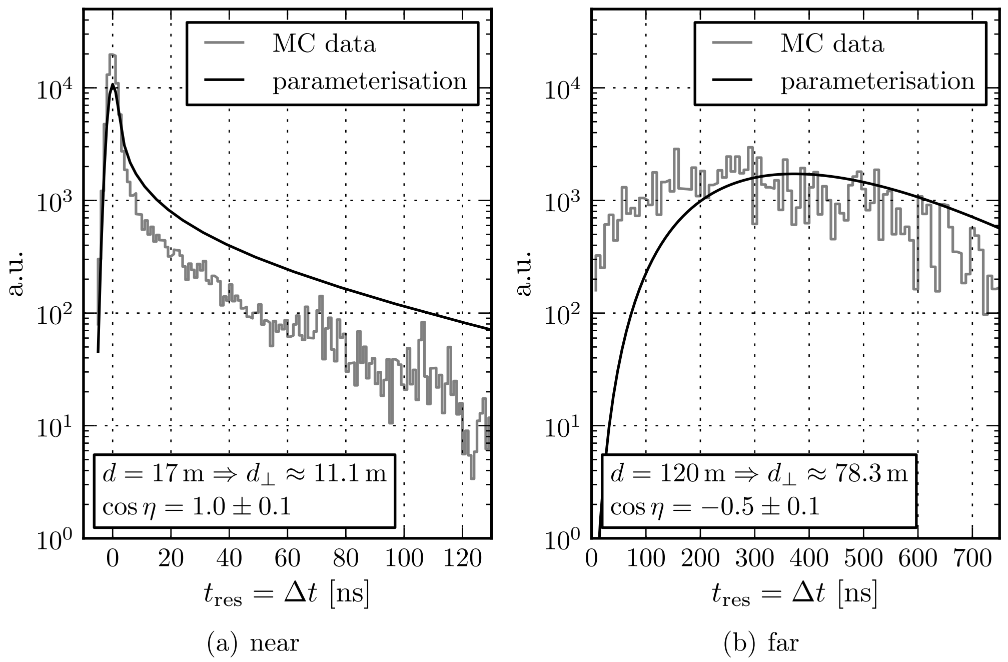

(a) near

(b) far

Figure 4.18 Fit of the Pandel function $p(d, t_{\mathrm{res}})$ to Monte Carlo time residual distributions for two distances, near and far from the muon track. For the far track, the PMT is looking away from the track ($\cos\eta = 0.5$).

parameterisation does not accurately describe the Monte Carlo distributions at all distances and time differences (cf. figure 4.18 and 4.19). This suggests that the Pandel function with only those two free parameters may not be the optimal choice for a sea water-based detector with its long scattering length. Nevertheless, the final reconstruction results are fairly good, despite the crude description of the time residuals. Future work should be invested in finding a better PDF parameterisation, either by using a better fit of the Pandel function with more free parameters or by using a new parameterisation altogether. For the purposes of this work, however, the results obtained using this parameterisation are sufficient. When looking at the final reconstruction results, it should be kept in mind that substantial improvements may be possible by improving the reconstruction algorithm at this point.

Additional effective path length for different PMT orientations

The fit of $b(\cos\eta)$ to Monte Carlo data can be seen in figure 4.20. The process was performed as follows: first, a fixed angle η was chosen. For this angle, the best fitting value of b was determined using a χ^2 fit. This process was then repeated for

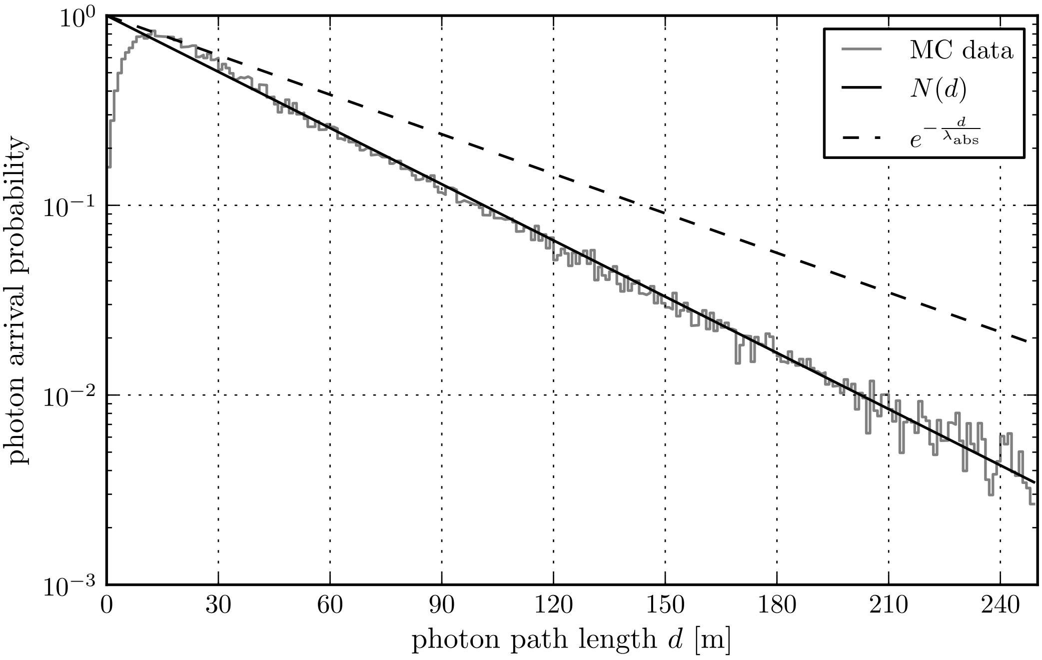

Figure 4.19 Photon survival probability vs. photon path length. The plot shows Monte Carlo data overlaid with the fit of $N(d)$ (cf. (4.23)). Additionally, an exponential containing only the absorption length is shown for comparison.

a number of angles. The results can be seen as data points in figure 4.20. Note the kink in the distribution at $\cos\eta \approx 0.14$. This is attributed to the angular acceptance of the PMTs used in the simulation which is linear in $\cos\eta$ for light coming from the front but zero for light coming from the back. It is therefore not differentiable at $\cos\eta = 0$ (cf. figure 4.13), an effect that seems to be visible in this fit. Starting from the kink, almost all light hitting a PMT is scattered, whereas for smaller angles, a substantial amount of direct light is left. For these reasons, the fit function $b(\cos\eta)$ was composed of two parts

$$b(\cos\eta) := \begin{cases} b_0 + \frac{b_{\mathrm{frac}}}{\cos\eta + b_{\mathrm{shift}}} & \text{for } \cos\eta \geq k \\ b_1 + b_2\cos\eta & \text{for } \cos\eta < k \end{cases} \tag{4.26}$$

with the condition to be continuous at $\cos\eta = k$. Note that this is a purely empirical definition which was chosen to best fit the Monte Carlo data.

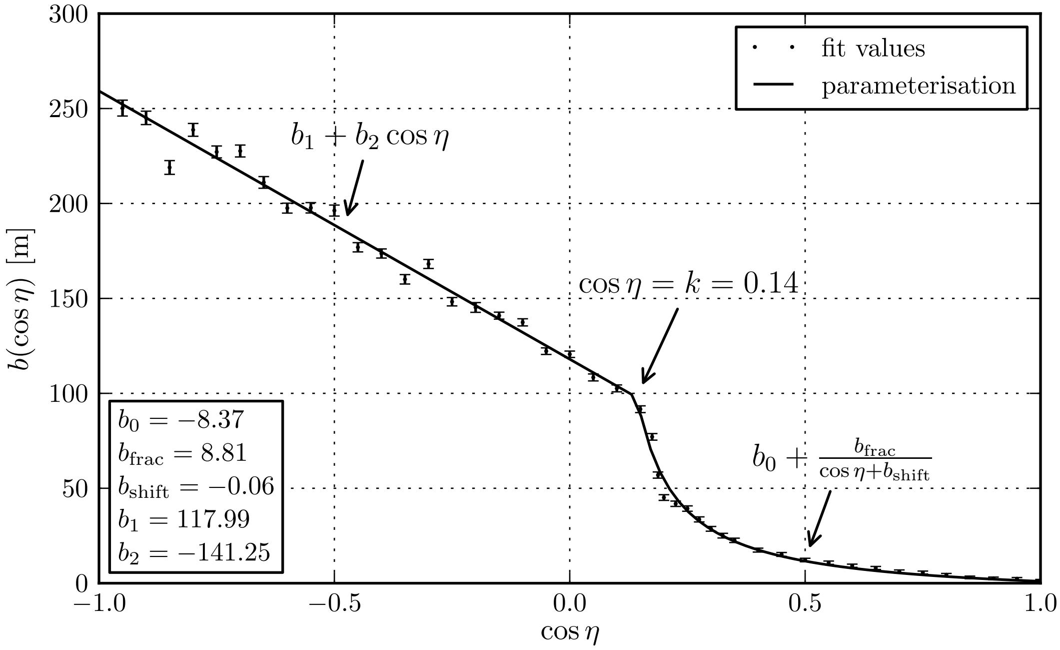

Figure 4.20 Angular dependency of the additional track length $b(\cos\eta)$ included in the effective distance d_{eff} (see (4.25)). The function corresponds to an effective additional path length for PMT orientations that face away from the direction of direct light. For larger values of η (i.e. lower values of $\cos\eta$), more and more scattered light with a larger track length reaches the PMT. The data points with error bars correspond to fits to Monte Carlo data at a particular value of $\cos\eta$, the solid line is the parameterisation used in the reconstruction code (see (4.26)).

Minimiser algorithms and first guess

When the Pandel PDF is finally used in a log-likelihood track reconstruction process, some kind of minimisation algorithm needs to be used. In the current implementation, the minimisation process consists of two steps: first, a minimum is determined using the downhill simplex algorithm [109] as implemented in the MINUIT package using the result of a simple linear fit as a starting point.[15] As this algorithm can possibly converge into a local minimum and miss the global one, a second minimisation process is performed, taking the simplex result as a starting point. It uses the exact same likelihood function as before, but finds the optimal value using the CMA-ES

---

[15] This linear fit assumes that the track goes directly through all hit PMTs. The algorithm finds the optimal value analytically.

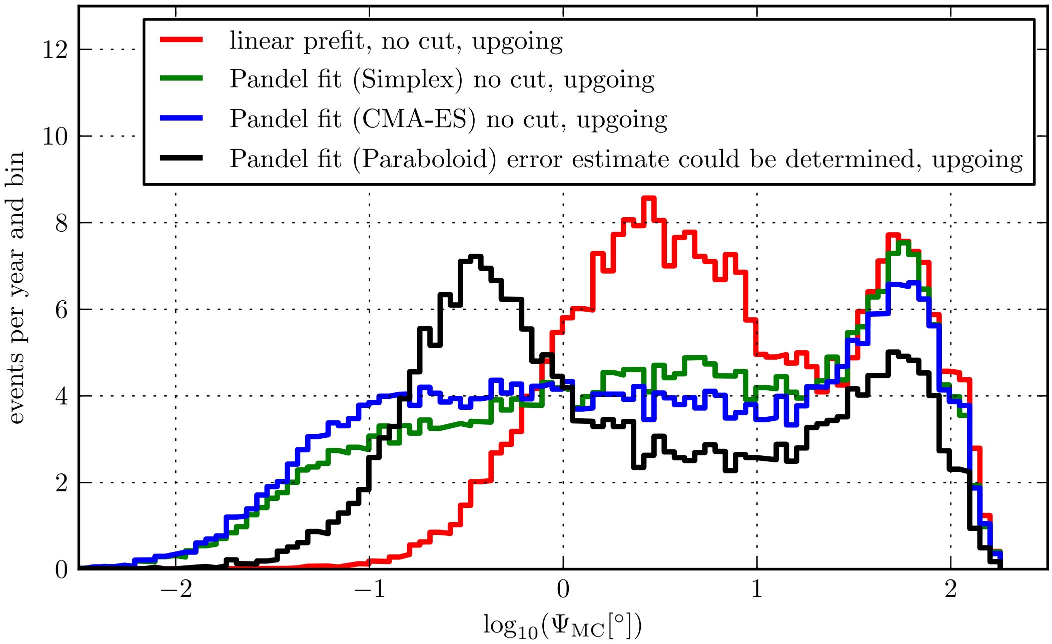

Figure 4.21 Angular error after the four fit stages for an example multiPMT detector with a E^{-2} neutrino energy spectrum. The first log-likelihood step after the initial linear fit improves the angular error substantially, whereas the secondary CMA-ES optimisation only finds the minimum for some tracks where the Simplex minimiser failed. The fourth fit is performed during the pointing accuracy determination step ("paraboloid").

evolutionary algorithm [110]. Though these methods are usually aimed at higher-dimensional search spaces, this algorithm nevertheless improves the reconstruction for tracks where the global minimum was only closely missed. Figure 4.21 shows the angular error after each of the three fit stages: the preliminary linear fit, the Pandel PDF as minimised by the Simplex algorithm and the fit after the additional CMA-ES minimisation. The fourth stage shown is for the track direction after the pointing accuracy estimation presented in the following section, which may re-fit the track.

Hit filtering

To provide the reconstruction algorithm with less optical noise hits, a simple hit filtering algorithm, developed as part of another work [111], is used before the actual fitting process. The algorithm starts with the whole set of hits. Each hit is then compared to all remaining hits on the same, the neighbouring and the next-to-neighbouring floors on the same string. Any combination with a time difference smaller than 300 ns is stored as part of a potential hit cluster containing a number of hits N_{clust} in addition to the initial hit. Within each cluster, the angle $\theta_i := \text{atan}\frac{\Delta t_i}{\Delta z_i}$ is calculated for each of cluster hit with respect to the initial hit. Here, Δt_i and Δz_i are the differences in hit time and z-coordinate, respectively. Now, hits are iteratively removed from the cluster until the RMS of θ is smaller than a pre-defined threshold (which was chosen as 1° in this case). In each iteration the hit with the largest deviation from the mean is removed. All hits in clusters where the remaining number of hits is larger than a threshold are retained and marked as selected. This threshold was chosen to be $N_{\text{clust, sel.}} \geq 4$.

A measure for track pointing accuracy

If the likelihood function's shape is assumed to be Gaussian (at least locally around its maximum), the track reconstruction error can be estimated from the gaussian's width σ. A gaussian maximum in the likelihood function becomes a minimum of a paraboloid in the negative log-likelihood space. For the one-dimensional case, the width σ thus is the distance from the minimum of the negative log-likelihood functionto the point where this function has changed by $\frac{1}{2}$, i.e.

$$\Delta\left(-\log\mathcal{L}\right) = \frac{1}{2}. \tag{4.27}$$

This track reconstruction error can be used as a powerful quality estimator. An implementation for IceCube, where the width is calculated in the two-dimensional angular space (zenith and azimuth), is discussed in [107, 112]. To reduce the 5-dimensional problem (with three dimensions for the track position and two dimensions for its direction) to a two-dimensional problem, the following algorithm is used: first, fixed track directions are defined around the previously determined minimum in the log-likelihood space. These directions are on concentrical circles around the optimal direction in zenith and azimuth[16]. For each of these directions, the log-likelihood function is optimised by varying the track position while leaving the direction fixed. The resulting log-likelihood values are used to analytically determine the optimal two-dimensional paraboloid. Under the condition given in (4.27), this yields an error ellipse with two width parameters, one for each axis of the ellipse (σ_1 and σ_2). Also resulting from this procedure is a new track direction estimate (i.e. the centre of the ellipse), which is used as the new fit direction. In case the analytical determination of the ellipse failed, the fit is rejected.

---

[16] To avoid distortions for directions near the poles, the coordinate system is rotated for the calculations of the minimum's width, so that the track direction is facing towards the equator, i.e. an zenith of 90°.

For this work, the IceCube algorithm has been re-implemented. Although both the σ_1 and the σ_2 parameters are available, for reasons of simplicity only their geometrical mean

$$\sigma := \sqrt{\frac{\sigma_1^2 + \sigma_2^2}{2}} \tag{4.28}$$

has been used as a quality parameter. Further studies should investigate the separate treatment of both direction errors.

The track estimation results after this step can be seen in figure 4.21, where some badly reconstructed tracks are missing after the "paraboloid" stage due to the rejection step. Unfortunately, there seem to be slight problems with the paraboloid determination, as the peak of the angular error histogram is slightly shifted to worse angular errors. Due to time constraints, this shift could not be investigated yet.

5 Analysis techniques

> I reject your reality and
> substitute my own.
>
> *(Adam Savage)*

Reconstructed tracks can now be subjected to different analysis steps. Some of the most important benchmark analysis techniques for neutrino telescopes will be presented in this chapter. There are certainly more analyses that can be performed than those presented in this chapter (including searches for diffuse fluxes). For the preliminary studies done for KM3NeT, the following detector properties were considered.

5.1 Angular resolution

One very important quality of a neutrino telescope is its angular resolution. A good angular resolution allows the detector to resolve track directions with a small error and thus enables it to detect point-sources. The angular resolution is influenced by several factors, amongst them the geometrical layout of the detector, its total photocathode area and density and of course the quality of the track reconstruction technique that is used. Most commonly the value that is presented is the median space angle Ψ between the Monte Carlo track direction $\vec{d}_{\mathrm{MC}}$ and the reconstructed direction $\vec{d}_{\mathrm{reco}}$

$$\Psi = \mathrm{acos}\left(\vec{d}_{\mathrm{MC}} \cdot \vec{d}_{\mathrm{reco}}\right), \tag{5.1}$$

where $\vec{d}_{\mathrm{MC}}$ and $\vec{d}_{\mathrm{reco}}$ are assumed to be unit vectors. Optionally, the angular difference can be expressed in two dimensions, leading to a 2D point-spread function.

5.2 Neutrino effective area

The effective area of a neutrino telescope is a way to define the fraction of particles incident on the detector that can be reconstructed without being dependent on the the actual detector's size. When used as a function of energy, it is also independent of the incident spectrum. It includes all possible effects like absorption in the earth, the interaction probability in or near the detector and its actual detection probability, possibly after reconstruction quality cuts. For this work, the "neutrino effective area" $A_{\mathrm{eff};\nu}(E_\nu, \theta_\nu)$ will be used exclusively, i.e. it will be defined in terms of neutrino

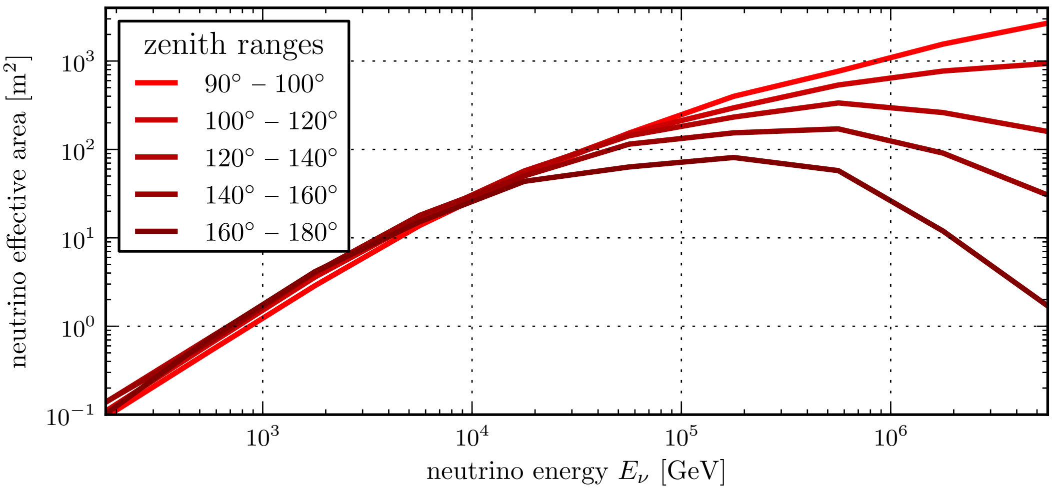

Figure 5.1 Typical example of effective areas for a neutrino detector for different zenith ranges. Note that due to neutrino absorption in the earth at high energies, the effective area above $E_\nu \approx 10^4\,\mathrm{GeV}$ decreases significantly with increasing zenith angle and thus increasing neutrino path lengths through the earth.

energy E_ν and the neutrino zenith angle θ_ν.[1] The event rate N_ν for a certain neutrino flux $\frac{\mathrm{d}\Phi_\nu}{\mathrm{d}E_\nu\theta_\nu}$ can then be calculated from the effective area:

$$N_\nu = \int A_{\mathrm{eff};\,\nu}(E_\nu, \theta_\nu)\,\frac{\mathrm{d}\Phi_\nu}{\mathrm{d}E_\nu\theta_\nu}\,\mathrm{d}E_\nu\mathrm{d}\Omega_\nu. \tag{5.2}$$

Typically, the effective area is highly energy-dependent, ranging from tiny areas at low energies (at about $E_\nu \leq 10\,\mathrm{GeV}$) where only a small amount of light is produced by the generated muon, up to a few hundred metres at higher energies above $E_\nu \approx 100\,\mathrm{TeV}$.[2] When looking downwards, the effective area will fall off at these high energies due to absorption of neutrinos in the earth. This effect is not visible when looking upwards. Effective areas are usually given in units of metres as a function of energy for a specific zenith range. Examples of effective areas can be seen in figure 5.1. Note that, when results are given later on in this work, the effective are will always be for upgoing tracks, i.e. for a zenith range of [90°; 180°].

---

[1] Other effective area types like the *muon* effective area will not be discussed here. The term “effective area” will be used in the following to consistently refer to “neutrino effective area”.

[2] These approximate values are for km^3-sized telescopes.

5.3 Point-source sensitivity and discovery potential

Searching for point-like sources of neutrino emission is one of the most important tasks of a neutrino telescope. Therefore, many techniques exist to look for point sources in the recorded data and to set exclusion limits in the case that no point sources are found. The algorithm used in this work to determine such detector sensitivities and discovery potentials is based on a binned point-source search. The more complex technique of unbinned searches will not be considered here.

The two basic questions are: can a source be seen with at least a certain *significance* (e.g. 5σ) in a given amount of hypothetical experiments (e.g. 50%)? And, if no source is discovered, what is the source flux that can be excluded at a given confidence level (e.g. 90%)? The answer to the first question yields the detector's *discovery potential* [113], whereas the second question leads to the detector's *sensitivity* [114].

Both calculations require the expected number of signal events n_{sig} and the number of background events n_{bkg} seen from the direction of a certain source. As the location of a source is assumed to be known, n_{bkg} can be kept low by only using events with directions that are near the actual source's direction, i.e. by using a so-called *search cone* with a defined opening angle θ_{cone}. Additionally, the relative number of signal and background events can be influenced by various track quality cuts. The cuts leading to optimal values for discovery potential and sensitivity will usually be different and have to be found using an optimisation process.

As the signal and background fluxes vary for different zenith angles due to earth absorption processes, the analysis has to be performed for a range of different zenith bins. For KM3NeT, the rotation of the earth has to be taken into account to convert from event numbers in zenith bins to event numbers for different declination bins. This can be achieved by distributing the event rates according to the fraction of time a certain zenith direction is visible in a certain declination band. The total visibility per year of each declination is shown in figure 5.2. In all these analyses, the fluxes are assumed to have an azimuthal symmetry.

5.3.1 Discovery potential

The discovery potential of a detector can be determined by calculating the "least detectable signal" $\mu_{\mathrm{lds}}(n_{\mathrm{bkg}})$, assuming a given number of background events according to [113]: given an expected number of background events n_{bkg}, the Poissonian probability of observing more than a certain number of events $P(\geq n_{\mathrm{obs}}|n_{\mathrm{bkg}})$ can be calculated. In case this number is very small, e.g. $P(\geq n_{\mathrm{obs}}|n_{\mathrm{bkg}}) < \alpha$, something interesting might have been detected. As an example, for a 5σ detection (area in a one-sided gaussian tail), α would be chosen as $\alpha = 2.87 \cdot 10^{-7}$. For a given α, the critical number of events n_{crit}, where $P(\geq n_{\mathrm{crit}}|n_{\mathrm{bkg}}) < \alpha$ can be calculated. This is

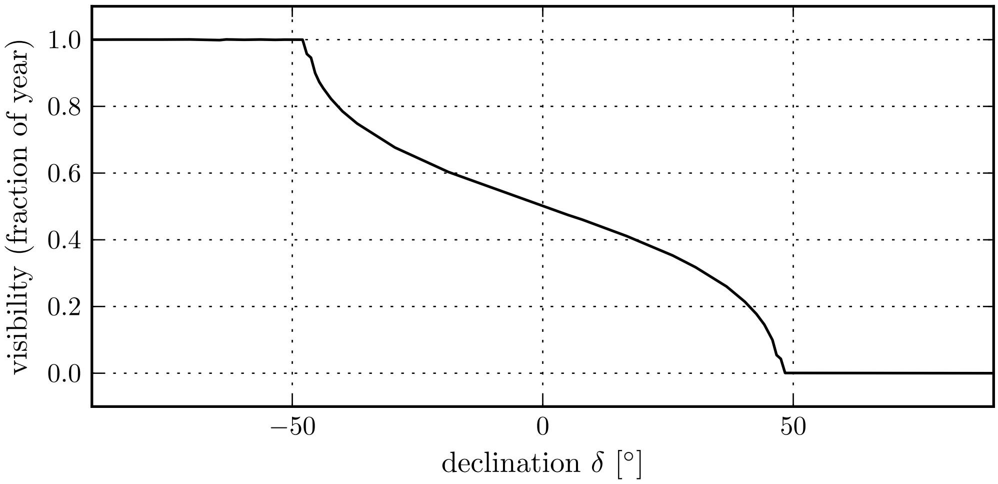

Figure 5.2 Source visibility versus declination δ. Sources are regarded as visible if they are below the horizon. The shown values are for a detector located in the Mediterranean at E 6° 10′ N 42° 48′ (grid WGS84), i.e. the ANTARES site.

the number of events that need to be observed in order to report a detection, in this case with 5σ. In the presence of a real signal n_{sig}, the probability (statistical power $1-\beta$) that n_{crit} or more events are observed is $1-\beta = P(\geq n_{\mathrm{crit}}|n_{\mathrm{bkg}} + n_{\mathrm{sig}})$. The "least detectable signal" μ_{lds} is then defined as the value of n_{sig} where this equality is satisfied for a given value of $1-\beta$.

Finding the minimum of the parameter ${}^{\mu_{\mathrm{lds}}}/_{n_{\mathrm{sig}}}$, yields an optimal set of cuts for discovering the source at significance level α with probability $1-\beta$. This parameter is often called the "model discovery factor" (MDF). In the following, α is chosen for a 5σ detection with a probability of $1-\beta = 50\%$.

5.3.2 Sensitivity

If no signal source is found, an upper limit for a certain source flux can be given [115]. The method is similar to the one presented in the last section, only the least detectable signal has to be replaced with an "average upper limit" $\bar{\mu}_{\mathrm{C.L.}}(n_{\mathrm{bkg}})$ for a certain confidence level (C.L.) calculated using the Feldman-Cousins approach [114]: in absence of a measured signal n_{obs}, the Feldman-Cousins upper limit $\mu_{\mathrm{C.L.}}(n_{\mathrm{obs}}, n_{\mathrm{bkg}})$ needs to be averaged for a certain background expectation n_{bkg}. This is done by weighting the upper limits by their Poisson probability of occurrence:

$$\bar{\mu}_{\mathrm{C.L.}} = \sum_{n_{\mathrm{obs}}=0}^{\infty} \mu_{\mathrm{C.L.}}(n_{\mathrm{obs}}, n_{\mathrm{bkg}}) \frac{(n_{\mathrm{bkg}})^{n_{\mathrm{obs}}}}{(n_{\mathrm{obs}})!} \exp\left(-n_{\mathrm{bkg}}\right) \tag{5.3}$$

Again, the optimal set of cuts can be found by minimising the parameter ${}^{\bar{\mu}_{\mathrm{C.L.}}}\!/\!{}_{n_{\mathrm{sig}}}$, called the “model rejection factor” (MRF). The detector’s flux sensitivity can then be written as

$$\left(\frac{\mathrm{d}\Phi}{\mathrm{d}E}\right)_{\mathrm{sens}} := \frac{\bar{\mu}_{\mathrm{C.L.}}}{n_{\mathrm{sig}}} \left(\frac{\mathrm{d}\Phi}{\mathrm{d}E}\right)_{\mathrm{source}} , \tag{5.4}$$

where $({}^{\mathrm{d}\Phi}\!/\!{}_{\mathrm{d}E})_{\mathrm{source}}$ is the assumed source flux yielding the signal expectation used to calculate the MRF. The resulting flux is the largest flux that can be excluded by the detector with the given C.L. In the following, the confidence level is chosen to be 90%.

Part III

Results

6 Comparison between simulation chains

> People are very open-minded about new things — as long as they're exactly like the old ones.
>
> *(Charles F. Kettering)*

This chapter presents results obtained for a single reference detector design (based on the *singlePMT* floor layout), simulated with the two different simulation chains available: the legacy ANTARES toolchain and the new simulation chain developed in this work. To determine if the results from the two simulation chains are compatible, data simulated with both of them have been reconstructed using the same algorithm. This shows the influence of different approaches and approximations made in the simulation on the final results.

6.1 Detector design, environment and simulation parameters

For this analysis, a small reference detector design based on the "string" detector design (ANTARES-like) floor layout with a volume of approximately $0.5\,\mathrm{km}^3$ was chosen. It consists of 154 strings in a hexagonal seafloor layout (cf. figure 6.1) with an inter-string distance of $d_{\mathrm{string}} = 91\,\mathrm{m}$. The strings have an instrumented length of 570 m with 20 floors per string. This corresponds to a vertical floor distance of 30 m. The distance from the seabed to the first floor is 100 m with the seabed being at a depth of 3500 m.

All simulations have been performed with an optical background rate of 75 kHz (per $9.3''$ PMT) in the "ANTARES water" medium defined in section 4.5.1. The muon neutrino signal has been simulated as a full sky sample ($\Omega = 4\pi$) with an E^{-1} spectrum and then re-weighted to an E^{-2} benchmark flux with the following normalisation:

$$\frac{\mathrm{d}\phi_{\nu_\mu}}{\mathrm{d}E} = 1.0 \cdot 10^{-8} \left(\frac{E}{\mathrm{GeV}}\right)^{-2} \mathrm{GeV}^{-1}\mathrm{cm}^{-2}\mathrm{s}^{-1} \tag{6.1}$$

This flux is distributed evenly to neutrinos and anti-neutrinos. The background signal corresponds to the atmospheric flux described in section 2.1.9. Neutrinos have been simulated in an energy range from 10^2 GeV to 10^7 GeV. The simulations

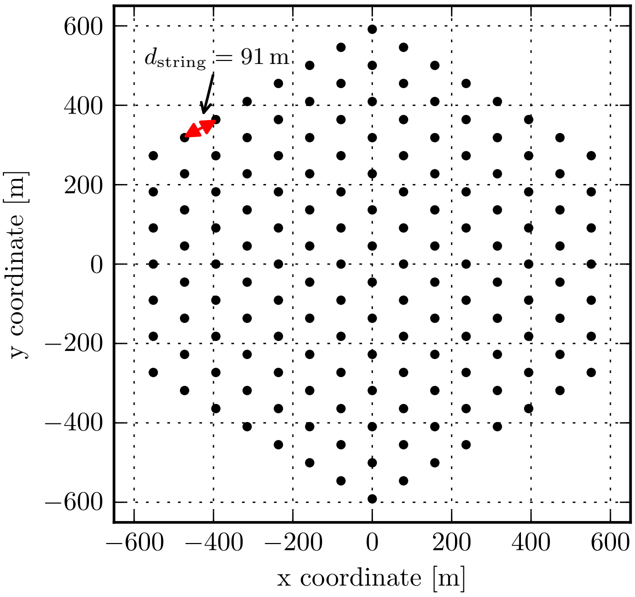

Figure 6.1 Hexagonal sea floor layout with 154 strings and a string distance of 91 m as used for the comparison between simulation chains. Each dot represents a detector string.

do not include atmospheric muon background at this point. Muon propagation and photon tracking is done using the *km3* tool for the old simulation chain. The new simulation chain uses the unified shower/muon simulation presented earlier in section 4.8.

As the neutrino sample simulated with the new algorithm was also used for other, larger detectors to obtain results presented later on, the light generation ("active") volume for the detector was chosen substantially larger than the detector's instrumented volume. In contrast to that, all data produced with the legacy ANTARES code uses its default active volume definition for the muon propagation, i.e. a cylinder around the instrumented volume, extended by three absorption lengths.

In the old ANTARES simulation chain, the hadronic cascade at the interaction vertex is simulated using the "geasim" tool which does not take light scattering effects into account. Therefore, for the sake of comparability of the two simulation chains, light from the vertex cascade was removed from both simulations.[1]

---

[1] Note that in all of the following sections, where only the new simulation chain is used, light from the hadronic cascade at the vertex is fully included.

6.2 Basic quantities before reconstruction

Before reconstructing tracks, distributions of the most important hit-related quantities of the muon and photon-propagation step have been compared between the two simulations chains (cf. figure 6.2). For the results presented in this section, in order to be independent of effects due to the event generator, the *genhen* tool has been used as a generator for both simulation chains. For all other results, the ANIS event generator has been used as part of the new simulation chain. The upper plot shows the distribution of the cosine of the angle θ between the expected photon direction with respect to the Monte Carlo muon track and the OM axis. Below, the distribution of the distance d_{track} between the Monte Carlo track and the OM recording the photon is shown. The two lower plots show the time residual distribution and the distribution of the recorded charges, respectively. The step in the d_{track} distribution at $d_{\text{track}} = 100\,\text{m}$ corresponds to a hit selection done as part of the ANTARES reconstruction strategy. The step in the time residual distribution at $t_{\text{res}} = 40\,\text{ns}$ corresponds to the integration time of the first ARS channel. After this time, the second channel can take over.

The only notable difference between the two simulations is the time residual distribution, where the peak around $t_{\text{res}} = 0$ is slightly broader for the new simulation chain. This is due to differences in light dispersion simulation between the two chains. Whereas the new simulation includes a full simulation of photons with the correct spectrum and thus automatically includes light dispersion because of the included refractive index distribution, the old simulation uses a single wavelength for the simulation of its photon tables. Only in the very last step of *km3*, the light dispersion is included as a smearing in time according to pre-generated distributions. These distributions do not seem to fully reproduce the results obtained with the full simulation performed as part of the new algorithm developed for this work.

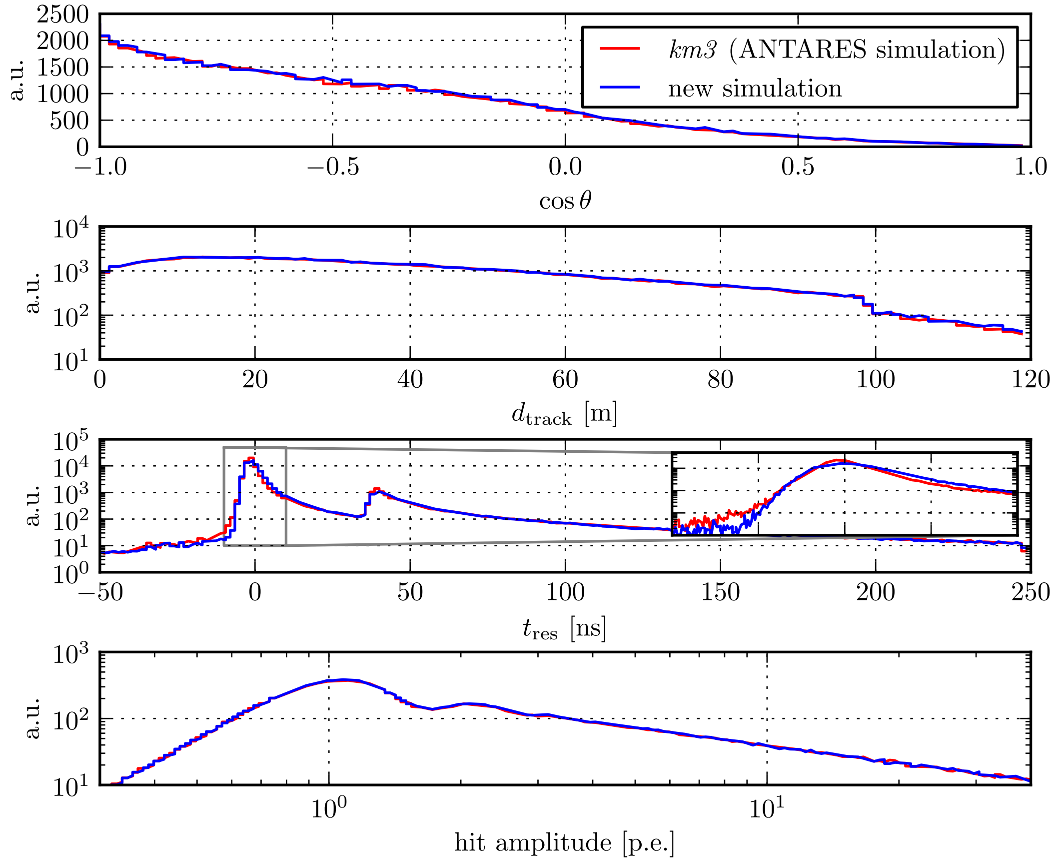

Figure 6.2 Distributions of basic hit-related quantities. The hits used to generate the distributions shown here are the ones selected for the final step of the ANTARES reconstruction strategy. From top to bottom, the plots show distributions of the cosine of the angle between the expected photon direction and the OM axis, the distance from the Monte Carlo track, of the time residuals and the hit amplitudes.

6.3 Quality cut distribution

One of the interesting quantities to study after the reconstruction algorithm has been used on simulated data, is the reconstruction quality variable. To this end, simulated neutrinos from both software chains have been reconstructed using the default ANTARES algorithm (with KM3NeT modifications, cf. sec. 4.11.1).[2]

During its development, the algorithm's final PDF has been heavily optimised to the MC results obtained from the old ANTARES simulation toolchain, especially to the photon output of the *km3* tool. When comparing the distribution of the Λ quality parameter defined in (4.21), small differences are visible only at high energies ($E_\nu > 10^6\,\mathrm{GeV}$), (see figure 6.3). The overall shape of the distributions is compatible for both simulation chains: there are two overlapping peaks, one containing well-reconstructed tracks, the other one mainly containing badly reconstructed ones. The location of the peak containing the "good" tracks is shifted starting at energies of about $E_\nu \approx 10^{3.5}\,\mathrm{GeV}$; it starts out at about $\Lambda \approx -5$ for low energies and is located at $\Lambda \approx -4.5$ above that threshold.

Only for the new simulation, another minute shift of the peak becomes visible at the highest energies ($E_\nu \approx 10^6\,\mathrm{GeV}$). A possible explanation for this behaviour can be found in the differences in the simulation algorithms for cascades along muon tracks: the *km3* tool distributes pre-simulated cascades obtained from a full Geant3 simulation along the muon track, but only has a limited range of cascade energies up to 100 GeV at its disposal. Higher energies are simulated by superimposing these cascades. In the new simulation algorithm, cascades of any energy are simulated, with their energy range not limited by the lack of photon tables. The price for this, however, is that cascades are only simulated according to parameterised angular and longitudinal distributions. Differences between these two approaches should only be visible at the highest energies. Because these differences may lead to differences between the simulated hit distribution and the distribution expected by the reconstruction's PDF, such a shift is at least plausible.

Overall, the new simulation chain yields about 5% more events, an effect that seems to get larger with higher energies. This effect can be attributed to the ANIS generator, as it is not visible when tracks generated by the old ANTARES *genhen* tool are propagated with the new muon simulation code instead of *km3*. This is consistent with the previous observation in section 6.2: when using the same events, the low level hit distributions are unchanged except at time residuals near zero, an effect that is independent of muon energy. The reason for this difference could not be found, but it is believed that this is either due to the different parameterisations

---

[2] Note that in contrast to the previous section, the event generator that has been used as part of the new software chain is now ANIS. This is also true for all results shown from now on. The *genhen* generator was still used to generate the results for the old ANTARES software chain.

of the νN structure functions (CTEQ5 for ANIS and CTEQ6 for *genhen*) or due to the fact that the *genhen* “can” size is chosen too small for such high energy events.

The optimal cut levels for each simulation chain have been determined, each one by optimising for best E^{-2} flux point-source sensitivity, albeit without contributions from atmospheric muons. This type of background was omitted as it would have required extensive amounts of computation time to include, which was not available in the frame of this work. The primary objective, however, was to compare the two simulation chains which was possible without the inclusion of atmospheric muons. The following sections show the angular resolution, effective area and point source sensitivity achievable with these cuts.

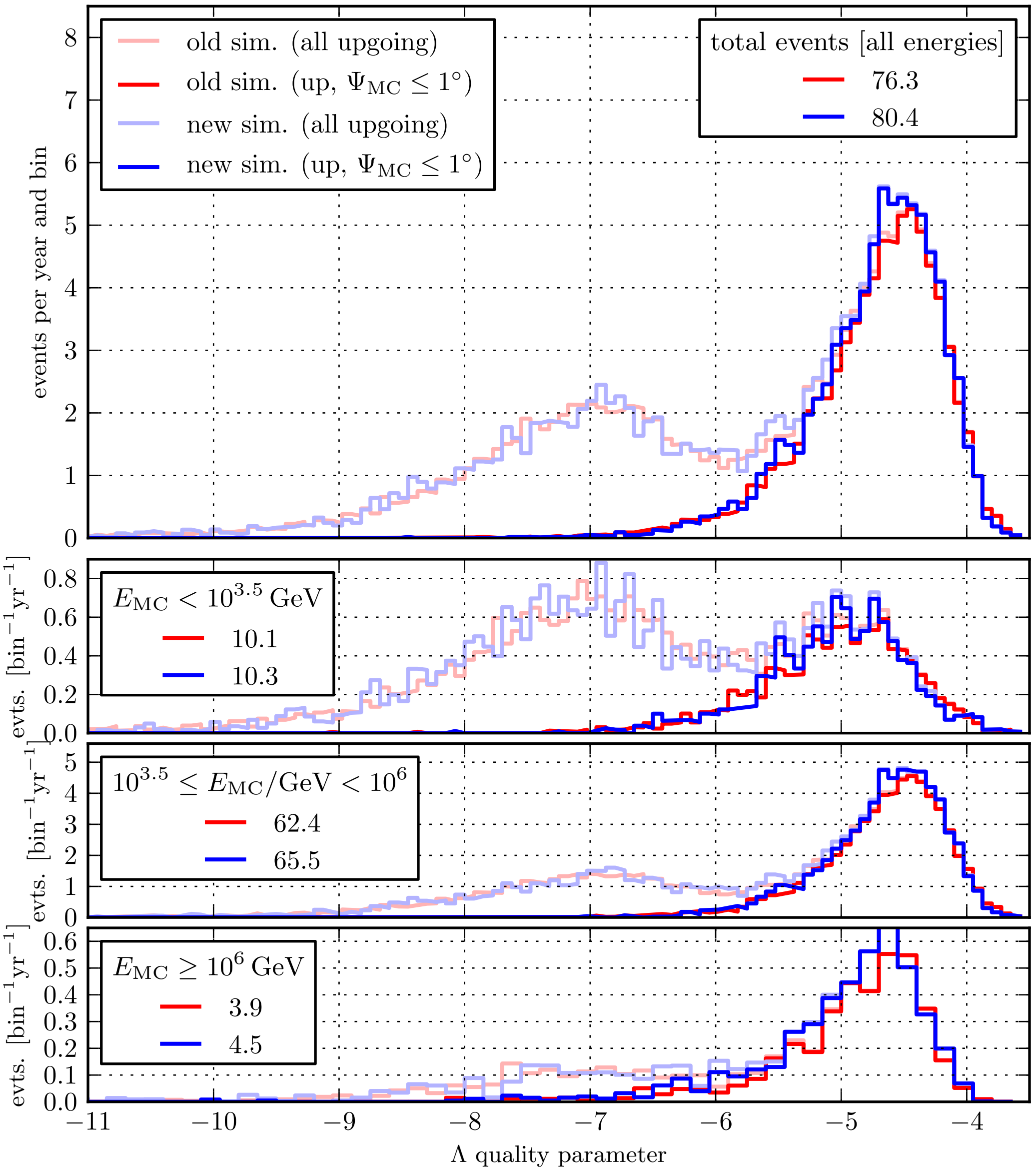

Figure 6.3 Distribution of the Λ quality parameter for both simulation chains. The top plot shows the overall distribution for an E^{-2} spectrum, whereas the lower plots show three different energy ranges. The lighter coloured lines correspond to the total distribution, the dark lines are distributions obtained after a cut on the Monte Carlo angular reconstruction error.

6.4 Angular resolution

Comparing the angular error of reconstructed tracks (cf. figure 6.4), the distributions are similar in shape and position. The only difference visible is an excess of well-reconstructed events for the new simulation. This is already expected from the previous plots, where more events were seen, too.

As expected, the highly optimised reconstruction algorithm yields an excellent angular resolution with a median angular error of about 0.07°. The cuts were optimised for best E^{-2} sensitivity, so some kind of energy estimator was needed to distinguish between the low energy atmospheric neutrino background and the high energy neutrinos from the signal flux. The cut chosen here (and in all following analyses) is the number of PMTs with L1 hits (N_{PMT}). This parameter depends on the track's energy due to the higher number of cascades from catastrophic energy losses accompanying them, leading to a higher photon count.

If optimising this cut together with the Λ quality parameter, the optimal values turn out to be $\Lambda \geq -5.5$ and $N_{\mathrm{PMT}} \geq 15$ for both simulation chains. When looking at the amount of mis-reconstructed events with $\Psi_{\mathrm{MC}} \gtrsim 1^\circ$, it is evident that these cuts are not probably enough to suppress the atmospheric muon background, although the plots were only made for upgoing events. Because of the immensely high rate of atmospheric muons, when compared to neutrino fluxes, having even a small amount of mis-reconstructed tracks with angular errors of the order of 90° or higher causes a large amount of atmospheric muon events to “spill over” below the horizon. Harder cuts will be needed to drastically lower the number of mis-reconstructed muons.

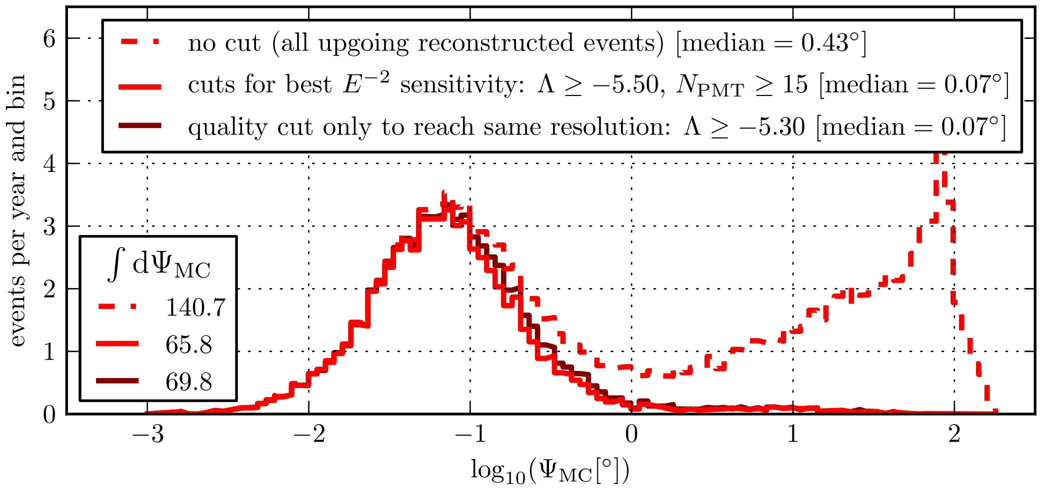

(a) old simulation chain

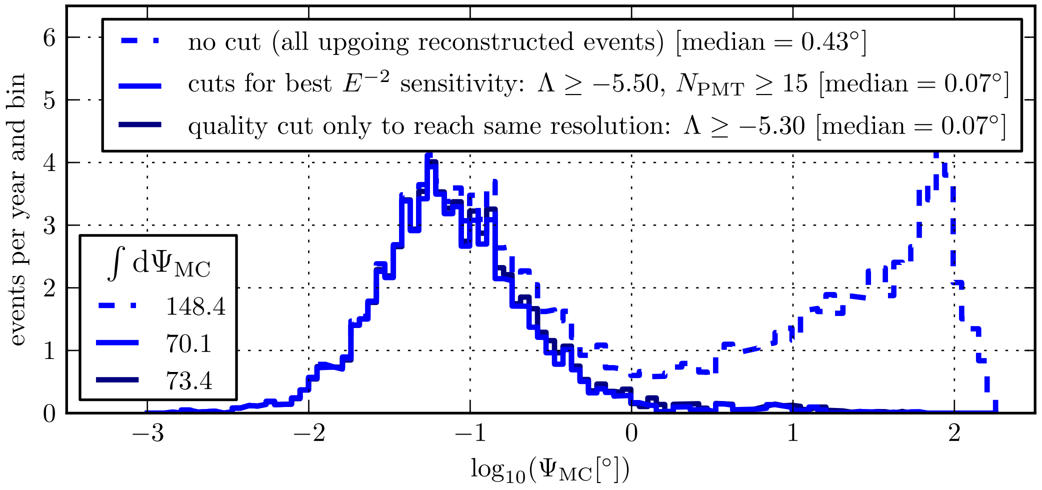

(b) new simulation chain

Figure 6.4 Angular error w.r.t. the muon direction for the old (a) and new (b) simulation chains, with no cut at all (i.e. all upgoing tracks that were reconstructable, without any quality cuts), with cuts optimised for best E^{-2} flux point-source sensitivity (using the Λ quality parameter and the number of PMTs with L1 hits, N_{PMT}, as a crude energy estimator) and with the Λ cut only. In the last case, the cut level was chosen as to obtain the same median resolution as for the combined Λ and N_{PMT} cuts.

6.5 Effective area

The effective areas for the two simulations (cf. figure 6.5) are similar, but show a peculiar behaviour at high energies ($E_{\mathrm{MC}} \gtrsim 10^6\,\mathrm{GeV}$): the effective area for reconstructed events does not follow the shape of the area obtained when asking for reconstructible events — for the ANTARES reconstruction strategy, this corresponds to $N_{\mathrm{hits}} \geq 6$, where N_{hits} is the number of hits selected for the final reconstruction step. Instead, the ratio of the two areas gets smaller again. This is due to the distribution of the Λ parameter at this energy range, which is broader than for lower energies. A constant cut on Λ thus removes more and more muons with well reconstructed tracks, thereby reducing the effective area. This difference can thus be attributed to the reconstruction strategy which was never designed for these high-energy events in km^3-scale detectors. The differences at very low energies ($E_\nu < 10^3\,\mathrm{GeV}$) can be attributed to a lack of statistics. In this region, over 95% of all simulated events are removed by the quality cuts, thus leaving only a small amount of samples to determine the effective area[3]. This, combined with the fact that the simulated spectrum is E^{-1} in both cases and thus produces lower statistics at low energies anyway, can very well lead to the observed differences.

---

[3] In the energy range $10^3\,\mathrm{GeV} \leq E_\nu \leq 10^6\,\mathrm{GeV}$ only about 50% of the simulated events are removed.

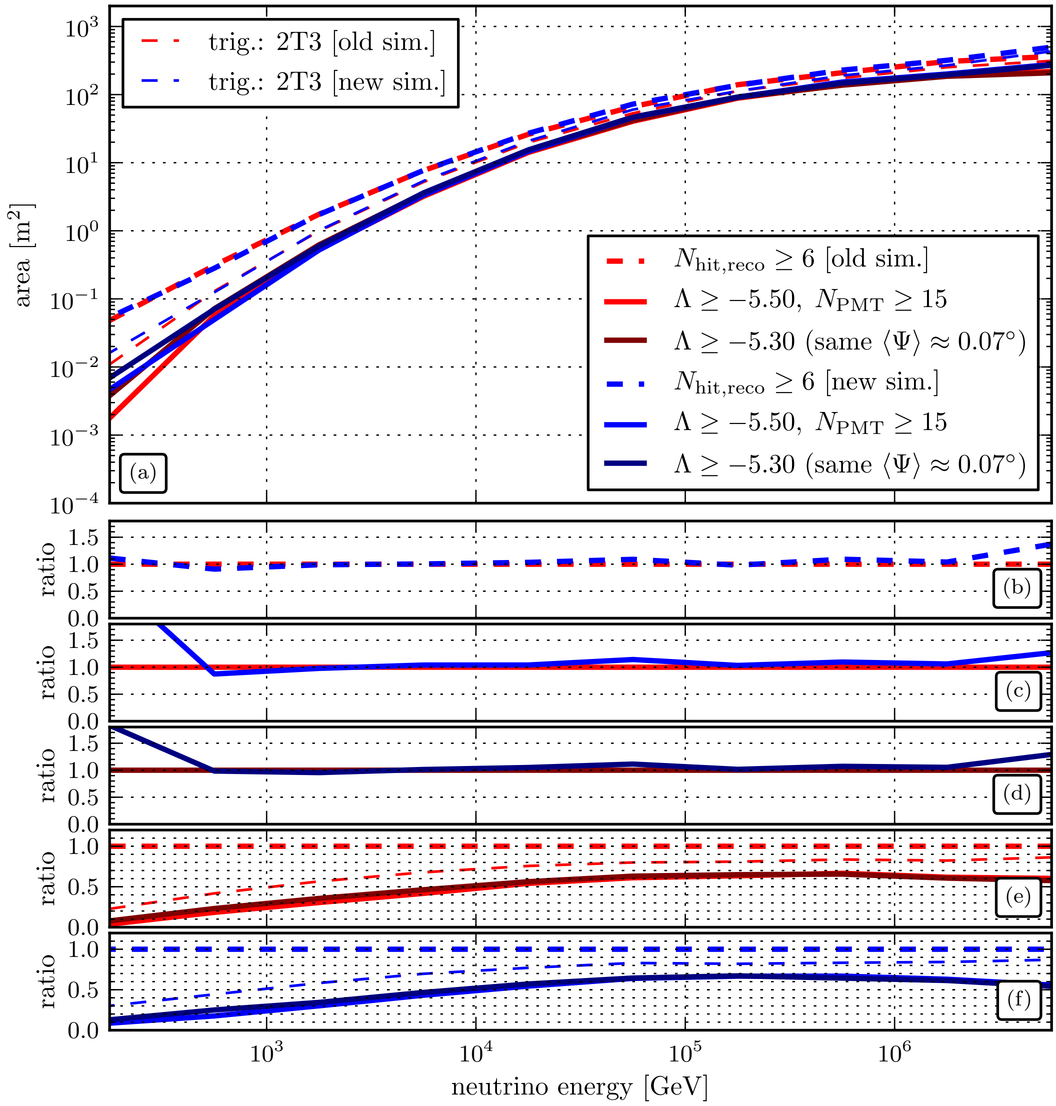

Figure 6.5 The top plot (a) shows the neutrino effective area for the two simulation chains for three different cut levels: all tracks that have at least 6 hits for the final reconstruction step (dashed), all hits surviving the cuts for best E^{-2} sensitivity and all hits for a cut yielding the same median angular resolution as the sensitivity cut, but using only the Λ parameter. For comparison, the effective areas for the 2T3 trigger level have been included. The lower plots (b-f) show ratios of the effective areas using the same colour scheme as in the top plot. Note that no trigger is used during the actual reconstruction.

6.6 Point-source sensitivity

The point-source sensitivity for an E^{-2} flux at different declinations δ (cf. figure 6.6) reveals differences between the two simulations at the extreme declination values corresponding to almost horizontal tracks ($\delta \gtrsim 20°$). The sensitivity calculated from the new simulation chain is slightly better over the whole range of declinations, except for declinations $\delta \lesssim -60°$. This corresponds to upgoing tracks, where very high neutrino energies cannot contribute due to their absorption in the earth. The difference is therefore due to neutrinos with very high energies of the order of $E_\nu \approx 10^6\,\mathrm{GeV}$ or higher. The flux of these neutrinos can influence the sensitivity as the simulated E^{-2} spectrum does not have any cutoff at high energies (except for the one imposed by the simulation which stops at $E_\nu = 10^7\,\mathrm{GeV}$). When plotting the sensitivity as a function of zenith angle in the detector's local system instead of declination (cf. figure 6.7), the effect gets disentangled from the declination "smearing" due to the Earth's rotation: starting from upgoing tracks at a zenith angle of 180° to about 120°, the sensitivities from both simulation chains are compatible. Only at zenith angles near the horizon, where neutrinos of extremely high energies can contribute because of their shorter path through the earth, the two sensitivities begin to deviate. This is compatible with the previous observation that an excess of events is observed at higher energies with the new simulation chain when compared to the old chain.

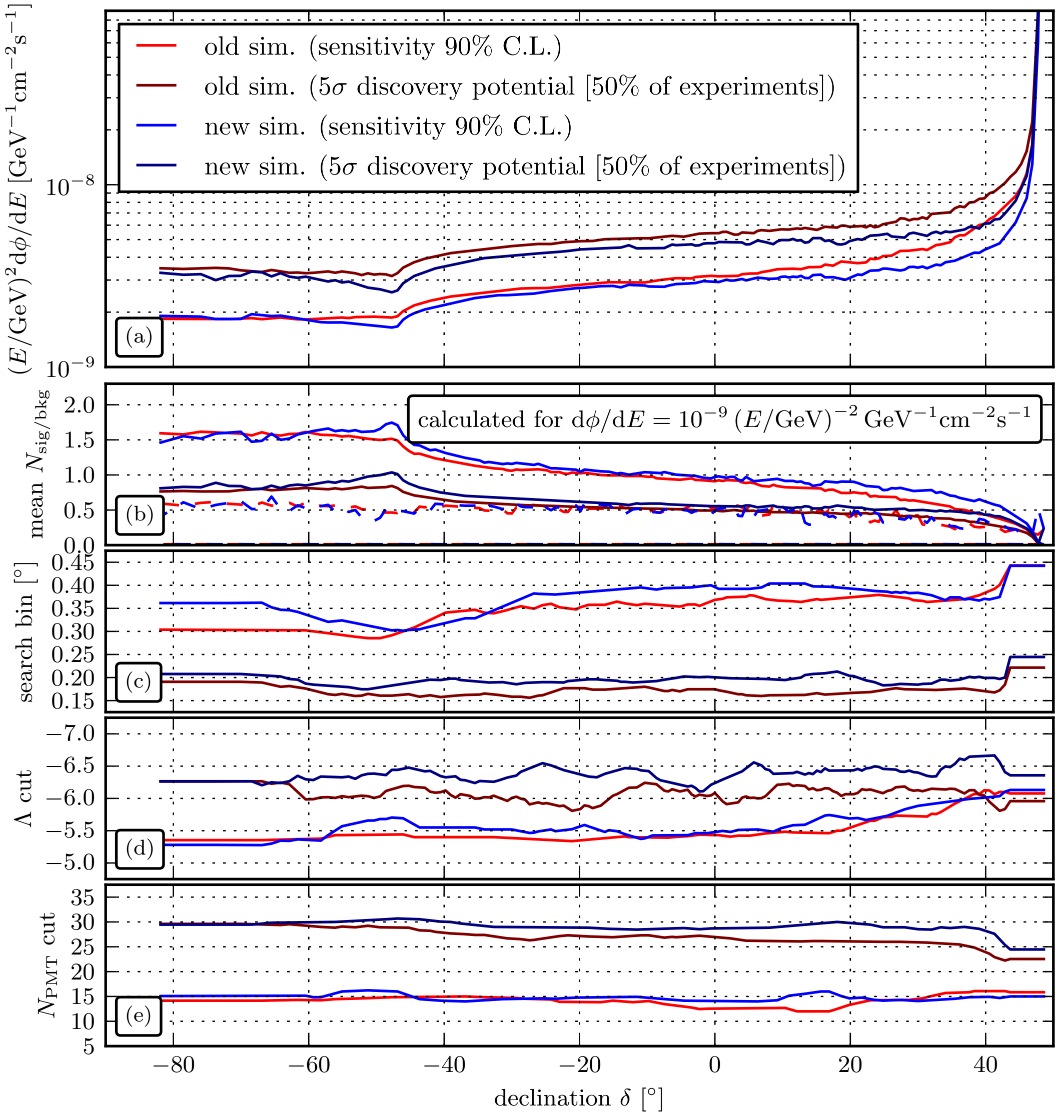

Figure 6.6 Point-source sensitivity and discovery potential for one year for the old and new simulation chains. The top plot (a) shows the final detectable/excludable fluxes, whereas the lower plots show the individual cut levels (c-e) and the mean number of signal and background events per year (b). The number of background events is indicated using a dashed line in (b). The search bin size in (c) is given as the radius. As the correlation between the parameters in (c-d) is high and their behaviour can therefore be erratic, the values have been smoothed using a sliding window to better indicate the parameters' general behaviour.

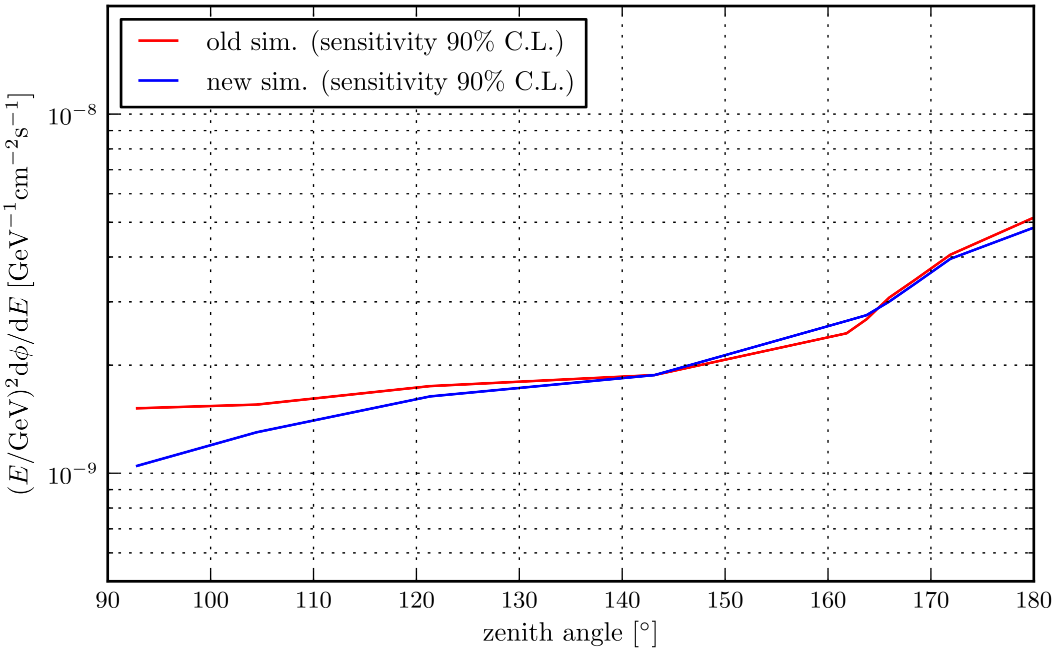

Figure 6.7 Point-source sensitivity for one year plotted against zenith angle. Plotting the sensitivity in this way corresponds to moving the detector to the pole, where zenith angle and declination have a time-independent relationship to each other.

7 Performance of different detector designs

> It is common sense to take a method and try it. If it fails, admit it frankly and try another. But above all, try something.
>
> *(Franklin D. Roosevelt)*

In this chapter, the three different detector types introduced earlier in section 2.3.2 will be compared. The detector sizes are still "small", i.e. 154 strings for the "string" and "multiPMT" designs and 80 strings for the "tower" design. The string distance for the former two detectors is 91 m, whereas it is 130 m for the latter. This choice yields approximately the same photocathode area for each of the designs, while still retaining a hexagonal layout and approximately the same detector volume and thus makes them comparable. This choice was made because the sensitivity of neutrino detectors mainly scales with photocathode area [78]. In this way, the designs' performance can be disentangled from the effect achieved by simply adding more OMs. Note that the average cost per optical module may be different for each design.

From now on, all simulations were made using the new simulation chain developed in this work. The input tracks used for all detectors are exactly the same, i.e. the same ANIS run is used for all of them. The only difference is in the muon tracking and light propagation step, which uses a different random seed for each detector type, and in the PMT and OM simulations. As before, the optical noise level for the single-PMT designs was chosen to be 75 kHz per OM. This translates to a background rate of 5.2 kHz per PMT for the "multiPMT" design. This value has been determined using a dedicated photon tracking simulation taking into account all of the OM parameters given in section 4.9.2.[1]

All data simulated for the "tower" and "string" detectors were reconstructed using the standard ANTARES reconstruction strategy, whereas for the "multiPMT" design, the new reconstruction algorithm presented in section 4.11.2 was used.

---

[1] The simulation was set-up in such a way as to retain the value of 75 kHz when applied to the single-PMT OMs.

7.1 Angular resolution

As in the previous chapter, the cut levels have been optimised for best E^{-2} point-source sensitivity. As expected, the angular resolution determined for the “string” design is almost the same as the one shown in the previous chapter (cf. figure 7.1(a)). There is only a single parameter that has been changed, which is the inclusion of light from the hadronic cascade at the interaction vertex. Interestingly, this change leads to a slight drop in the median angular resolution from 0.07° to 0.08° when reconstructing exactly the same events.

As expected, the angular resolution determined for the “multiPMT” design is worse than that of the other two designs (cf. figure 7.1(c)). This, however, is not due to the detector’s inferior design, but rather due to the fact that the reconstruction algorithm used for this type of detector is not as refined as the standard ANTARES strategy. Large improvements in both detection efficiency and angular resolution can be expected once the new algorithm gets more refined. For the other two detector types, where the algorithm is already heavily adapted to single-PMT light detection in sea-water only smaller improvements are expected when optimising the reconstruction algorithm. In this way, all results presented for the “multiPMT” design are to be taken as worst-case scenarios, where no optimisation has been done on the reconstruction algorithm.

The “tower” design has a good angular resolution but the detection efficiency is worse than that of the “string” design. This seems to be due to the sparser detector which allows more muons to pass it undetected. If, however, the cost of deploying one tower structure is not much more expensive than the cost of deploying a single string, a denser “tower” detector with more OMs will certainly outperform a “string”-type detector of similar cost.

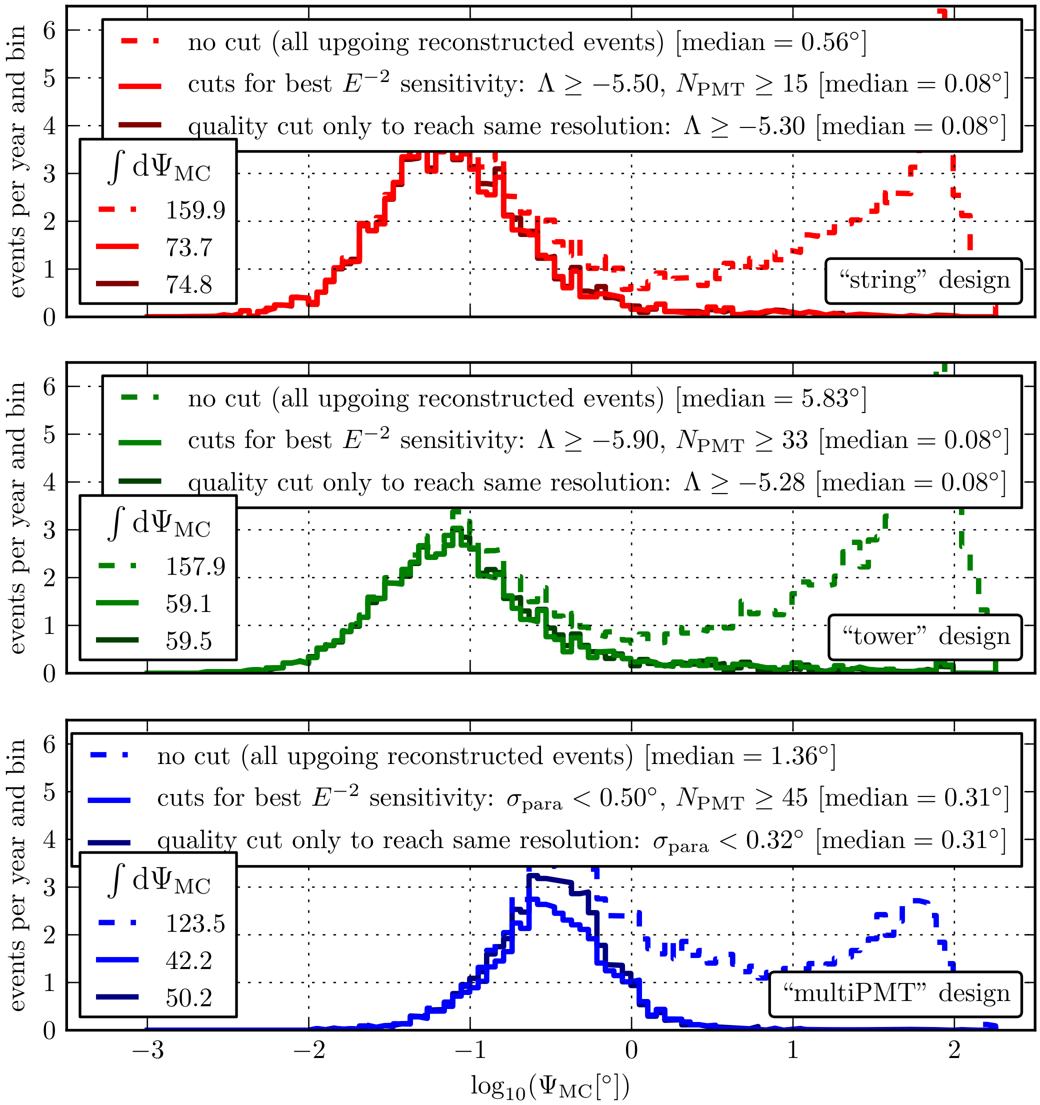

Figure 7.1 Angular error w.r.t. the muon direction for the "string" (a), the "tower" (b) and the "multiPMT" (c) designs, with no cut (i.e. all upgoing tracks that were reconstructable, without any quality cuts), with cuts optimised for best E^{-2} flux point-source sensitivity (using the Λ quality parameter and the number of PMTs with L1 hits N_{PMT} as a crude energy estimator) and with the Λ cut only. In the last case, the cut level was chosen to obtain the same median resolution as for the E^{-2} cuts.

7.2 Effective area

When comparing the effective areas of the three detector designs shown in figure 7.2, it is apparent that the effective area obtained for the “multiPMT” design is a factor 0.3 smaller than the one for the “string” design. This is visible over the whole range of energies for the case where no additional energy cut was introduced in addition to the fit quality cut (Λ for the single-PMT designs and σ_{para} for the “multiPMT” design). To achieve the best E^{-2} point-source sensitivity, the “multiPMT” design with its worse angular resolution due to the unoptimised reconstruction algorithm needs a high energy cut. This can be seen at energies $E_\nu < 10^4\,\text{GeV}$ (lighter colours). This cut could have been chosen at a lower level if the angular resolution had been better.

Interestingly, the drop in effective area at very high energies visible for tracks reconstructed with the ANTARES algorithm is not visible for the “multiPMT” detectors using a different algorithm. This backs up the point made before that this drop is an artefact of the ANTARES track reconstruction algorithm.

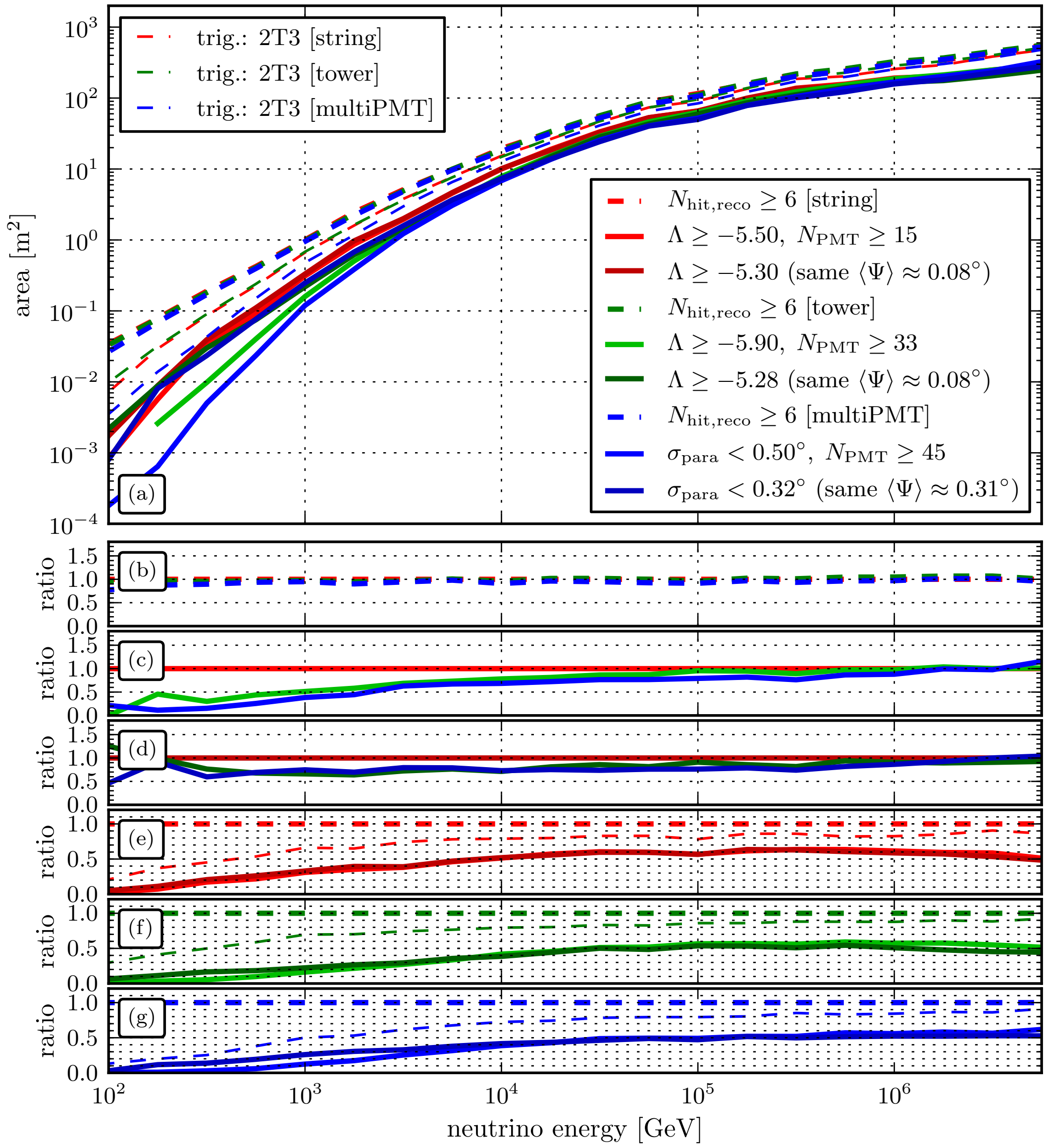

Figure 7.2 The top plot (a) shows the neutrino effective area for the “string”, “tower” and “multiPMT” detector designs with three different cut levels: all tracks that have at least 6 hits for the final reconstruction step (dashed), all hits surviving the cuts for best E^{-2} sensitivity and all hits for a cut yielding the same median angular resolution as the sensitivity cut, but using only the Λ/σ quality parameter. The lower plots (b-g) show ratios of the of the effective areas using the same colour scheme as in the top plot. Note that no trigger is used during the actual reconstruction.

7.3 Point-source sensitivity

It is no surprise that the point-source sensitivity for an E^{-2} flux is worse for the “multiPMT” design than for the two other detector types. This is due to the slightly worse effective area and to the worse angular resolution obtained with the unrefined reconstruction algorithm. Figure 7.3 shows the point-source sensitivity and the discovery potential for the “multiPMT”, “tower” and “string” detector designs along with the cut levels, search bin sizes and event numbers that are used to calculate these values. Despite the comparable effective areas of the “multiPMT” ad “tower” designs, the “tower” design has a better senistivity due to its better angular resolution.

7.4 Effect of the atmospheric muon background on the multiPMT design

Up to now, no atmospheric muon background was included in the sensitivity studies. The reason for this is the immense computational time needed to simulated a sample with adequate statistics. For point-source studies where the detector is looking below the horizon, only mis-reconstructed atmospheric muons surviving the quality cuts are of interest. As the atmospheric muon flux is a factor of 10^6 higher than the atmospheric neutrino flux, it is very time-consuming to generate such a sample for each detector design with the appropriate statistics. Unfortunately, this time was not available during this study.

For this reason, a different approach was taken: a number of atmospheric muon events was generated for the “multiPMT” design, as this is the design choice that will be further explored in the remainder of this work. For two example reconstruction quality cut levels, the minimum energy cut level needed in order to suppress the atmospheric muon background to a level of 10% of the atmospheric neutrino background was determined. The assumption made here is that when this level is reached, the atmospheric muon background can effectively be neglected. As with the previous results, the energy cut was performed by requiring a minimum number of PMTs with at least one L1 hit N_{PMT}.

Because the simulated atmospheric muon sample did not have the necessary statistics, an extrapolation to the 10% level was performed. The results can be seen in figure 7.4(a). In this case, the reconstruction quality cut was fixed to $\sigma_{\text{para}} = 0.55$, which is the approximate cut value yielded by the E^{-2} sensitivity optimisations. When increasing the N_{PMT} cut, the number of mis-reconstructed atmospheric muon events is falling faster than the number of atmospheric neutrino background events. Unfortunately, at $N_{\text{PMT}} \approx 43$, all of the simulated atmospheric muon events are cut away. At this point, this background type is still a magnitude higher than the neutrino background. However, when linearly extrapolating the curve, it can be seen

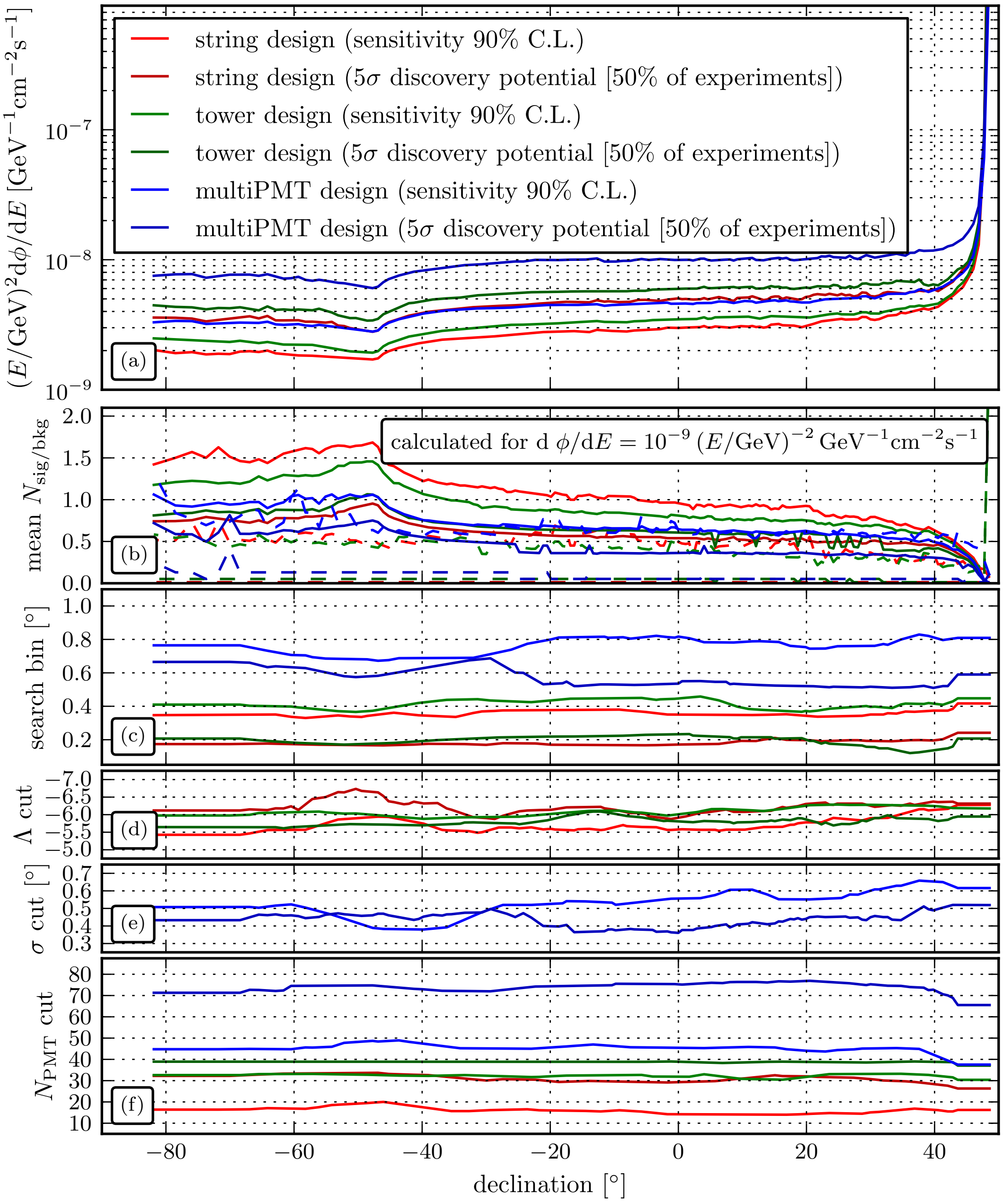

Figure 7.3 Point-source sensitivity and discovery potential for one year for the "string", "tower" and "multiPMT" design options. The top plot (a) shows the final detectable/excludable fluxes, the lower one the individual cut levels (c-f) and the mean number of signal and background events (b). The number of background events is indicated using a dashed line in (b).

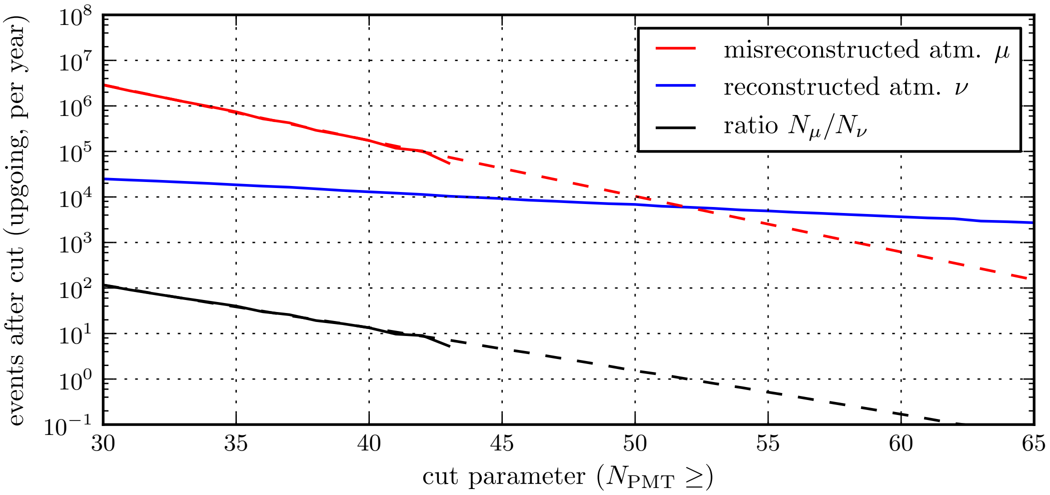

(a) loose cut $\sigma_{\mathrm{para}} = 0.55$

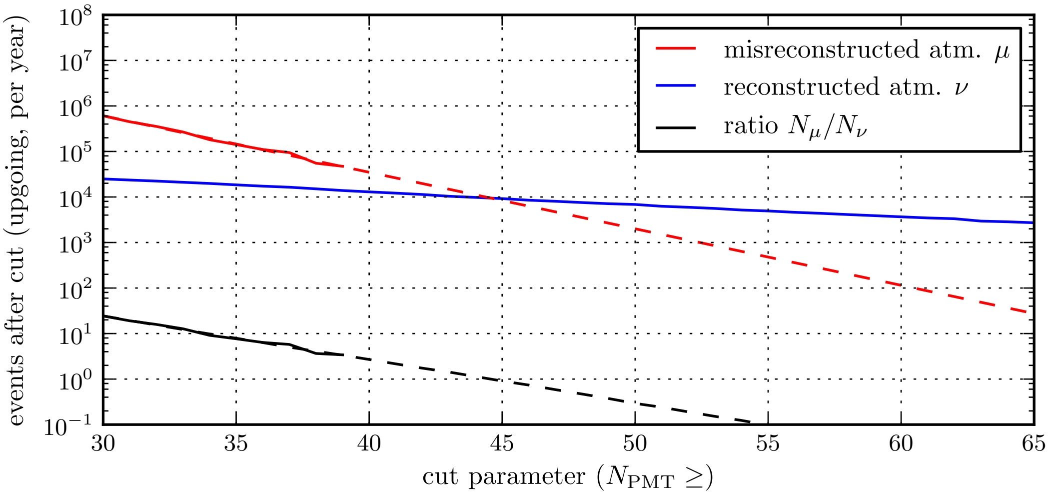

(b) tight cut $\sigma_{\mathrm{para}} = 0.3$

Figure 7.4 Extrapolation of the N_{PMT} energy cut to a level where the atmospheric muon background is 10% of the atmospheric neutrino background. The upper plot (a) uses a looser track quality cut, requiring a higher number of hit PMTs in order to suppress enough atmospheric muons. In the lower plot (b), a tighter quality cut was chosen, yielding a lower N_{PMT} requirement.

that the 10% level is reached at $N_{\mathrm{PMT}} \geq 62$. Thus, assuming the dependence stays linear until this point, the necessary cut level is found. This energy cut is rather high when compared to the necessary N_{PMT} level determined by the previous sensitivity optimisations of about $N_{\mathrm{PMT}} \gtrsim 45$. It is, however, lower than the cutoff provided by an optimisation for best discovery potential. Thus, when tightening the energy cut to the determined level, the point-source sensitivity will get slightly worse, whereas the discovery potential will stay virtually unchanged. This behaviour can be seen in figure 7.5.

A second N_{PMT} cut level was determined for a tighter reconstruction quality cut of $\sigma_{\mathrm{para}} = 0.3$. The reason for this is, that the previous energy cut may certainly be usable for source spectra which extend up to very high energies (like the pure E^{-2} benchmark spectrum used up to now), but is not especially suited for spectra with a lower energy cutoff, where very high energy neutrinos are not emitted. Choosing a tighter reconstruction quality cut will lead to a lower energy cutoff that retains more of the events from a particular source. The results can be seen in figure 7.4(b). The energy cut level is now $N_{\mathrm{PMT}} \geq 55$. This "low-energy" cut will be used later on during the determination of discovery potentials for a real source (RX J1713.7–3946) instead of the pure E^{-2} spectrum (see section 8.2.4).

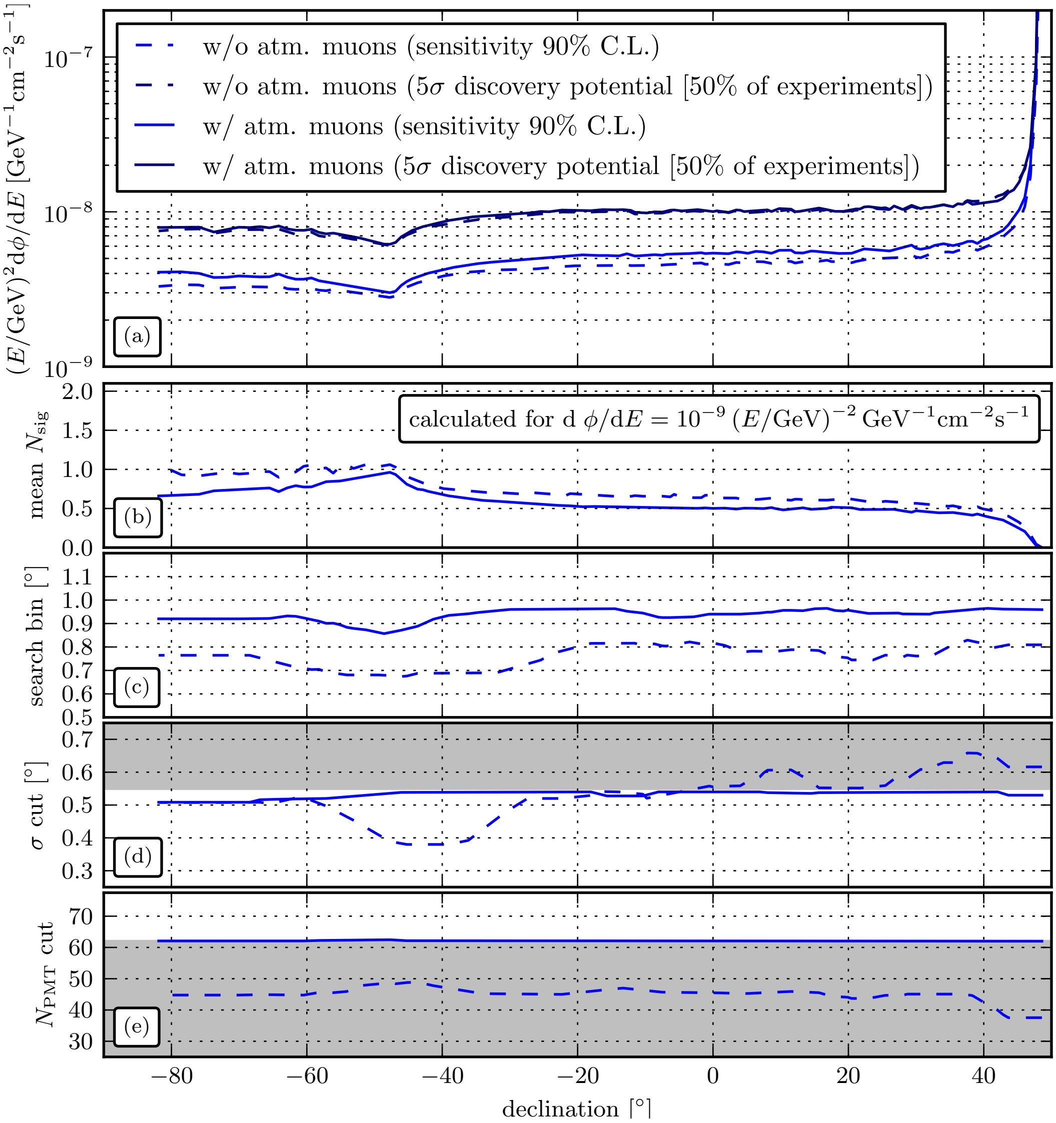

Figure 7.5 The top plot (a) shows the point-source sensitivity and discovery potential for one year for the "multiPMT" design with 154 strings with and without the constraints derived for the reduction of the mis-reconstructed atmospheric muon background The lower plots (b-e) show the individual cut levels and the mean number of signal and background events per year. The grey bands are the areas that are excluded by the constraints. As the cuts for the discovery potential are almost always outside these constraints, they are omitted from the plots.

8 Scaling of the multiPMT design

> Two is not equal to three -
> not even for very large
> values of two.
>
> *(Grabel's Law)*

The remainder of this work shall focus on the "multiPMT" detector design and explore the effects of varying the number of string and the inter-string distance.

8.1 Doubling the number of strings

An interesting question to ask is: how does the sensitivity of a detector behave when increasing the number of strings? This section will explore part of this question by looking at the effects of doubling the number of strings of the previous detector design from 154 strings to 308 (or 310) strings. When not changing the layout of each single string and keeping the string distance constant, the number of strings can be doubled in two ways. One possibility is to simply build two identical detectors at two separate sites, so that the chance of observing the same event in two detectors becomes negligible. In this case, no new simulation is necessary to determine the sensitivity or discovery potential as the detectors are fully independent. The observed numbers of background and signal events can simply be doubled. The other possibility is to build a single, larger detector with twice the number of strings. Such a detector has been simulated, however with 310 instead of 308 strings. The reason for this is that a hexagonal seafloor string layout is only possible with 310 strings and not with 308. The systematical error introduced by this is negligible.

Figures 8.1 and 8.2 shows the E^{-2} point-source sensitivities and discovery potentials for both cases, respectively. For the chosen benchmark flux, there is almost no difference between a single, large or two smaller detectors. When looking at the discovery potential for a E^{-2} point-source flux, it even seems to be better to build two smaller detectors. Note that the atmospheric muon constraints derived in section 7.4 have been imposed on the sensitivity and discovery potential calculations. Also note that the N_{PMT} cut derived for the 154-string detector is assumed to also be valid for the 310-string version, as, unfortunately, a new atmospheric muon simu-

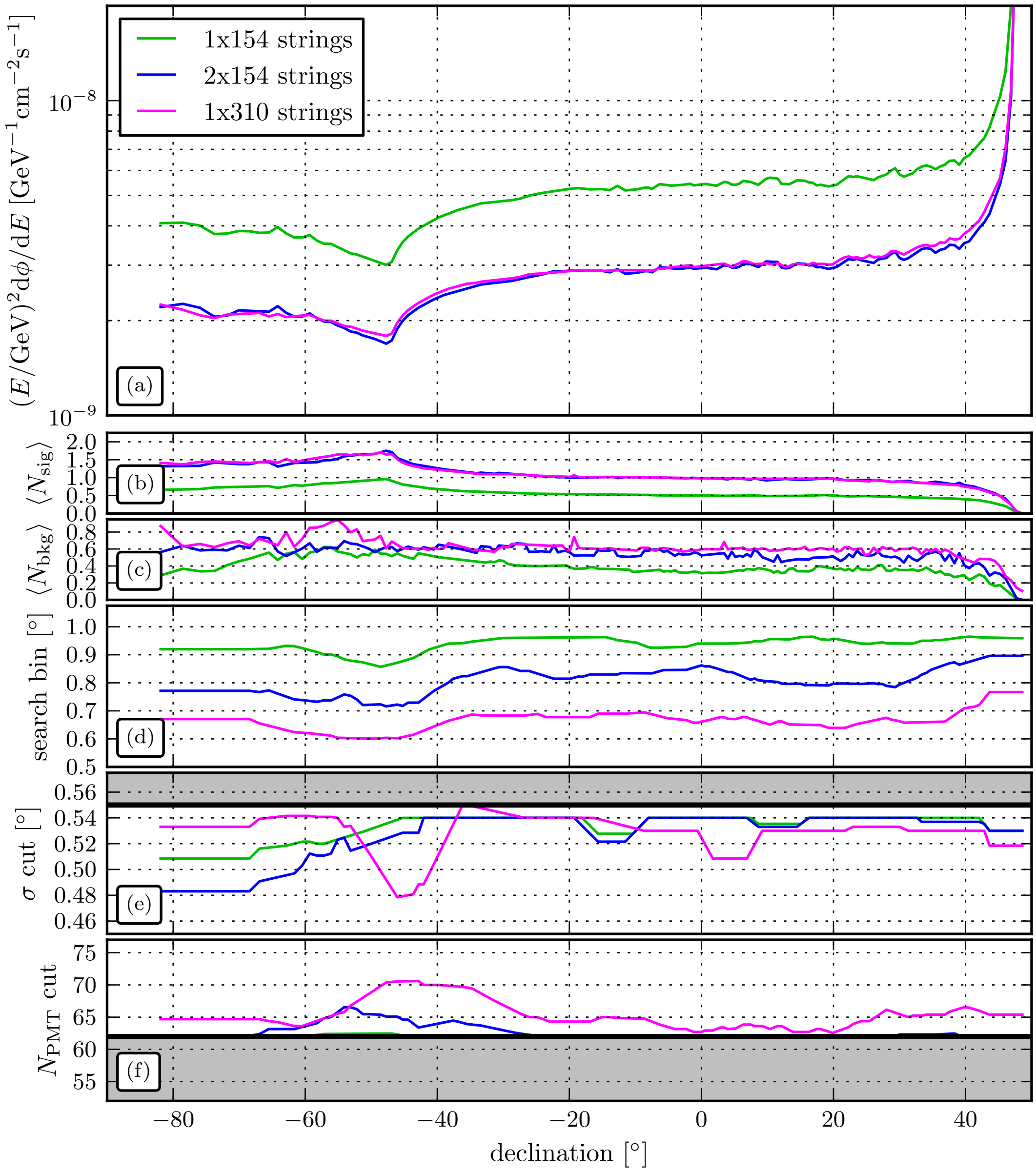

Figure 8.1 Point-source sensitivity (90% C.L.) for one year for the "multiPMT" design with 154 strings, 2x154 strings and 310 strings. The top plot (a) shows the final detectable/excludable fluxes, whereas the lower plots (b-f) show the individual cut levels and the mean number of signal and background events per year. The grey bands represent the atmospheric muon constraints imposed on the cut levels.

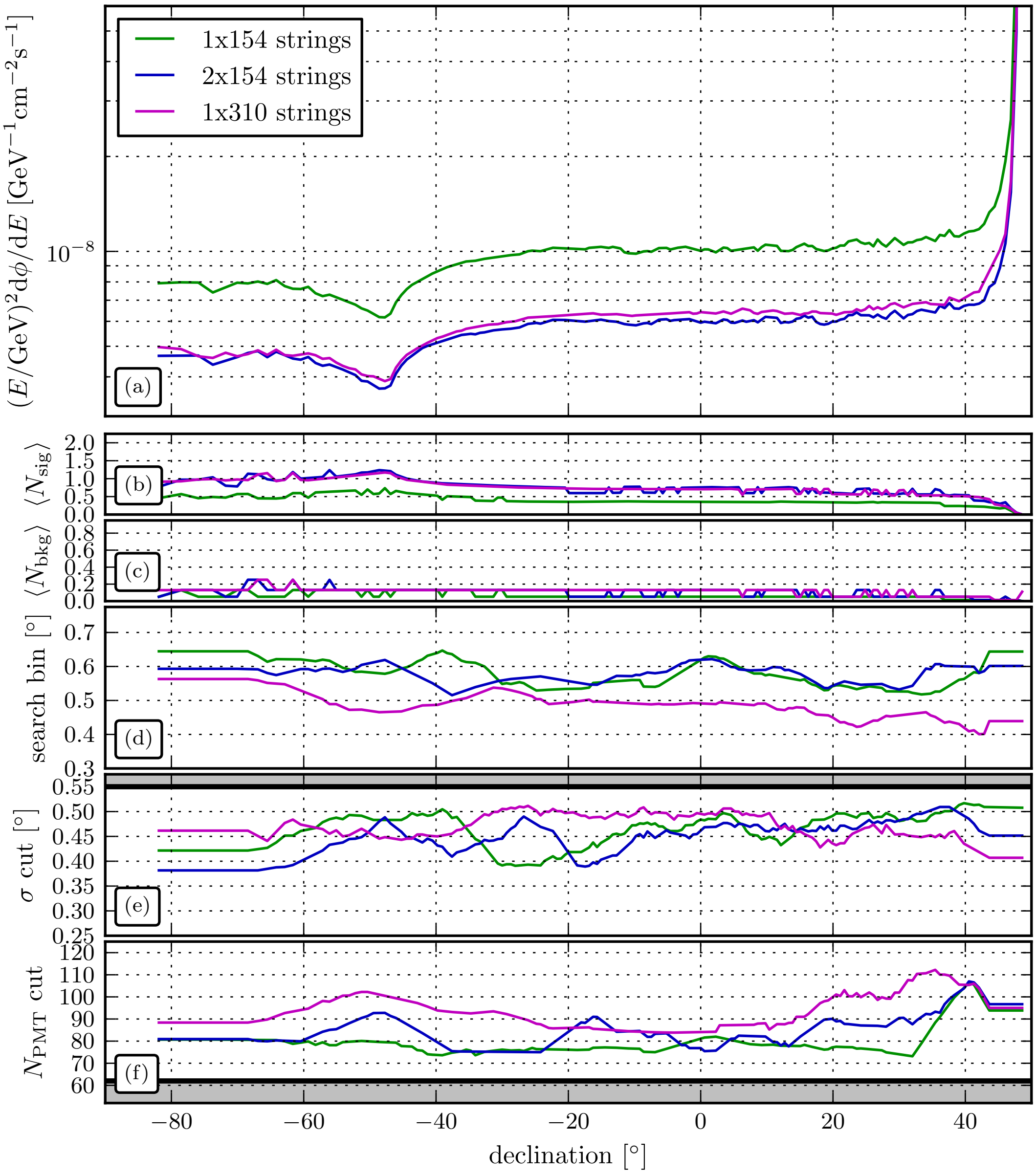

Figure 8.2 Point-source 5σ discovery potential for 50% of experiments in one year for the "multiPMT" design with 154 strings, 2x154 strings and 310 strings. The top plot (a) shows the final detectable/excludable fluxes, whereas the lower plots (b-f) show the individual cut levels and the mean number of signal and background events per year. The grey bands represent the atmospheric muon constraints imposed on the cut levels.

lation could not be performed for this detector type due to the required generation time.[1]

This is, however, an effect of the unbroken E^{-2} benchmark spectrum. Here, very high energy neutrinos play an important role. As the generated muons have very long tracks, the “effective” volume for such tracks is larger when building two independent detectors. In a way, at very high energies, the detector becomes “surface”-dominated instead of “volume”-dominated. Thus, when introducing an energy cutoff E_{cut} into the benchmark spectrum, the single, large detector should perform better starting at a certain cutoff. This is shown in figure 8.3(b). The benchmark spectrum was changed to include a cutoff term to look like

$$\frac{\mathrm{d}\phi_{\nu_\mu}}{\mathrm{d}E} := 10^{-8}\left(\frac{E}{\mathrm{GeV}}\right)^{-2}\exp\left(-\sqrt{\frac{E}{E_{\mathrm{cut}}}}\right)\mathrm{GeV}^{-1}\mathrm{cm}^{-2}\mathrm{s}^{-1}. \tag{8.1}$$

Example spectra are shown in figure 8.3(a). Note that no neutrinos were simulated above $E_\nu = 10^7\,\mathrm{GeV}$, which also represents a hard cutoff. This energy region is marked with a grey background in figure 8.3(a). When varying E_{cut}, it can be seen that a single, large detector starts to yield better sensitivities for $E_{\mathrm{cut}} \lesssim 10^7\,\mathrm{GeV}$. For $E_{\mathrm{cut}} \lesssim 10^5\,\mathrm{GeV}$, the discovery potential obtained for a single, large detector becomes better than the one for two smaller detectors, as well.

This result raises an important issue when optimising detector designs for pure E^{-2} point-source fluxes. Real neutrino sources will always have an energy cutoff at a certain point, so that a single-minded optimisation for this benchmark source spectrum may yield a different optimal detector design than what would be obtained for more realistic spectra. When building a neutrino detector, it will always be more suited to one type of spectrum than to another. The expected spectra from Galactic sources, e.g. SNRs, show lower cutoffs, while the spectra from extragalactic sources like GRBs have higher ones. It is thus important not only to optimise for one extreme case, like a pure E^{-2} spectrum, and to keep in mind that other source spectra should be detectable after a practical amount of observation time, too.

---

[1] In the rather “flat” detector designs looked at here, with heights of 570 m compared to diameters of over 1 km, downgoing, low-energy muons should only hit a low number of strings, anyway. This number will not change significantly when adding more strings while leaving the detector height constant.

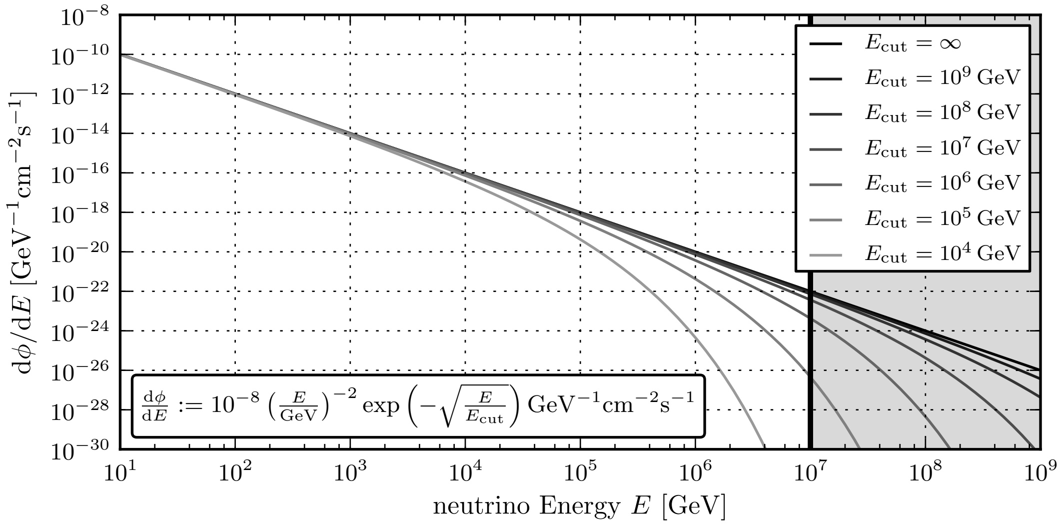

(a) E^{-2} fluxes with energy cutoffs

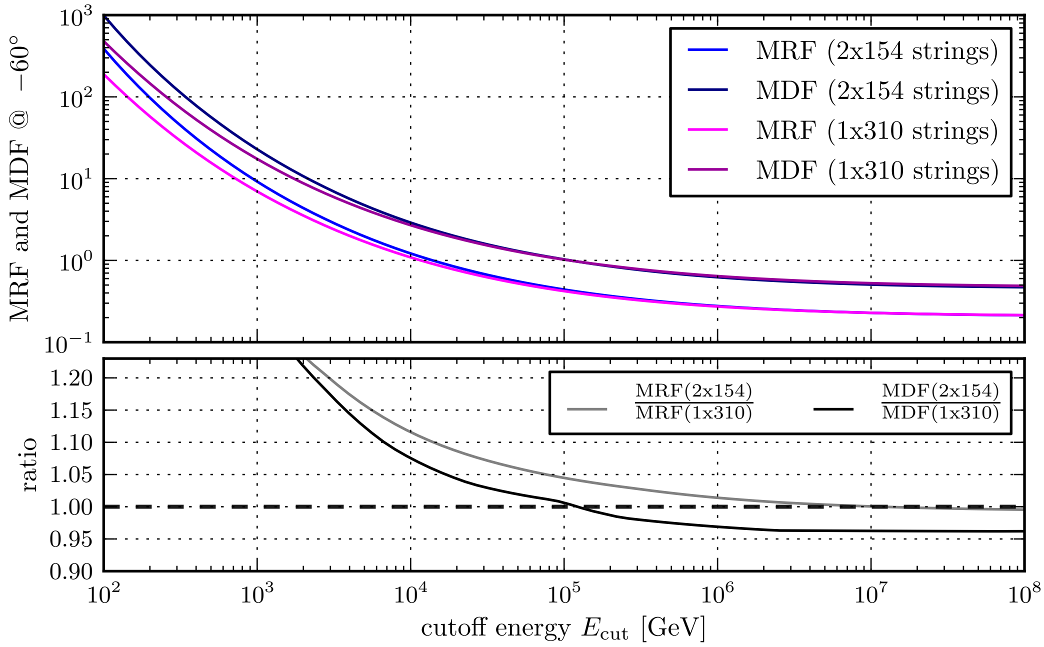

(b) model discovery and rejection factors vs. E_{cut}

Figure 8.3 Behaviour of the sensitivity and discovery potential on an energy cutoff in the source neutrino flux for a source at $\delta \approx -60°$. The upper plot (a) shows the simulated spectra used to calculate the MRF and MDF values shown in (b).

8.2 Effects of varying string distances

In this section, the effects of increasing the string distance from 91 m to larger distances is explored for a “multiPMT” detector with 310 strings. For historical reasons, these distances were chosen to be 100 m, 130 m and 150 m. As before, for each of these distances, the angular resolution and effective areas have been determined using cut values from a sensitivity optimisation to an E^{-2} point-source flux. The atmospheric muon cuts derived in section 7.4 are also used for these calculations.

8.2.1 Angular resolution

The angular reconstruction errors for each of the simulated detectors is shown in figure 8.4. Not surprisingly, the median angular error get slightly worse with increasing string distance, starting at 0.28° for 91 m up to 0.35° for 150 m string distance. The lower amount of light reaching the OMs in a less dense detector and the increased timing error for long photon paths introduce a higher uncertainty when reconstructing a muon track.

8.2.2 Effective area

Comparing the effective areas obtained for the four different distances, the expected behaviour can be observed: at low energies, short string distances are advantageous, because muon tracks will be short and do not emit a large amount of light. In contrast, at higher energies, the amount of light produced by a muon track will be enough to illuminate a sufficient amount of optical modules, even if they are far away from a light source. Hence, the string spacing does not have to be as small as for low energies.

The effective areas plotted against neutrino energy seen in figure 8.5 show exactly this behaviour. At about $E_\nu \approx 2 \cdot 10^4\,\mathrm{GeV}$, the effective area is independent from the string spacing. For lower energies, smaller string distances are favourable, above this point, higher string distances yield better effective areas. The objective is to find a string distance that finds the best balances between both.

8.2.3 Point-source sensitivity

Detectors with large string distances seem to be better suited for the detection of an E^{-2} point-source flux, as can be seen in figures 8.6 and 8.7. Especially at declinations where near-horizontal high-energy neutrinos play a larger role, the sensitivity becomes better when the string distance is increased. At declinations near $-90°$, corresponding to up-going tracks where extremely high-energy neutrinos are absorbed by the Earth, these differences are less pronounced.

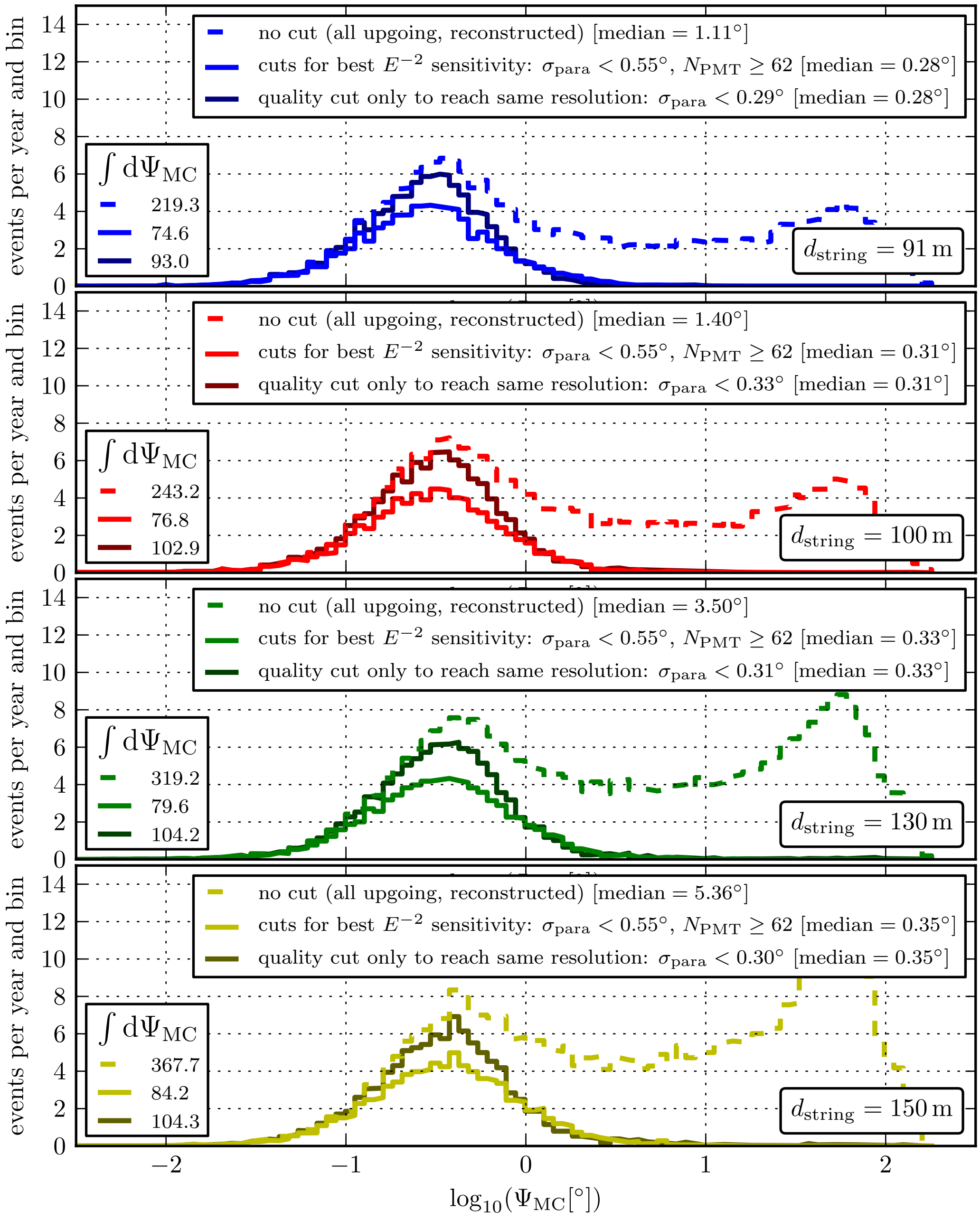

Figure 8.4 Distribution of angular reconstruction errors w.r.t. the muon direction for four 310-string "multiPMT"-type detectors with varying string distances. The subplot contents are analogous to the plots shown on the previous pages.

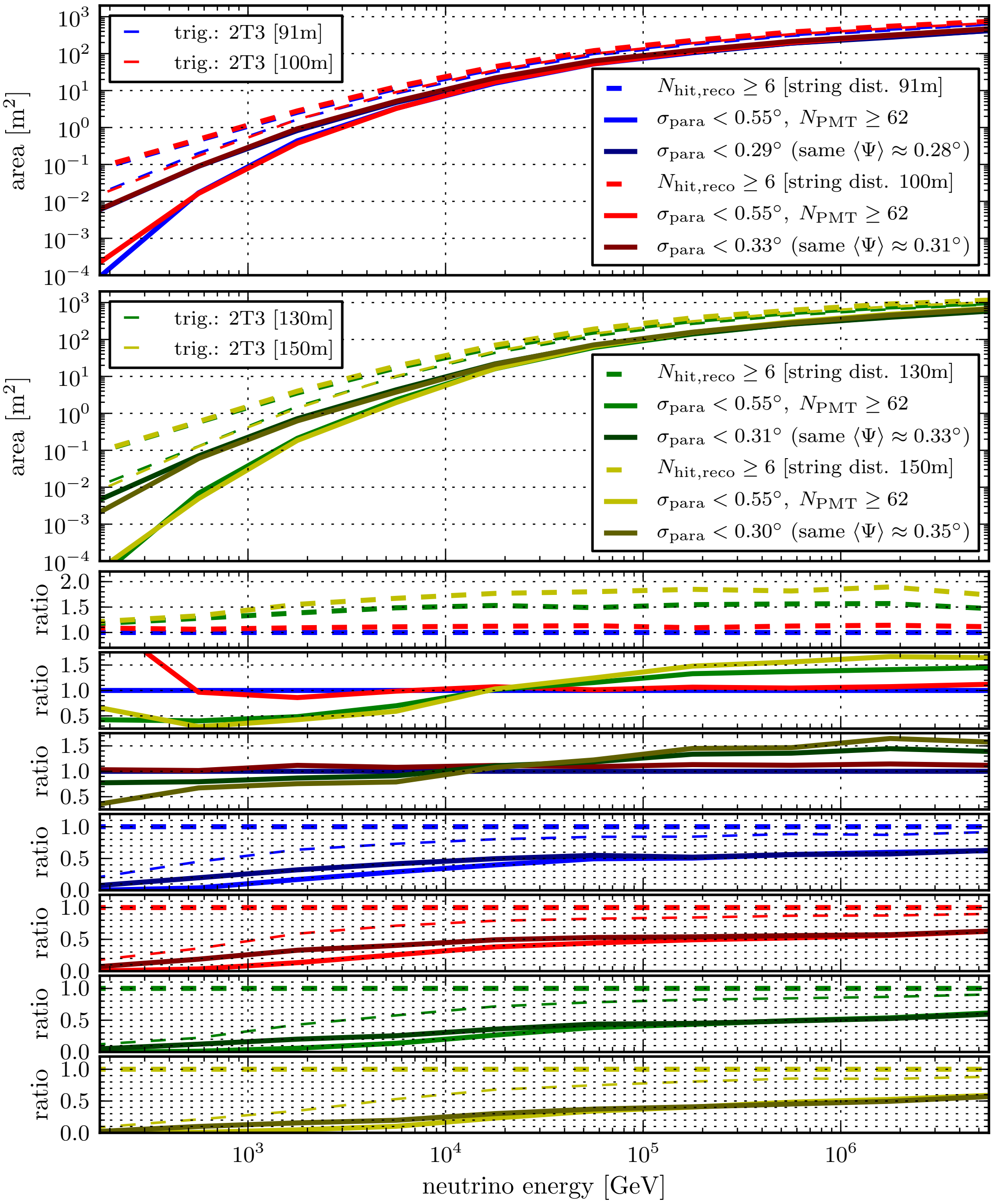

Figure 8.5 Effective area for 310-string “multiPMT” detectors with four different string distances. The subplot contents are analogous to the plots shown on the previous pages.

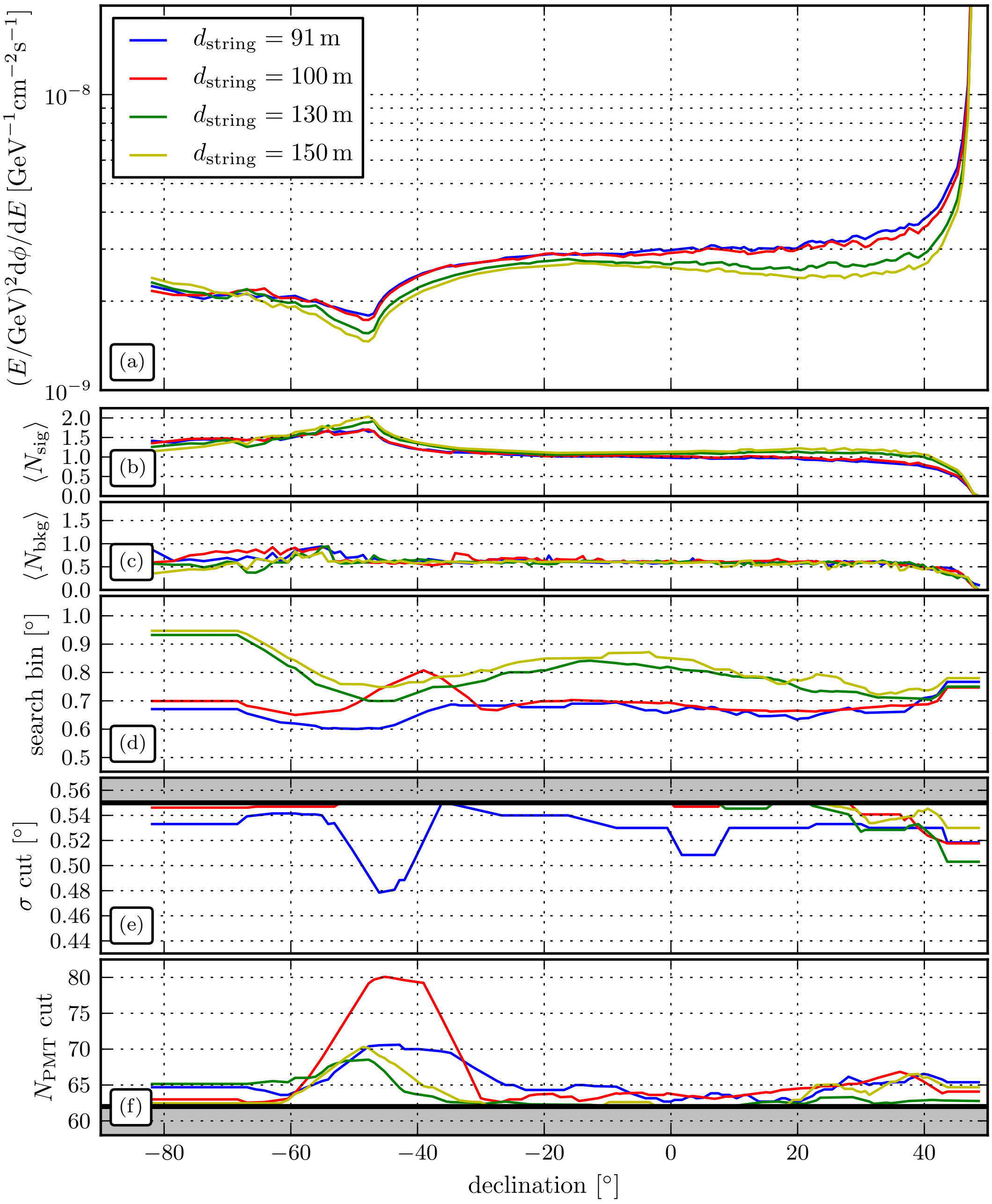

Figure 8.6 Point-source sensitivity (90% C.L.) for one year for the "multiPMT" designs with 310 strings and four different string distances. The subplot contents are analogous to the plots shown on the previous pages.

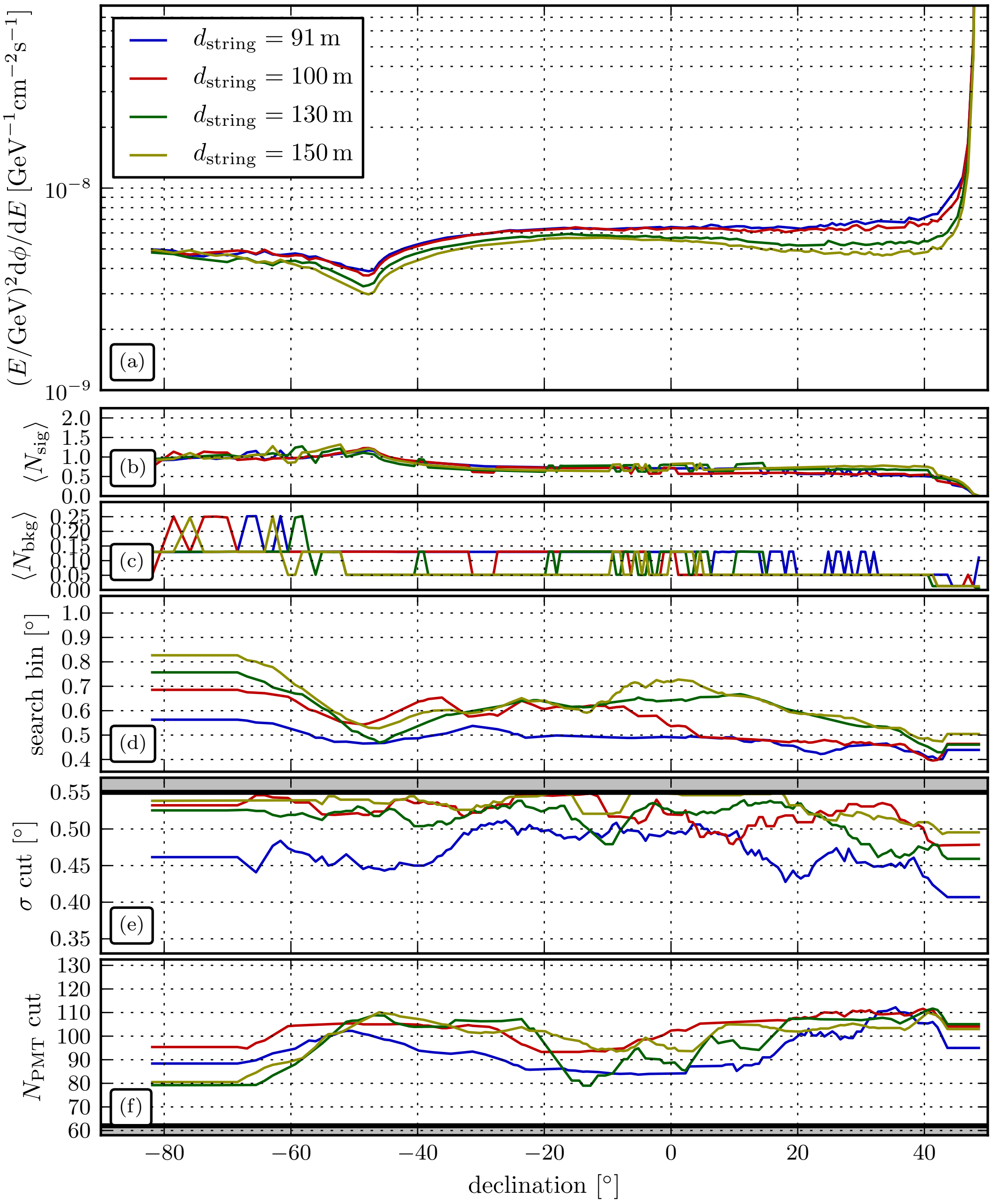

Figure 8.7 5σ Point-source discovery potential (50% of exp.) for one year for the “multiPMT” designs with 310 strings and four different string distances. The subplot contents are analogous to the plots shown on the previous pages.

8.2.4 Discovery potential for SNR RX J1713.7–3946

In order to not only optimise to an artificial E^{-2} benchmark flux, but to a real object with a predicted neutrino spectrum, the SNR RX J1713.7–3946 at declination $\delta = -39.46°$, shall be considered.

The assumed neutrino flux, based on observations in TeV-γ-rays, taken from [27], using updated values [116], is

$$\frac{\mathrm{d}\phi_{\nu_\mu}}{\mathrm{d}E} := k \left(\frac{E}{\mathrm{TeV}}\right)^{-\gamma} \exp\left(-\sqrt{\frac{E}{\epsilon}}\right), \tag{8.2}$$

with

$$k := 16.80 \cdot 10^{-12} \mathrm{TeV}^{-1}\mathrm{cm}^{-2}\mathrm{s}^{-1} \tag{8.3}$$

$$\gamma := 1.78 \tag{8.4}$$

$$\epsilon := 2.10\,\mathrm{TeV}. \tag{8.5}$$

RX J1713 is an extended source, so this fact had to be incorporated into the simulation. As an approximation, all neutrino source directions have been uniformly smeared on a disc with radius 0.65°, centred on the given source location.

With this spectrum, the time to reach an MDF of 1.0 has been determined for each of the four available string distances. At that time, the source will have been detected in 50% of the experiments with a significance of 5σ. The sensitivity and discovery potential optimisations were done using the "low-energy" atmospheric muon constraints presented in section 7.4, because for this source, very high energy neutrinos are unlikely because of its spectrum's rather low cutoff.

Figure 8.8 shows the MDF as a function of time. When compared to the previous results for the E^{-2} benchmark flux, the behaviour is reversed again: detectors with smaller string distances will detect the predicted flux earlier. This, however, is expected for sources with an energy cutoff, as already explained in section 8.1. The time until detection/rejection is summarised in table 8.1, which also includes the mean signal and background event numbers at the detection time.

Unfortunately, the time until a detection on the 5σ level is possible is quite long, over 14 years for any of the detector designs. Be reminded, however, that the track reconstruction algorithm used to get to these results is by no means fully optimised. These results, like all before them, should be regarded as worst-case scenarios.

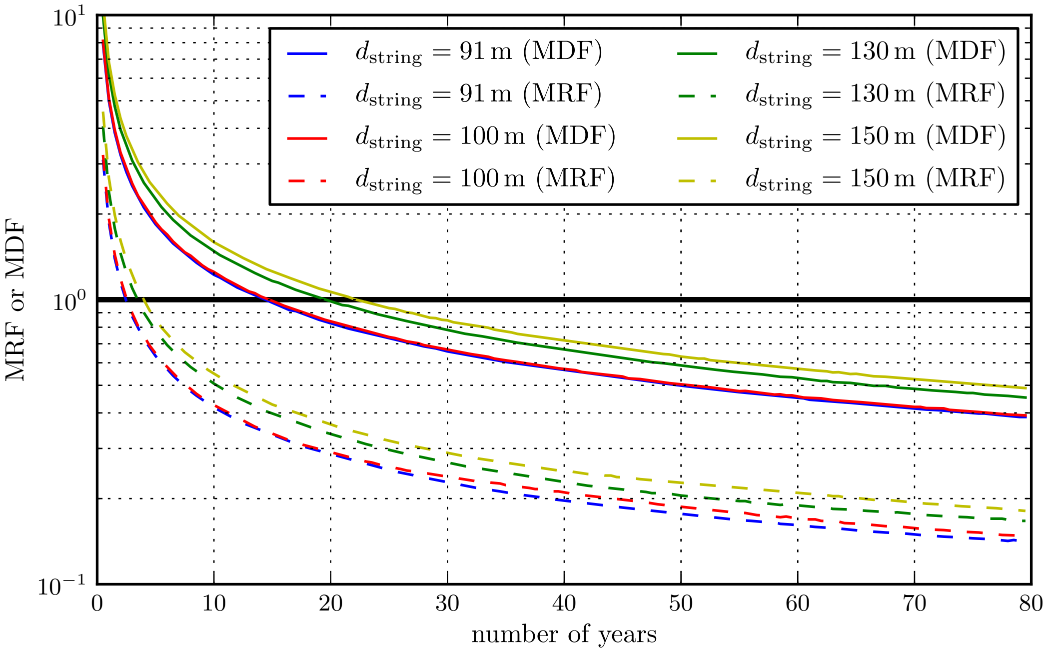

Figure 8.8 MDF and MRF for a predicted neutrino flux from the SNR RX J1713.7–3946 versus observation time.

	sensitivity (90% C.L.)			5σ discovery (50% of exp.)		
string distance	time	n_{sig}	n_{bkg}	time	n_{sig}	n_{bkg}
91 m	2.5 yr	5.14	4.72	14.5 yr	25.96	19.01
100 m	3.0 yr	5.78	5.03	15.0 yr	26.35	19.57
130 m	3.5 yr	5.01	4.37	20.0 yr	25.99	19.00
150 m	4.0 yr	4.79	3.86	22.5 yr	23.52	15.28

Table 8.1 Observation time necessary to reach an MRF or MDF of one for the SNR RX J1713.7–3946. This time is the time necessary to exclude the source with a C.L. of 90% or to detect it with 5σ in 50% of experiments, respectively. Additionally, the mean number of observed signal and background events is given.

Summary and conclusions

The aim of this thesis was to study the performance of different detector design possibilities for the KM3NeT telescope, with the focus on a new design using multiple photomultiplier tubes within a single spherical optical module (the "multiPMT" design). For that purpose, a new Monte Carlo simulation chain was developed within a software framework (IceTray). This chain was then used to perform all simulation work.

The necessary software tools have been implemented as a mixture of freshly created and pre-existing code. The pre-existing code consists of the neutrino event generator ANIS and the lepton propagator MMC, originally developed for IceCube. Due to their good design and the use of a software framework, these tools could easily be re-purposed for KM3NeT. Amongst the algorithms implemented specifically for this work are a full muon and Cherenkov photon propagation algorithm based on Geant4, including a new way to store photon tables for a fast, detailed simulation of light scattering in water. For the "multiPMT" design, a new photomultiplier, readout and electronics simulation has been developed. Additionally, auxiliary code from the original ANTARES software was integrated into the IceTray framework where necessary.

This new toolchain has been compared to the original ANTARES toolchain, revealing minor differences at very high energies. These were attributed to the event generation process at the detector site, i.e. differences between the ANIS generator package and the corresponding tool within the ANTARES toolset, *genhen*. Other than that, no major differences were observed; the two chains yield compatible results.

The new software chain has then been used to simulate three different hypothetical KM3NeT detectors, starting with small volumes of only about $0.5\,\mathrm{km}^3$. Each of these detectors was built according to one of the three possible design options that were discussed for KM3NeT when this thesis was written:[2]

- An ANTARES-like "string" design, with triplets of optical modules per floor on 154 strings. Each string contains 20 floors. The floor spacing is 30 m, the string spacing is 91 m with strings on a hexagonal grid. This design uses the same optical module design as the ANTARES detector, a single photomultiplier tube per optical module with a diameter of $9.3''$ (236.22 mm). It also uses

---

[2] Since then, the details of the design options have been slightly changed, but their basic features are still retained. For example, the current "tower" design uses smaller 8" PMTs and the readout scheme has been changed to an alternative design.

the same readout scheme as ANTARES, an integrating two-channel on-chip design with an all-data-to-shore approach.

- A “tower” design that uses floors made from large metal frame bars with three pairs of optical modules mounted on them. The same optical module design and readout scheme as for the “string” design was used for this detector type. Each tower contains 20 floors with a spacing of 30 m. Because a tower floor contains twice the number of OMs as a floor in the “string” design, the number of towers was chosen to be 80 with a spacing of 130 m. In that way, the photocathode area and average detector instrumentation density are comparable. The 80 strings are still arranged on a hexagonal grid.

- The “multiPMT” design only uses a single optical module per floor, but instead of placing a single, large photomultiplier inside each optical module, 31 smaller PMTs are mounted inside of each one. Their diameter is approximately $3''$ (76 mm). Like the “string” design, 154 strings with 20 OMs per string are used with the same spacings as for that design. This yields approximately the same photocathode area as for the other two designs. The readout scheme used for is different from the other two. It is implemented using a time-over-threshold approach, sending a full time-binned “over-threshold” bitstream to shore.

All data simulated for the two single-PMT designs have been reconstructed using the same modified version of the standard ANTARES reconstruction strategy that has previously been used for other KM3NeT studies. This algorithm is heavily optimised for the single-PMT design and yields excellent angular resolutions of about 0.07° for an incoming E^{-2} flux. It does, however, not yield satisfactory results for the “multiPMT” design. Therefore, a dedicated algorithm, inspired by published work from IceCube, was developed. The new algorithm is far from being optimised and is only a first step to a full dedicated “multiPMT” reconstruction strategy. The angular resolutions obtained for an E^{-2} spectrum with this design are of the order of 0.3°. It is believed that large improvements to this value are possible by refining the reconstruction algorithm.

In terms of neutrino effective area after reconstruction and applying cuts optimised for E^{-2} point-source flux sensitivity, it is the “string” design that does perform best. Both, the “tower” and the “multiPMT” design have worse effective areas, with the exception of the highest energies above 10^6 GeV, where all designs perform similarly. For the “tower” design, this can be explained with the lesser number of vertical structures, effectively leading to a less dense detector in terms of strings per seafloor area. However, it may very well be that the total deployment cost per optical module is cheaper for the “tower” design, thus allowing to use more than the 80 towers that were simulated. This would bring the “tower” design on par with the “string” one.

For the “multiPMT” design, the worse effective area can be accounted for through the non-refined track reconstruction strategy. With its angular resolution being a factor four worse than for the other two designs, much harder cuts have to be used to optimise for E^{-2} point-source flux sensitivity. Especially for this design, large improvements are to be expected after refinement of the reconstruction algorithm. All results presented for this design should thus be seen as worst-case scenarios.[3]

Comparing the E^{-2} point-source flux sensitivities and discovery potentials yields the same behaviour as for the effective areas: the “string” design performs best, followed closely by the “tower” design. Despite the lower effective area and worse angular resolution, the “multiPMT” design performs fairly good when compared to the other two designs. During these and all following sensitivity and discovery potential calculations, cuts an the reconstruction quality parameters and on the number of PMTs with at least one hit were used. The latter one is a crude energy cut that had to be used in the absence of a dedicated energy reconstruction algorithm for KM3NeT.

From this point on, the focus was on the “multiPMT” design. This design possibility has not been studied before as much as the others, especially due to the fact that no satisfactory track reconstruction algorithm existed up to now.

Up to this point, the only background flux used for the sensitivity calculations was the one of atmospheric neutrinos. The reason for this is the immense computational time needed to simulate an atmospheric muon flux with the necessary statistics. Using a small sample of atmospheric muon background events, simulated for the “multiPMT” design, the effect of these events on the point-source sensitivity and discovery potential has been studied by extrapolating constraints on the energy cut level for different quality cut levels. The imposed requirement was to reduce the atmospheric muon background to 10% of the atmospheric neutrino background. These constraints have a visible impact on the point-source flux sensitivity, but hardly change the discovery potential. This is because the discovery potential cut optimisation already yields optimal cut levels that fulfil the atmospheric muon constraints. The constraints derived for this detector type were then used for all the following results.

Scaling of the “multiPMT” detector from its initial number of strings (154) to double its size was examined. This was done in two different ways: the performance of having two identical smaller detectors at different sites was compared to a single, large detector. This larger detector, was chosen to consist of 310 strings on a hexagonal seafloor grid. The string design was kept unchanged. For an E^{-2} flux without a cutoff, two smaller detectors yield better point-source sensitivity. When, however, introducing a cutoff into the spectrum, the single large detector performs better. This is because of neutrinos with very high energies $E_\nu \gtrsim 10^6\,\mathrm{GeV}$, produc-

---

[3] This is of course also true for the other designs, but the improvements will probably be less for them.

ing high-energy muons with very long track lengths. For them, the smaller detector design is still surface-dominated. As spectrum cutoffs are expected for almost all sources, building a single large detector seems to be the favourable choice.

Keeping the string number constant at a value of 310, the effects of varying the string distance and thus the detector density was studied. In addition to the string distance of 91 m that was used before, three new detectors with string distances of 100 m, 130 m and 150 m were considered. All other parameters were kept unchanged. For an unbroken E^{-2} flux, the 150 m detector turns out to be optimal in terms of sensitivity and discovery potential, especially at track directions near the horizon where neutrino absorption in the Earth at the highest energies does not play a large role yet.

Injecting the neutrino spectrum predicted for a known TeV-γ-ray source yields different results. The chosen spectrum was for the supernova remnant RXJ1713.7-3946 under the assumption of hadronic acceleration. Due to its spectrum's energy cutoff, the two detectors with smaller string distances (91 m and 100 m) yield better sensitivities and discovery potentials. With one of these detectors, a 5σ detection of the source would be possible after 15 years. Keep in mind, however, that these results were obtained using a non-optimised reconstruction algorithm and with only a crude cut on energy. Additionally, improvements are to be expected by using an unbinned analysis technique instead of the binned one used in this work. During the last phase of this work, it became clear that detectors with even more strings were a serious possibility. The currently discussed possibilities are detectors with over 600 strings. Taking all these points into account, KM3NeT has a very good chance to detect Galactic neutrino sources. A detector with a string distance of about 100 m should also be able to detect extragalactic sources with higher energy cutoffs and harder spectra. Taking into account higher neutrino energies, the differences between a detector with this string distance and the ones with larger distances are not too pronounced. Of course, there is also the possibility of neutrino sources where the emitted γ-rays are heavily absorbed within the source itself. Should they exist, their discovery would present an important step forward in neutrino and cosmic ray astronomy.

Building the KM3NeT neutrino telescope presents an important opportunity for the whole field of astroparticle physics, including many aspects that were not even touched in this thesis. Having a complementary neutrino telescope to IceCube on the Northern Hemisphere and a more sensitive instrument at the same time will certainly lead to a lot of exciting discoveries. Most of them will probably be entirely unexpected.

Zusammenfassung und Ausblick

Ziel dieser Arbeit war es, die Effizienz verschiedener Design-Optionen für das Neutrinoteleskop der nächsten Generation im Mittelmeer, „KM3NeT“, zu untersuchen. Der Fokus lag dabei auf einem neuen Design, bei welchem mehrere Photomultiplier innerhalb eines optischen Moduls angebracht sind (dem sog. „MultiPMT“-Design). Zu diesem Zweck wurde eine neue Monte Carlo-Simulationskette innerhalb eines Software-Frameworks („IceTray“) entwickelt. Mittels dieser Kette wurden dann alle Simulationen durchgeführt.

Die benötigte Software wurde als eine Mischung aus neu entwickeltem und bereits vorhandenem Code implementiert. Der bereits existierende Code besteht aus dem Neutrino-Ereignisgenerator ANIS und dem Lepton-Propagator MMC. Beide Werkzeuge wurden ursprünglich für IceCube entwickelt. Aufgrund ihres guten Designs und durch die Benutzung eines Software-Framworks konnten sie sehr leicht für KM3NeT verwendet werden. Speziell für diese Arbeit wurde eine vollständige Myon- und Cherenkov-Photonen-Simulation auf Basis von Geant4 implementiert. Diese beinhaltet einen neuen Algorithmus zur Speicherung von Photonentabellen zur schnellen und detaillierten Simulation von Streuung in Wasser. Für das „MultiPMT“-Design wurde ein neuer Algorithmus zur Simulation der Photomultiplier und der Ausleseelektronik entwickelt. Falls erforderlich, wurde Code aus der Software des bestehenden Neutrino-Detektors ANTARES in das IceTray-Framework integriert.

Diese neue Simulationskette wurde mit der bestehenden ANTARES-Simulationskette verglichen, wobei kleine Unterschiede bei sehr hohen Energien festgestellt wurden. Diese lassen sich auf Unterschiede zwischen dem Ereignisgenerator ANIS und dem entsprechenden Tool aus der ANTARES-Simulationskette („genhen“) zurückführen. Weiterhin wurden keine bedeutenden Unterschiede festgestellt; beide Simulationsketten liefern vergleichbare Ergebnisse.

Mittels der neuen Simulationskette wurden nun drei verschiedene hypothetische KM3NeT-Detektoren simuliert, wobei anfangs ein relativ kleines Volumen von $0.5\,\mathrm{km}^3$ gewählt wurde. Jeder dieser Detektoren entspricht einer der drei möglichen Design-Optionen, die während der Anfertigung dieser Arbeit diskutiert wurden:[4]

- Das „String“-Design basiert weitgehend auf der Konstruktion des bisherigen ANTARES-Detektors. Auf jedem Stockwerk befinden sich drei, um 45° von der Horizontalen nach unten geneigte, optische Module. Jeweils 20 von diesen

---

[4] Seitdem haben sich die Parameter dieser Optionen leicht geändert, ihre grundlegenden Eigenschaften blieben aber unverändert. So wurde zum Beispiel beim „Tower“-Design die Größe der Photomultiplier auf 8 Zoll angepasst und die Auslesemethode verändert.

Stockwerken mit einem Abstand von 30 m bilden einen vertikalen „String“. Der gesamte Detektor besteht aus 154 dieser Strings, welche im Abstand von 91 m auf einem hexagonalen Gitter angeordnet sind. Der Aufbau der optischen Module entspricht dem des ANTARES-Detektors, d.h. einem einzelnen Photomultiplier mit 9.3″ (236.22 mm) Durchmesser pro Modul. Auch die Ausleseelektronik ist analog zum ANTARES-Detektor simuliert: Das gemessene Signal wird auf einem zwei-kanaligen Chip integriert und zur Küstenstation geschickt, wo es weiter verarbeitet wird.

- Beim „Tower“-Design bestehen die Detektor-Stockwerke aus großen Metallgerüst-Balken, an deren Enden und Mitte jeweils Paare von optischen Modulen angebracht sind. Für diesen Detektor-Typ wurde in der Simulation die gleiche Auslese-Elektronik wie für das „String“-Design simuliert. Jeder „Tower“ besteht aus 20 Stockwerken in einem Abstand von jeweils 30 m. Da jedes Stockwerk, verglichen mit dem vorhergehenden Design, die doppelte Anzahl von optischen Modulen besitzt, besteht der simulierte Detektor nur aus 80 dieser Einheiten. Diese haben einen horizontalen Abstand von 130 m, wiederum angeordnet auf einem hexagonalen Gitter. Dadurch bleiben die Photokathodenfläche und die mittlere Instrumentierungsdichte der beiden Detektoren vergleichbar.

- Das „MultiPMT“-Design besteht aus nur einem optischen Modul pro Stockwerk, welches nun allerdings 31 kleinere Photomultiplier mit Durchmessern von 3″ (76 mm) enthält. Wie beim „String“-Design besteht der Detektor aus 154 Strings mit jeweils 20 Stockwerken pro String. Dadurch erhält man in etwa die gleiche Photokathodenfläche wie bei den beiden anderen Designs. Die Ausleseelektronik ist hier mittels eines „Time-over-threshold“-Ansatzes implementiert, wobei ein durchgehender, zeitlich unterteilter Bit-Strom zur Küstenstation gesendet wird.

Alle simulierten Daten für die beiden erstgenannten Designs wurden mittels desselben Algorithmus rekonstruiert, der auch bereits zuvor für eine Vielzahl von KM3NeT-Studien verwendet wurde. Es handelt sich hierbei um eine leicht modifizierte Version des Standard-ANTARES-Rekonstruktionsalgorithmus. Da dieser stark auf Detektoren optimiert ist, die denselben optischen Modul-Typ wie ANTARES verwenden, ergeben sich sehr gute Winkelauflösungen von ca. 0.07° für das rekonstruierte Myon bei einem simulierten E^{-2}-Fluss. Für das „MultiPMT“-Design hingegen wurden damit keine zufriedenstellenden Ergebnisse erzielt. Daher wurde eigens hierfür ein Rekonstruktions-Algorithmus entwickelt, der auf veröffentlichten Beschreibungen eines IceCube-Algorithmus basiert. Dieser neue Algorithmus ist noch nicht optimiert und daher nur als erster Schritt zu einer vollständigen „MultiPMT“-Rekonstruktion anzusehen. Die erreichte Winkelauflösung für Myonen für einen E^{-2}-Fluss bewegt sich um 0.3°. Dieser Wert sollte sich durch Weiterentwicklung des Rekonstruktions-Algorithmus stark verbessern lassen.

Betrachtet man die effektiven Flächen für Neutrinos nach der Spurrekonstruktion und optimiert die Qualitätsschnitte auf bestmögliche Punktquellen-Sensitivität für einen angenommenen E^{-2}-Fluss, so schneidet der „String"-Detektor am Besten ab. Sieht man vom Energiebereich über 10^6 GeV ab, so sind die effektive Flächen der anderen beiden Detektoren etwas kleiner. Dies kann beim „Tower"-Design mit der geringeren Anzahl an vertikalen Strukturen erklärt werden, welche zu einer kleineren Dichte, bezogen auf „Strings pro Meeresbodenfläche", führt. Allerdings ist es gut möglich, dass die Gesamtkosten pro optischem Modul einschließlich der Aufbaukosten für das „Tower"-Design kleiner sind, so dass in diesem Fall mehr als die simulierten 80 Strings benutzt werden könnten.

Beim „MultiPMT"-Design kann man die kleinere effektive Fläche mit dem noch nicht vollständig optimierten Spurrekonstruktions-Algorithmus erklären. Aufgrund der um einen Faktor vier schlechteren Winkelauflösung im Vergleich zu den anderen beiden Designs, führt eine Optimierung auf Punktquellen-Sensitivität zu sehr viel härteren Schnitten. Es ist daher insbesondere bei diesem Design mit großen Verbesserungen in der Rekonstruktionseffizienz nach einer Optimierung des Rekonstruktions-Algorithmus zu rechnen.[5]

Betrachtet man die Sensitivitäten und Entdeckungspotentiale für Punktquellen mit einem E^{-2}-Fluss, so ergibt sich dasselbe Bild: Das „String"-Design schneidet knapp vor dem „Tower"-Design am Besten ab. Trotzdem sind die Ergebnisse auch für das „MultiPMT"-Design relativ gut. Für diese und alle folgenden Berechnungen wurden Schnitte auf die Rekonstruktions-Qualität und auf die Energie des den Detektor durchquerenden Teilchens angewendet. Da kein geeigneter Energierekonstruktions-Algorithmus zur Verfügung stand, wurde der Energieschnitt auf die Anzahl der Photomultiplier mit mindestens einem Treffer gelegt, einer Wert, der grob mit der Energie des Teilchens korreliert ist.

Von nun an lag der Fokus der Arbeit auf dem „MultiPMT"-Design. Dieses wurde in vorhergehenden Arbeiten nicht in derselben Ausführlichkeit untersucht wie die beiden anderen Designs, was zum großen Teil auf das Fehlen einer leistungsfähigen Spurrekonstruktion zurückzuführen sein dürfte.

In den bisherigen Betrachtungen bestand der simulierte Untergrund einzig aus atmosphärischen Neutrinos; fälschlicherweise als nach oben laufend rekonstruierte atmosphärische Myonen wurden vernachlässigt. Der Grund hierfür liegt in der immensen Rechenzeit, die benötigt wird, um ausreichende Statistik zu generieren. Die Auswirkungen auf Punktquellen-Sensitivitäten wurden daher aus einer kleineren Menge an simulierten Ereignissen extrapoliert. Die sich ergebenden Einschrän-

---

[5] Natürlich lassen sich die Ergebnisse auch für die anderen beiden Detektor-Designs durch Optimierung des Rekonstruktions-Algorithmus verbessern, allerdings ist zu erwarten, dass die Verbesserungen für diese kleiner ausfallen.

kungen an die Qualitäts- und Energie-Schnitte wurden so gewählt, dass die Anzahl der Untergrundereignisse aus atmosphärischen Myonen weniger als 10% der Anzahl der Ereignisse aus atmosphärischen Neutrinos beträgt. Die härteren Schnitte haben sichtbaren Einfluss auf die Punktquellen-Sensitivitäten. Dagegen ändern sich die Entdeckungspotentiale kaum. Der Grund hierfür ist, dass die optimierten Schnitte in diesem Fall schon die Einschränkungen zur Unterdrückung des atmosphärischen Myon-Untergrundes erfüllen. Für alle weiteren Studien wurden nun diese Einschränkungen an die Schnitte benutzt.

Weiterhin wurden die Auswirkungen einer Verdoppelung der Anzahl der Strings eines „MultiPMT“-Detektors untersucht. Die Effizienz eines einzelnen, großen Detektors wurde mit derjenigen von zwei identischen, kleineren, an verschiedenen Stellen gebauten Detektoren verglichen. Der große Detektor bestand aus 310 Strings (verglichen mit 154 beim kleineren). Der Abstand der Strings wurde beibehalten. Für ein E^{-2}-Spektrum ergibt sich eine bessere Sensitivität für zwei kleine Detektoren. Führt man in das simulierte Quellspektrum allerdings einen Energie-Cutoff ein, so schneidet der große Detektor besser ab. Dies lässt sich mit Neutrinos hoher Energie ($E_\nu \gtrsim 10^6\,\mathrm{GeV}$) erklären, welche zu sehr langen Myon-Spuren führen. Detektoren mit größerer Oberfläche sind hier von Vorteil, was zur besseren Sensitivität von zwei kleinen Detektoren führt. Da reale Quellspektren im Allgemeinen aber einen Cutoff besitzen, ist der Bau eines großen Detektors die vorzuziehende Alternative.

Nun wurden die Auswirkungen der Änderung des String-Abstands für Detektoren mit 310 Strings untersucht. Zusätzlich zum bereits betrachteten Detektor mit einem Abstand von 91 m wurden noch solche mit Abständen von 100 m, 130 m und 150 m simuliert. Für ein E^{-2}-Spektrum ohne Cutoff erscheint der größte Detektor mit einem Abstand von 150 m als optimal in Bezug auf Sensitivität und Entdeckungspotential, insbesondere für Spuren nahe dem Horizont, bei denen die Absorption von höchstenergetischen Neutrinos in der Erde noch keine große Rolle spielt.

Simuliert man ein erwartetes Neutrino-Spektrum für eine bekannte TeV-γ-Strahlungsquelle, so erhält man abweichende Ergebnisse. Hier wurde ein erwartetes Spektrum für den Supernova-Überrest RXJ1713.7-3946 benutzt. Aufgrund des Energie-Cutoffs dieses Spektrums erhält man bessere Sensitivitäten für Detektoren mit kleineren String-Abständen (91 m und 100 m). Mit einem dieser Detektoren ist eine Entdeckung der Quelle auf 5σ-Niveau nach 15 Jahren möglich. Dabei sollte aber beachtet werden, dass dieses Ergebnis mit einer noch nicht optimalen Rekonstruktion und einem nur groben Energieschnitt bestimmt wurde. Zusätzlich sind Verbesserungen durch die Benutzung einer „ungebinnten“ Analyse (im Gegensatz zu der „gebinnten“ Analyse, welche in dieser Arbeit verwendet wurde) zu erwarten. In der Endphase der Entstehung dieser Arbeit wurde weiterhin klar, dass der Bau von Detektoren mit weit mehr als den bisher betrachteten 310 Strings ernsthaft in Betracht gezogen wird. Nimmt man all diese Punkt zusammen, so rückt die Entdeckung von galaktischen Neutrino-Quellen mit KM3NeT in greifbare Nähe. Ein Detektor mit einem String-Abstand von 100 m sollte zudem weiterhin extragalaktische Quellen mit einem höheren Energie-Cutoff und härteren Spektren detektieren können. Natürlich besteht auch die Möglichkeit für Neutrino-Quellen, deren γ-Strahlen stark in der Quelle selbst absorbiert sind. Sollten sie existieren, so wäre ihre Entdeckung ein wichtiger Schritt für die Neutrino-Astronomie und die Astronomie der kosmischen Strahlung im Allgemeinen.

Der Bau des KM3NeT-Neutrinoteleskops stellt eine einzigartige Chance für das gesamte Feld der Astroteilchenphysik dar und bietet Möglichkeiten, die weit über das in dieser Arbeit Beschriebene hinausgehen. Ein zu IceCube komplementäres Neutrinoteleskop auf der Nordhalbkugel, welches zudem noch sensitiver ist, wird mit Sicherheit zu spannenden Entdeckungen führen. Die meisten davon werden wohl völlig unerwartet sein.

Bibliography

[1] R. Kronig and V. F. Weisskopf, editors. *Wolfgang Pauli: Collected scientific papers*, volume 2. Interscience Publishers, New York, 1964. (Cited on page 15.)

[2] C. L Cowan, F Reines, F. B Harrison, et al. Detection of the Free Neutrino: A Confirmation. *Science*, 124:103, 1956. (Cited on page 15.)

[3] G Danby, J.-M Gaillard, K Goulianos, et al. Observation of High-Energy Neutrino Reactions and the Existence of Two Kinds of Neutrinos. *Physical Review Letters*, 9:36, 1962. (Cited on page 16.)

[4] DONUT Collaboration, K Kodama, N Ushida, et al. Observation of tau neutrino interactions. *Physics Letters B*, 504:218, 2001. (Cited on page 16.)

[5] LEP Collaborations. A Combination of Preliminary Electroweak Measurements and Constraints on the Standard Model. *CERN Document PPE/96-183*, pages 96–183, 1996. (Cited on page 16.)

[6] Q R Ahmad, R. C Allen, T. C Andersen, et al. Measurement of the Rate of $\nu_e + d \rightarrow p + p + e^-$ Interactions Produced by 8B Solar Neutrinos at the Sudbury Neutrino Observatory. *Physical Review Letters*, 87:71301, 2001. (Cited on page 16.)

[7] Raymond Davis. Nobel Lecture: A half-century with solar neutrinos. *Reviews of Modern Physics*, 75:985, 2003. (Cited on page 16.)

[8] M Nagano and A. A Watson. Observations and implications of the ultrahigh-energy cosmic rays. *Reviews of Modern Physics*, 72:689, 2000. (Cited on page 16.)

[9] Günter Sigl. Ultrahigh-Energy Cosmic Rays: Physics and Astrophysics at Extreme Energies. *Science*, 291:73, 2001. (Cited on page 16.)

[10] V F Hess. Über Beobachtungen der durchdringenden Strahlung bei sieben Freiballonfahrten. *Phys. Z.*, 13:1084–1091, 1912. (Cited on page 16.)

[11] Kenneth Greisen. End to the Cosmic-Ray Spectrum? *Physical Review Letters*, 16:748, 1966. (Cited on page 17.)

[12] G. T Zatsepin and V. A Kuz'min. Upper Limit of the Spectrum of Cosmic Rays. *ZhETF Pis ma Redaktsiiu*, 4:114, 1966. (Cited on page 17.)

[13] J. W Cronin, T. K Gaisser, and S. P Swordy. Cosmic rays at the energy frontier. *Sci. Am.*, 276(1):32–37, 1997. (Cited on page 18.)

[14] D. J Bird, S. C Corbato, H. Y Dai, et al. The cosmic-ray energy spectrum observed by the Fly's Eye. *Astrophys. J*, 424:491, 1994. (Cited on page 18.)

[15] M. A Lawrence, R. J. O Reid, and A. A Watson. The cosmic ray energy spectrum above 4×10^{17} eV as measured by the h Park array. *Journal of Physics G: Nuclear and Particle Physics*, 17:733, 1991. (Cited on page 18.)

[16] M Nagano, M Teshima, Y Matsubara, et al. Energy spectrum of primary cosmic rays above $10^{17.0}$ eV determined from extensive air shower experiments at Akeno. *Journal of Physics G: Nuclear and Particle Physics*, 18:423, 1992. (Cited on page 18.)

[17] E. S Seo, J. F Ormes, R. E Streitmatter, et al. Measurement of cosmic-ray proton and helium spectra during the 1987 solar minimum. *Astrophys. J*, 378: 763, 1991. (Cited on page 18.)

[18] W. I Axford, E Leer, and G Skadron. The Acceleration of Cosmic Rays by Shock Waves. *Proceedings of the 15th International Cosmic Ray Conference*, 11:132, 1977. (Cited on page 17.)

[19] A. R Bell. The acceleration of cosmic rays in shock fronts. I. *Royal Astronomical Society*, 182:147, 1978. (Cited on page 17.)

[20] R. D Blandford and J. P Ostriker. Particle acceleration by astrophysical shocks. *Astrophys. J*, 221:L29, 1978. (Cited on page 17.)

[21] G. F Krymskii. A regular mechanism for the acceleration of charged particles on the front of a shock wave. *Akademiia Nauk SSSR*, 234:1306, 1977. (Cited on page 17.)

[22] John G Learned and Karl Mannheim. High-Energy Neutrino Astrophysics. *Annual Reviews of Nuclear and Particle Science*, 50:679, 2000. (Cited on pages 20 and 21.)

[23] Julia K Becker. High-energy neutrinos in the context of multimessenger astrophysics. *Physics Reports*, 458:173, 2008. (Cited on page 21.)

[24] Eli Waxman and John Bahcall. High energy neutrinos from astrophysical sources: An upper bound. *Phys. Rev. D*, 59:23002, 1999. (Cited on page 22.)

[25] VERITAS Collaboration, V. A Acciari, E Aliu, et al. A connection between star formation activity and cosmic rays in the starburst galaxy M82. *Nature*, 462:770, 2009. (Cited on page 22.)

[26] Abraham Loeb and Eli Waxman. The cumulative background of high energy neutrinos from starburst galaxies. *Journal of Cosmology and Astroparticle Physics*, 05:003, 2006. (Cited on page 22.)

[27] Alexander Kappes, Jim Hinton, Christian Stegmann, et al. Potential neutrino signals from galactic gamma-ray sources. *Astrophys. J*, 656(2):870–878, 2007. (Cited on pages 22 and 139.)

[28] J Alvarez-Muñiz and F Halzen. Possible High-Energy Neutrinos from the Cosmic Accelerator RX J1713.7-3946. *The Astrophysical Journal*, 576:L33, 2002. (Cited on page 22.)

[29] Felix A Aharonian, A. G Akhperjanian, A. R Bazer-Bachi, et al. Observations of the Crab nebula with HESS. *Astronomy and Astrophysics*, 457:899, 2006. (Cited on page 22.)

[30] Felix A Aharonian, A. G Akhperjanian, A. R Bazer-Bachi, et al. First detection of a VHE gamma-ray spectral maximum from a cosmic source: HESS discovery of the Vela X nebula. *Astronomy and Astrophysics*, 448:L43, 2006. (Cited on page 22.)

[31] W Bednarek. Neutrinos from the pulsar wind nebulae. *Astronomy and Astrophysics*, 407:1, 2003. (Cited on page 22.)

[32] Anna Balenzano, Fiorella Burgio, and Teresa Montaruli. Review of models of galactic sources and rate estimates in ANTARES: young supernova remnants, plerions, magnetars and microquasars. *ANTARES internal note*, 2004. (Cited on page 23.)

[33] C Distefano, D Guetta, Eli Waxman, et al. Neutrino Flux Predictions for Known Galactic Microquasars. *The Astrophysical Journal*, 575:378, 2002. (Cited on page 23.)

[34] Felix A Aharonian, L Anchordoqui, D Khangulyan, et al. Microquasar LS 5039: a TeV gamma-ray emitter and a potential TeV neutrino source. *Journal of Physics: Conference Series*, 39:408, 2006. (Cited on page 23.)

[35] Franck Bernard. *Caractérisation des performances d'un télescope sous-marin à neutrinos pour la détection du cascades contenues dans le cadre du project ANTARES*. PhD thesis, Université de la Méditerranée, 2000. (Cited on page 27.)

[36] A Gazizov and Marek Kowalski. ANIS: High energy neutrino generator for neutrino telescopes. *Comput. Phys. Commun.*, 172:203, 2005. (Cited on pages 28, 54, 56, and 57.)

[37] P. A Čerenkov. Visible Radiation Produced by Electrons Moving in a Medium with Velocities Exceeding that of Light. *Physical Review*, 52:378, 1937. (Cited on page 29.)

[38] Cristina Cârloganu. Muon Interactions at High Energies. *ANTARES internal note*, 1998. (Cited on page 30.)

[39] C. H Wiebusch. *The Detection of Faint Light in Deep Underwater Neutrino Telescopes*. PhD thesis, RWTH Aachen, 1995. (Cited on pages 29 and 30.)

[40] N Palanque-Delabrouille. Light transmission in the ANTARES site Measurement in blue light (Analysis of Test 3' data). *ANTARES internal note*, 1999. (Cited on page 31.)

[41] David J.L Bailey. The effect of the group velocity and dispersion on photon arrival times in the ANTARES detector. *ANTARES internal note*, 2001. (Cited on page 32.)

[42] Stéphanie Escoffier and Anne-Sophie Cussatlegras. Correlations between bioluminescence and environmental parameters with ANTARES data in 2003 (PSL) and 2005 (MILOM). *ANTARES internal note*, 2006. (Cited on page 35.)

[43] Raj Gandhi, Chris Quigg, Mary Hall Reno, et al. Neutrino interactions at ultrahigh energies. *Phys. Rev. D*, 58:93009, 1998. (Cited on page 37.)

[44] Raj Gandhi, Chris Quigg, Mary Hall Reno, et al. Ultrahigh-energy neutrino interactions. *Astropart. Phys.*, 5:81, 1996. (Cited on page 37.)

[45] S Cecchini, E Korolkova, A Margiotta, et al. Atmospheric muon background in the ANTARES detector. *Proceedings of the 29th International Cosmic Ray Conference*, 5, 2005. (Cited on page 36.)

[46] GD Barr, TK Gaisser, Paolo Lipari, et al. Three-dimensional calculation of atmospheric neutrinos. *Phys. Rev. D*, 70(2):023006, 2004. (Cited on page 37.)

[47] G Fiorentini, VA Naumov, and FL Villante. Atmospheric neutrino flux supported by recent muon experiments. *Physics Letters B*, 510(1-4):173–188, 2001. (Cited on page 37.)

[48] Arthur Roberts. The birth of high-energy neutrino astronomy: A personal history of the DUMAND project. *Reviews of Modern Physics*, 64:259, 1992. (Cited on page 38.)

[49] V Aynutdinov, A Avrorin, V Balkanov, et al. The BAIKAL neutrino experiment — Physics results and perspectives. *Nucl. Instr. Meth. A*, 602:14, 2009. (Cited on pages 38 and 39.)

[50] Spencer R Klein. IceCube: A Cubic Kilometer Radiation Detector. *IEEE Transactions on Nuclear Science*, 56:1141, 2009. (Cited on pages 39, 40, and 52.)

[51] ANTARES Collaboration. Performance of the front-end electronics of the ANTARES neutrino telescope. 2009. (Cited on page 41.)

[52] E Migneco, S Aiello, A Aloisio, et al. Recent achievements of the NEMO project. *Nucl. Instr. Meth. A*, 588:111, 2008. (Cited on page 42.)

[53] Nestor Collaboration, E. G Anassontzis, A. E Ball, et al. Operation and performance of the NESTOR test detector. *Nucl. Instr. Meth. A*, 552:420, 2005. (Cited on page 42.)

[54] Nestor Collaboration, G Aggouras, E. G Anassontzis, et al. A measurement of the cosmic-ray muon flux with a module of the NESTOR neutrino telescope. *Astropart. Phys.*, 23:377, 2005. (Cited on page 42.)

[55] KM3NeTConsortium. KM3NeT Conceptual Design for a Deep-Sea Research Infrastructure Incorporating a Very Large Volume Neutrino Telescope in the Mediterranean Sea. *KM3NeT CDR*, 2008. (Cited on page 42.)

[56] Paul Kooijman. SeaWiet — SEnsor Architecture for a WIde Energy range Telescope. *KM3NeT internal report*, 2009. (Cited on pages 43 and 81.)

[57] Jürgen Brunner. Antares simulation tools. *ANTARES internal note*, 2003. (Cited on page 47.)

[58] Jürgen Brunner. General purpose data format for ANTARES simulation and reconstruction. *ANTARES internal note*, 1998. (Cited on page 47.)

[59] Jürgen Brunner. Updated tag list fot the new ANTARES event format. *ANTARES internal note*, 1999. (Cited on page 47.)

[60] F Cassol. GENDET 1.0: a program to generate detector files. *ANTARES internal note*, 1999. (Cited on page 47.)

[61] Franca Cassol-Brunner. GENDET 1.2: cards and tags. *ANTARES internal note*, 2000. (Cited on page 47.)

[62] David J.L Bailey. Extension of Genneu to v3r0. *ANTARES internal note*, 2000. (Cited on page 48.)

[63] David J.L Bailey. Genhen v3r1: Further optimisation for large energy ranges. *ANTARES internal note*, 2000. (Cited on page 48.)

[64] David J.L Bailey. Genhen v5r1: Software Documentation. *ANTARES internal note*, 2002. (Cited on page 48.)

[65] Jürgen Brunner. Event generators for ANTARES nu oscillation search. *ANTARES internal note*, 1998. (Cited on page 48.)

[66] Konstantin Kuzmin, Teresa Montaruli, and Igor A Sokalski. GENHEN v6r3: implementation of the Glashow resonance and of the MUSIC transport code. *ANTARES internal note*, 2004. (Cited on page 48.)

[67] Annalisa L'Abbate, Teresa Montaruli, and Igor A Sokalski. GENHEN v6: ANTARES neutrino generator extension to all neutrino flavors and inclusion of propagation through the Earth. *ANTARES internal note*, 2004. (Cited on page 48.)

[68] G Ingelman, A Edin, and J Rathsman. LEPTO 6.5 — A Monte Carlo generator for deep inelastic lepton-nucleon scattering. *Comput. Phys. Commun.*, 101:108, 1997. (Cited on page 48.)

[69] Giles David Barr. *The Separation of Signals and Background in a Nucleon Decay Experiment.* PhD thesis, University of Oxford, 1987. (Cited on page 48.)

[70] P Antonioli, C Ghetti, E. V Korolkova, et al. A three-dimensional code for muon propagation through the rock: MUSIC. *Astropart. Phys.*, 7:357, 1997. (Cited on page 48.)

[71] Edgar V Bugaev, Igor A Sokalski, and S. I Klimushin. Simulation accuracy of long range muon propagation in medium: analysis of error sources. *arXiv*, hep-ph, 2000. (Cited on page 48.)

[72] Igor A Sokalski, Edgar V Bugaev, and Sergey I Klimushin. MUM: Flexible precise Monte Carlo algorithm for muon propagation through thick layers of matter. *Phys. Rev. D*, 64:74015, 2001. (Cited on page 48.)

[73] Paolo Lipari and Todor Stanev. Propagation of multi-TeV muons. *Phys. Rev. D*, 44:3543, 1991. (Cited on page 48.)

[74] David J.L Bailey. KM3 v2r1: User Guide. *ANTARES internal note*, 2002. (Cited on pages 48, 49, and 61.)

[75] Sergio Navas and L. F Thompson. KM3 User Guide and Reference Manual. *ANTARES internal note*, 1999. (Cited on page 48.)

[76] Computing Application Software Group and Networks Division. GEANT Detector Description and Simulation Tool. *CERN Program Library Long Writeup*, W5013, 1993. (Cited on page 49.)

[77] A Heijboer. *Track Reconstruction and Point Source Searches with ANTARES.* PhD thesis, Universiteit van Amsterdam, 2004. (Cited on pages 50 and 86.)

[78] Sebastian Kuch. *Design studies for the KM3NeT Neutrino Telescope.* PhD thesis, Universität Erlangen, 2007. (Cited on pages 50 and 119.)

[79] Claudio Kopper, Thomas Eberl, and Alexander Kappes. A software framework for KM3NeT. *Proceedings of the 31st International Cosmic Ray Conference*, 2009. (Cited on page 50.)

[80] T de Young. IceTray: A Software Framework for IceCube. *International Conference on Computing in High-Energy Physics and Nuclear Physics (CHEP2004)*, 2004. (Cited on page 52.)

[81] *available from* `http://www.boost.org/`. (Cited on page 52.)

[82] J A Aguilar, A Albert, F Ameli, et al. The data acquisition system for the ANTARES neutrino telescope. *Nucl. Instr. Meth. A*, 570:107, 2007. (Cited on page 52.)

[83] *see* `http://www.python.org/`. (Cited on page 52.)

[84] Ralf Auer. PhD thesis, Erlangen Centre for Astroparticle Physics (ECAP), Universität Erlangen, 2010. In preparation. (Cited on page 53.)

[85] Felix Fehr. *Systematic studies, calibration, and software development for event reconstruction and data analysis using the ANTARES deep-sea neutrino telescope.* PhD thesis, Erlangen Centre for Astroparticle Physics (ECAP), Universität Erlangen, 2010. (Cited on pages 53 and 54.)

[86] Friederike Schöck. PhD thesis, Erlangen Centre for Astroparticle Physics (ECAP), Universität Erlangen, 2010. In preparation. (Cited on page 53.)

[87] Jürgen Brunner. The BBfit Reconstruction algorithm. *ANTARES internal note*, 2009. (Cited on page 54.)

[88] Ronald Bruijn. *The Antares Neutrino Telescope: Performance Studies and Analysis of First Data.* PhD thesis, Universiteit van Amsterdam, 2008. (Cited on page 54.)

[89] D Heck, J Knapp, J. N Capdevielle, et al. CORSIKA: a Monte Carlo code to simulate extensive air showers. *CORSIKA: a Monte Carlo code to simulate extensive air showers.*, 1998. (Cited on pages 54 and 58.)

[90] Dmitry Chirkin and Wolfgang Rhode. Propagating leptons through matter with Muon Monte Carlo (MMC). *arXiv*, 2004. (Cited on pages 54 and 59.)

[91] Geant4 Collaboration, S Agostinelli, J Allison, et al. Geant4 — a simulation toolkit. *Nucl. Instr. Meth. A*, 506:250, 2003. (Cited on pages 54 and 59.)

[92] H. L Lai, J Huston, S Kuhlmann, et al. Global QCD analysis of parton structure of the nucleon: CTEQ5 parton distributions. *The European Physical Journal C*, 12, 2000. (Cited on page 56.)

[93] R Gandhi, Chris Quigg, Mary Hall Reno, et al. Ultrahigh-energy neutrino interactions, 1996. (Cited on pages 56 and 57.)

[94] Dmitry Chirkin. dCORSIKA update. (Cited on page 58.)

[95] DE Groom, NV Mokhov, and SI Striganov. Muon stopping power and range tables 10 MeV-100 TeV. *Atom Data Nucl Data*, 78(2):183–356, 2001. (Cited on page 60.)

[96] M Ambrosio, R Antolini, G Auriemma, et al. Vertical muon intensity measured with MACRO at the gran sasso laboratory. *Phys. Rev. D*, 52(7):3793–3802, 1995. (Cited on page 60.)

[97] C D Mobley. *Light and Water. Radiative Transfer in Natural Waters.* Academic, New York, 1994. (Cited on page 62.)

[98] Jürgen Brunner. Cherenkov light from HE electromagnetic and hadronic showers. *ANTARES internal note*, 2002. (Cited on page 63.)

[99] J Lundberg, P Miočinović, K Woschnagg, et al. Light tracking through ice and water — Scattering and absorption in heterogeneous media with PHOTONICS. *Nucl. Instr. Meth. A*, 581:619, 2007. (Cited on pages 63 and 66.)

[100] M Anghinolfi, H Costantini, K Fratini, et al. New measurement of the angular acceptance of the Antares Optical Module. *ANTARES internal note*, 2008. (Cited on page 80.)

[101] ANTARES Collaboration, P Amram, M Anghinolfi, et al. The ANTARES optical module. *Nucl. Instr. Meth. A*, 484:369, 2002. (Cited on page 80.)

[102] S-O Flyckt and Carole Marmonier. *Photomultiplier tubes, principles and applications.* Photonis, Brive, France, 2002. (Cited on page 84.)

[103] J Ahrens, X Bai, R Bay, et al. Muon track reconstruction and data selection techniques in AMANDA. *Nucl. Instr. Meth. A*, 524:169, 2004. (Cited on pages 86, 89, and 90.)

[104] D Zaborov. Simulation of ANTARES KM3 detector. *ANTARES internal note*, 2002. (Cited on page 86.)

[105] D Zaborov. Updated results of Monte-Carlo simulation of km3-scale water Cherenkov detectors. *ANTARES internal note*, 2004. (Cited on page 86.)

[106] Dirk Pandel. *Bestimmung von Wasser- und Detektorparametern und Rekonstruktion von Myonen bis 100 TeV mit dem Baikal-Neutrinoteleskop NT-72.* Diplomarbeit, Humboldt-Universität zu Berlin, 1996. (Cited on pages 88 and 89.)

[107] Till Neunhöffer. *Die Entwicklung eines neuen Verfahrens zur Suche nach kosmischen Neutrino-Punktquellen mit dem AMANDA-Neutrinoteleskop.* PhD thesis, Johannes-Gutenberg-Universität in Mainz, 2003. (Cited on pages 89 and 95.)

[108] N van Eijndhoven, O Fadiran, and G Japaridze. Implementation of a Gauss convoluted Pandel PDF for track reconstruction in neutrino telescopes. *Astropart. Phys.*, 28:456, 2007. (Cited on page 90.)

[109] J A Nelder and R Mead. A Simplex Method for Function Minimization. *The Computer Journal*, 7(4):308–313, 1965. (Cited on page 93.)

[110] N Hansen and S Kern. Evaluating the CMA evolution strategy on multimodal test functions, 2004. (Cited on page 94.)

[111] Holger Motz. PhD thesis, Erlangen Centre for Astroparticle Physics (ECAP), Universität Erlangen, 2010. In preparation. (Cited on page 94.)

[112] Till Neunhöffer. Estimating the angular resolution of tracks in neutrino telescopes based on a likelihood analysis. *Astropart. Phys.*, 25:220, 2006. (Cited on page 95.)

[113] G.C Hill, J Hodges, B Hughey, et al. Examining the balance between optimising an analysis for best limit setting and best discovery potential. *Proc. of PHYSTAT 2005*, 2005. (Cited on page 99.)

[114] GJ Feldman and RD Cousins. Unified approach to the classical statistical analysis of small signals. *Phys. Rev. D*, 57(7):3873–3889, 1998. (Cited on pages 99 and 100.)

[115] GC Hill and K Rawlins. Unbiased cut selection for optimal upper limits in neutrino detectors: the model rejection potential technique. *Astropart. Phys.*, 19(3):393–402, 2003. (Cited on page 100.)

[116] Alexander Kappes. private communication. (Cited on page 139.)

Acknowledgements

All the work done for this thesis would certainly not have been possible without the help and contributions from lots of different people. I cannot name all of them and hope that no one feels left out.

Let me first thank my supervisor Uli Katz for the opportunity to work on such an interesting topic and for giving me a free hand with my research. Thank you, Uli, for always having an open door and for even having time for questions and advice when you did not have time at all! I am also extremely thankful for the invaluable discussions with Alexander Kappes. Without his feedback I would not have been able to finish this thesis in its current form. I had a lot of help with the technical work from fellow PhD student and systems administrator colleague Ralf Auer, who is currently on "leave" at the South Pole deploying lots of IceCube strings. I am a little jealous..

I would like to thank the entire ANTARES&KM3NeT group at the *Erlangen Centre for Astroparticle Physics* (ECAP) for the good atmosphere and the incredible working environment. Of all the other groups at ECAP, I have to especially thank the whole novel detector group. Thank you for accepting me into your "Kaffeezimmer" when our group did not have one yet. Without the daily coffee breaks I would have gone mad (and probably would have slept through most of my work day). I also would have missed the opportunity to get to know a lot of people and to make a lot of friends. As much as I would like to, I cannot mention everyone individually, but there are a few whom I would especially like to thank: Annelen, Björn, Ulle, Mike, Markus, Florian and Kati.

A large part of my work has been made so much easier because of contributions from the IceCube collaboration. I don't know if I could have achieved any of this without their software framework *IceTray*, which they let us use and which, in the meantime, has even become the official framework of ANTARES and KM3NeT. Thank you, Troy and Erik, for even encouraging us to use it!

Furthermore, I would like to thank all the colleagues of the ANTARES and KM3NeT collaborations I have met during my work. Let's keep ANTARES running as successful as possible and get the big one built! Thanks to Kati Kania, Alexander Kappes, Thomas Eberl and my brother Sandro for proofreading the manuscript.

And, finally, I owe a lot to my family for encouraging and supporting me the entire time. None of this would have been possible without them and I do not know how to thank them enough.